WISDOM Project - XII. Clump properties and turbulence regulated by clump-clump collisions in the dwarf galaxy NGC 404

Lijie Liu, Martin Bureau, Guang-Xing Li, Timothy A. Davis, Dieu D. Nguyen, Fu-Heng Liang, Woorak Choi, Mark R. Smith, Satoru Iguchi

Monthly Notices of the ROYAL ASTRONOMICAL SOCIETY

MNRAS **517,** 632–656 (2022) https://doi.org/10.1093/mnras/stac2287
Advance Access publication 2022 October 4

WISDOM Project – XII. Clump properties and turbulence regulated by clump–clump collisions in the dwarf galaxy NGC 404

Lijie Liu [1,2,3]★ Martin Bureau,[1,4] Guang-Xing Li [5], Timothy A. Davis [6], Dieu D. Nguyen [7], Fu-Heng Liang [1], Woorak Choi,[4] Mark R. Smith [1] and Satoru Iguchi [8,9]

[1]*Sub-department of Astrophysics, Department of Physics, University of Oxford, Keble Road, Oxford OX1 3RH, UK*
[2]*Cosmic Dawn Center (DAWN), Denmark*
[3]*DTU-Space, Technical University of Denmark, Elektrovej 327, DK-2800 Kgs. Lyngby, Denmark*
[4]*Yonsei Frontier Lab and Department of Astronomy, Yonsei University, 50 Yonsei-ro, Seodaemun-gu, Seoul 03722, Republic of Korea*
[5]*South-Western Institute for Astronomy Research, Yunnan University, Chenggong District, Kunming 650091, P. R. China*
[6]*School of Physics and Astronomy, Cardiff University, Queens Buildings, The Parade, Cardiff CF24 3AA, UK*
[7]*Ens de Lyon, CNRS, Centre de Recherche Astrophysique de Lyon (CRAL) UMR5574, Université de Lyon 1, F-69230 Saint-Genis-Laval, France*
[8]*Department of Astronomical Science, SOKENDAI (The Graduate University of Advanced Studies), Mitaka, Tokyo 181-8588, Japan*
[9]*National Astronomical Observatory of Japan, National Institutes of Natural Sciences, Mitaka, Tokyo 181-8588, Japan*

Accepted 2022 August 10. Received 2022 August 9; in original form 2021 November 29

ABSTRACT

We present a study of molecular structures (clumps and clouds) in the dwarf galaxy NGC 404 using high-resolution ($\approx$0.86 $\times$ 0.51 pc^2) Atacama Large Millimeter/sub-millimeter Array ^{12}CO(2-1) observations. We find two distinct regions in NGC 404: a gravitationally stable central region (Toomre parameter $Q = 3$–30) and a gravitationally unstable molecular ring ($Q \lesssim 1$). The molecular structures in the central region have a steeper size–linewidth relation and larger virial parameters than those in the molecular ring, suggesting gas is more turbulent in the former. In the molecular ring, clumps exhibit a shallower mass–size relation and larger virial parameters than clouds, implying density structures and dynamics are regulated by different physical mechanisms at different spatial scales. We construct an analytical model of clump–clump collisions to explain the results in the molecular ring. We propose that clump–clump collisions are driven by gravitational instabilities coupled with galactic shear, which lead to a population of clumps whose accumulation lengths (i.e. average separations) are approximately equal to their tidal radii. Our model-predicted clump masses and sizes (and mass–size relation) and turbulence energy injection rates (and size–linewidth relation) match the observations in the molecular ring very well, suggesting clump–clump collisions are the main mechanism regulating clump properties and gas turbulence in that region. As expected, our collision model does not apply to the central region, where turbulence is likely driven by clump migration.

Key words: galaxies: dwarf – galaxies: individual: NGC 404 – galaxies: ISM – galaxies: nuclei – radio lines: ISM.

1 INTRODUCTION

Dwarf galaxies are low-mass systems that are often different from present-day large spiral galaxies like the Milky Way (MW). They have overabundant atomic gas, low metallicities, long gas consumption times, and high gas mass fractions (e.g. Fukui & Kawamura 2010; Schruba et al. 2017). Molecular structures (clumps and clouds) in dwarf galaxies may also be quite different from those in the MW and Local Group galaxies, as they are shaped by different galactic environments (e.g. Hughes et al. 2013, 2016; Colombo et al. 2014; Sun et al. 2018, 2020). So far, detailed observations and analyses of molecular structures in dwarf galaxies have been limited to a handful of nearby systems (e.g. IC 10, Leroy et al. 2006; SMC, Muller et al. 2010; NGC 6822, Schruba et al. 2017; Henize 2-10, Imara & Faesi 2019; J1023+1952, Querejeta et al. 2021), as molecular tracers like CO and cold dust are often too faint to detect at low metallicities (e.g. Leroy et al. 2011; Elmegreen et al. 2013; Cormier et al. 2017; Hunter, Elmegreen & Berger 2019; Madden & Cormier 2019).

Dwarf galaxies may also serve as good analogues of the Universe's earliest galaxies (e.g. Motiño Flores, Wiklind & Eufrasio 2021a, b). It is well known that high-redshift star-forming galaxies are significantly different from local spiral galaxies, the former being gravitationally unstable (Toomre parameter $Q \leq 1$), distinctly clumpy, gas-rich, and dynamically hot (e.g. Tacconi 2012; Forbes et al. 2014; Genzel et al. 2014; Swinbank et al. 2015; Stott et al. 2016; Tadaki et al. 2018; Rizzo 2020; Tacconi, Genzel & Sternberg 2020). However, dwarf galaxies share many of these properties, e.g. young ages, low metallicities, high gas-mass fractions, and clumpy morphologies (e.g. Motiño Flores et al. 2021a, b). Hence, studying dwarf galaxies may provide unique insights into the evolution of the first galaxies.

Turbulence is a key factor regulating interstellar gas (e.g. Elmegreen & Scalo 2004) and star formation (e.g. Mac Low & Klessen 2004; Bournaud et al. 2010), but there is an ongoing debate over the source of the observed turbulence in dwarf galaxies. A

★ E-mail: ljliu.astro@gmail.com

commonly discussed source is stellar feedback, including supernovae and other stellar processes (e.g. winds and outflows). However, many dwarf galaxies have very low star formation rate (SFR) densities, and stellar feedback cannot plausibly provide enough energy in these systems (e.g. Stilp et al. 2013). The magneto-rotational and/or thermal instabilities do not appear to be sufficient either (e.g. Kim, Ostriker & Stone 2003; Piontek & Ostriker 2004, 2005, 2007; Agertz, Teyssier & Moore 2009). Possible drivers of turbulence in dwarf galaxies are thus large-scale gravitational instabilities (e.g. Elmegreen & Burkert 2010; Elmegreen 2011; Goldbaum, Krumholz & Forbes 2015; Krumholz & Burkhart 2016), which lead to a population of massive cold clumps undergoing mutual gravitational interactions and merging (i.e. collisions). Such clump–clump collisions can induce significant turbulent motions in the gas, by extracting energy from the rotational energy of the galaxies (e.g. Agertz et al. 2009; Tasker & Tan 2009; Bournaud et al. 2010; Williamson & Thacker 2012; Stilp et al. 2013; Goldbaum et al. 2015; Goldbaum, Krumholz & Forbes 2016; Li et al. 2018).

Clump–clump collisions can also create parsec-scale dense gas structures (e.g. Gammie 2001; Tasker & Tan 2009), regulate clump (or cloud) properties (e.g. Bournaud et al. 2010; Dobbs & Pringle 2013; Li et al. 2018), and trigger star formation events (Hasegawa et al. 1994; Fukui et al. 2021; Maeda et al. 2021; Sano et al. 2021), particularly high-mass star and star-cluster formation (e.g. Tan 2000; Myers 2009; Schneider et al. 2012; Dobbs et al. 2014; Kobayashi et al. 2018; Wu et al. 2018; Henshaw et al. 2019). Collisions between clumps have been clearly observed and identified in many galaxies, including high-speed ($\approx$20 km s^{-1}) collisions between clouds in the barred galaxy NGC 1300 (Maeda et al. 2021) and extreme collisions (>100 km s^{-1}) between clouds in the centre of the MW (Sormani et al. 2019; Henshaw et al. 2022) and the overlap region of the Antennae galaxies (Fukui et al. 2021). However, not many analytical models have been developed to quantify the effects of these collisions. Dedicated numerical simulations have been performed (e.g. Tasker & Tan 2009; Wu et al. 2017a, b, 2018; Li et al. 2018), but they are mainly focused on MW-type gas discs.

In this paper, we perform statistical analyses of the multiple-scale molecular structures of the dwarf lenticular galaxy NGC 404, exploiting high-spatial resolution ($\approx$0.86 $\times$ 0.51 pc^2) Atacama Large Millimeter/sub-millimeter Array (ALMA) ^{12}CO(2-1) observations. The results are confronted with a new simple analytical model of clump–clump collisions, and a good explanation of the observational results in the molecular ring of NGC 404 is achieved. We describe our target and ALMA data in Section 2. Basic observational results are presented in Section 3. Our analytic model of clump–clump collisions and its comparison to observations are described in Section 4. In Section 5, we describe the implications of the clump–clump collision-induced turbulence. We provide a discussion in Section 6 and our conclusions in Section 7.

2 DATA AND STRUCTURAL DECOMPOSITION

2.1 Target

NGC 404 is the nearest face-on S0 galaxy (distance D = 3.06 $\pm$ 0.37 Mpc; Karachentsev et al. 2002). It has a large stellar disc (isophotal diameter >20 kpc at a V-band surface brightness μ_V = 31.5 mag arcsec^{-2}; Tikhonov, Galazutdinova & Aparicio 2003; Seth et al. 2010; Nguyen 2017) which is known to be dominated by old stellar populations (ages >10 Gyr; Williams et al. 2010). The centre of NGC 404, however, appears to be dominated by young stellar populations (ages $\leq$1 Gyr; Maoz et al. 1998; Boehle et al. 2018). NGC 404 harbours a low-ionization nuclear emission region (LINER; Schmidt, Bica & Alloin 1990). The dynamical centre of the galaxy is revealed by a central radio continuum peak which is spatially coincident with a hard X-ray source (Taylor, Petitpas & del Rio 2015). The galaxy exhibits bright extended Hα emission (Nyland et al. 2017) and widespread shocks in the nucleus (Boehle et al. 2018). NGC 404 also appears to host an accreting massive black hole, with a mass $M_{\rm BH} \approx 5.7 \times 10^5$ M$_\odot$ constrained from both stellar and molecular gas kinematics (Davis et al. 2020).

NGC 404 contains an appreciable amount of atomic ($\approx 1.5 \times 10^8$ M$_\odot$; del Río, Brinks & Cepa 2004) and molecular ($\approx 9.0 \times 10^6$ M$_\odot$; Taylor et al. 2015) gas. Approximately 75 per cent of the H I is located in a nearly face-on doughnut-shaped distribution, with a central hole that nicely matches the optical galaxy (del Río et al. 2004). The molecular gas, however, is located on a much smaller spatial scale ($\approx$140 $\times$ 130 pc^2) at the centre of the optical galaxy and the H I hole, as revealed by low-resolution (7.0 arcsec $\times$ 7.6 arcsec synthesized beam) Berkeley–Illinois–Maryland Association (BIMA) radio telescope array ^{12}CO(1-0) observations (Taylor et al. 2015). The peak of CO(1-0) emission is spatially coincident with the dynamical centre of the galaxy identified by the radio continuum and hard X-ray sources. The total CO(1-0) flux detected by BIMA is 67.4 Jy km s^{-1} (Taylor et al. 2015). There is tentative evidence that NGC 404 acquired gas 0.5–1.0 Gyr ago through a merger with a gas-rich dwarf irregular system (del Río et al. 2004; Taylor et al. 2015; Nguyen 2017).

2.2 ALMA data

NGC 404 was observed in the ^{12}CO(2-1) line ($\approx$230 GHz) using ALMA for a total of five tracks, three in extended configurations and two with shorter baselines. This yielded a total baseline range of 15–16 200 m, a field of view [full width at half-maximum (FWHM) of the primary beam] of FWHM $\approx$ 24.5 arcsec which extends far beyond the molecular gas disc, and a maximum recoverable scale of $\approx$10.4 arcsec which is much larger than the largest single molecular structure identified in this work. See Davis et al. (2020) for more details of the observations. The raw ALMA data were calibrated using the standard ALMA pipeline and imaged using Briggs weighting with a robust parameter of 0.5, yielding a synthesized beam of FWHM $\approx$ 0.058 arcsec $\times$ 0.034 arcsec ($\approx$0.86 $\times$ 0.51 pc^2) at a position angle of 36°. Continuum emission was detected and subtracted in the uv plane. The data cube used in this paper is slightly different from that of Davis et al. (2020), with a channel width of 2 km s^{-1}, a root-mean-squared (RMS) noise $\sigma_{\rm rms}$ = 1.13 mJy beam^{-1} per channel (13.1 K converted to brightness temperature), and spaxels of 0.02 arcsec $\times$ 0.02 arcsec (thus yielding $\approx$5.6 spaxels per synthesized beam).

Fig. 1 shows the zeroth-moment (integrated-intensity) map of our adopted data cube, created using a smooth-masking moment technique (e.g. Dame 2011). To generate the mask, the data cube was convolved spatially by a Gaussian of width equal to that of the synthesized beam, Hanning-smoothed in velocity and clipped at a fixed threshold (0.3$\sigma_{\rm rms}$). The integrated CO(2-1) intensity is 210 Jy km s^{-1}. Comparing our CO(2-1) integrated intensity to that in CO(1-0) by Taylor et al. (2015), we obtain a CO(2-1)/CO(1-0) line ratio of $\approx$0.78 in temperature units, similar to the average MW ratio of 0.8 (Carilli & Walter 2013). We thus estimate a total molecular gas mass of $\approx 9.4 \times 10^6$ M$_\odot$, derived using our integrated ALMA CO(2-1) intensity and the CO(2-1)/CO(1-0) line ratio of 0.78, and assuming a standard Galactic CO-to-H$_2$ conversion factor $X_{\rm CO}$ = 2 $\times$ 10^{20} cm^{-2} (K km s^{-1})$^{-1}$ (as despite a low total stellar mass,

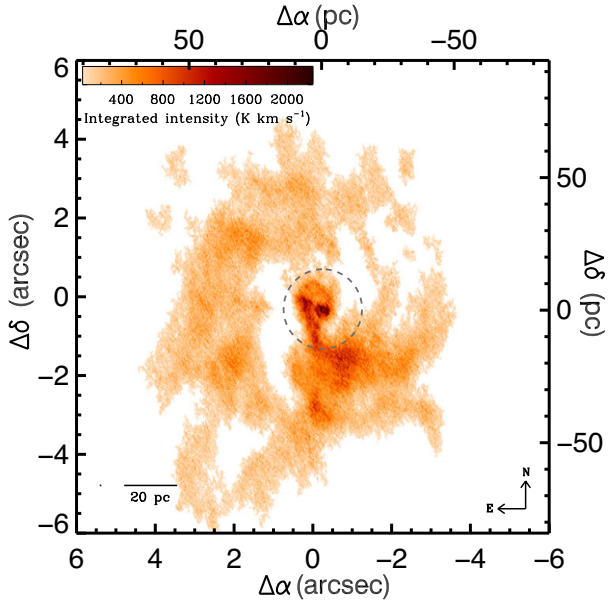

Figure 1. Moment-zero map of the ^{12}CO(2-1) emission of NGC 404 derived from our ALMA observations. The synthesized beam (≈0.058 arcsec × 0.034 arcsec or ≈0.86 × 0.51 pc^2) is shown as a very small black ellipse to the left of the scale bar in the bottom-left corner. The grey dashed ellipse at a galactocentric distance of 15 pc separates the central region and molecular ring discussed in the text.

NGC 404 has approximately solar ionized gas metallicity; Bresolin 2013; Davis et al. 2020).

The ALMA CO(2-1) observations reveal a complex molecular gas morphology (see Fig. 1; Davis et al. 2020), including a central disc/ring within a radius of ≈8 pc (centre RA (J2000) = 01^{h}09^{m}27^s.001 and Dec. (J2000) = +35°43′04″.942, inclination i = 37.1°, position angle PA = 37.2°), a single arm-like feature with a radius of ≈8–15 pc, and an incomplete (pseudo-)ring with a radius of ≈15–50 pc (i = 9.3°, PA ≈ 1°). Hereafter, we will refer to the central disc/ring and arm-like feature as the central region (galactocentric distances $R_{gal} \leq 15$ pc), and to the outer incomplete (pseudo-)ring as the molecular ring ($15 < R_{gal} \lesssim 50$ pc). The grey dashed ellipse in Fig. 1 separates the two regions. The central region's kinematic centre is spatially coincident with the continuum source detected with very long baseline interferometry (VLBI; Nyland et al. 2017), while the molecular ring contains multiple spatially resolved molecular structures corresponding to dust features seen in absorption in *Hubble Space Telescope* (*HST*) images (see e.g. fig. 3 in Davis et al. 2020).

2.3 Structural decomposition

We use the dendrogram (i.e. tree analysis) code ASTRODENDRO described by Rosolowsky et al. (2008) to identify molecular structures in NGC 404. A three-dimensional mask of bright emission is initially created using the code CPROPSTOO (Rosolowsky & Leroy 2006; Leroy et al. 2015). All single pixels with brightness temperatures $T_b > 3\sigma_{rms}$ (≈39 K) are first identified, and the pixel list is then expanded to include all neighbouring pixels with $T_b > 1.5\sigma_{rms}$ (≈20 K). Each discrete region of signal in the mask (i.e. each 'island') is also required to have a minimum projected diameter of ≈3 pc (≈100 spaxels in area), corresponding to the maximum Jeans length in the outer parts of the molecular ring (see Section 4.5). Fig. 2 shows the zeroth-moment map of NGC 404 created using this mask. The integrated CO(2-1) intensity within the masked region is ≈151 Jy km s^{-1}, ≈ 72 per cent of the total integrated ALMA CO(2-1) intensity.

A hierarchy of molecular structures is then identified using the code ASTRODENDRO. The algorithm first sets a minimum significant isophotal contour for every region; emission fainter than $min\_value = 1.5\sigma_{rms}$ (≈20 K) is not characterized. This step has almost no effect, however, as the CPROPSTOO-generated mask with a threshold of $1.5\sigma_{rms}$ has already been applied to the data cube. The algorithm then identifies local maxima of brightness temperatures at least $min\_delta = 1.5\sigma_{rms}$ (≈20 K) above the merger level with any other local maximum (i.e. above the highest contour/isophotal level enclosing a pair of local maxima). The minimum area (min_area) and minimum number of pixels (min_npix) that each local maximum should span are also specified. Here, we require $min\_area = min\_npix = 6$, so that each local maximum spans at least one synthesized beam.

The isosurfaces surrounding local maxima are then categorized into different types of structures: leaves, branches, and trunks. Leaves are the smallest structures and do not contain any substructure (i.e. they contain only one local maximum), trunks are the largest contiguous structures (i.e. they have no parent structure), and branches are intermediate in scale (and can have both substructures, i.e. branches and leaves, and parent structures, i.e. branches and trunks). Trunks therefore do not overlap any other trunks, and leaves do not overlap any other leaves (Wong et al. 2019), but both trunks and branches can split up into branches and/or leaves, thus allowing hierarchical structures to be adequately identified and represented (Rosolowsky et al. 2008). The algorithm identifies 3626 molecular structures in NGC 404: 50 trunks, 1642 branches, and 1934 leaves. The trunks in our catalogue recover almost all of the CPROPSTOO-masked CO(2-1) emission, while the leaves contain a total of ≈83 Jy km s^{-1} or ≈ 55 per cent of this emission.

Once a hierarchy of structures has been identified by ASTRODENDRO, we use our modified version of CPROPSTOO (see Liu et al. 2021) to calculate the properties of the structures identified. The code CPROPSTOO is chosen because it attempts to correct the measured quantities for the finite sensitivity of the observations, extrapolating sizes, linewidths, and luminosities to their infinite signal-to-noise ratio (S/N) equivalents (i.e. to a brightness temperature at the edge of the structures identified $T_{edge} = 0$ K). CPROPSTOO also 'deconvolves' in two dimensions the measured (and extrapolated) sizes, to account for the finite size of the synthesized beam, thus roughly correcting for possible resolution biases.

Table 1 lists the position and properties of each identified structure: structure size (radius) R_c, one-dimensional observed linewidth (velocity dispersion) $\sigma_{obs,\,los}$, CO(2-1) luminosity $L_{CO(2-1)}$, gaseous mass M_c [assuming a CO(2-1)/CO(1-0) line ratio of 0.78, and a standard Galactic CO-to-H$_2$ conversion factor $X_{CO} = 2 \times 10^{20}$ cm^{-2} (K km s^{-1})$^{-1}$; referred to as M_{gas} in Liu et al. 2021], and deprojected galactocentric distance R_{gal}. The uncertainties of the measured properties are estimated via a bootstrapping technique. For a detailed definition of each property and its uncertainty, refer to Liu et al. (2021). About 50 per cent (953/1934) of the identified leaves, ≈ 97 per cent (1592/1642) of the identified branches, and ≈ 94 per cent (47/50) of the identified trunks are resolved, i.e. have deconvolved diameters larger than or equal to the synthesized beam in two dimensions and deconvolved velocity widths at least half of one velocity channel (Donovan Meyer et al. 2013). Fig. 2 shows the resolved leaves (blue ellipses) and trunks (coloured contours) of NGC 404 overlaid on the zeroth-moment map created with the CPROPSTOO-generated mask.

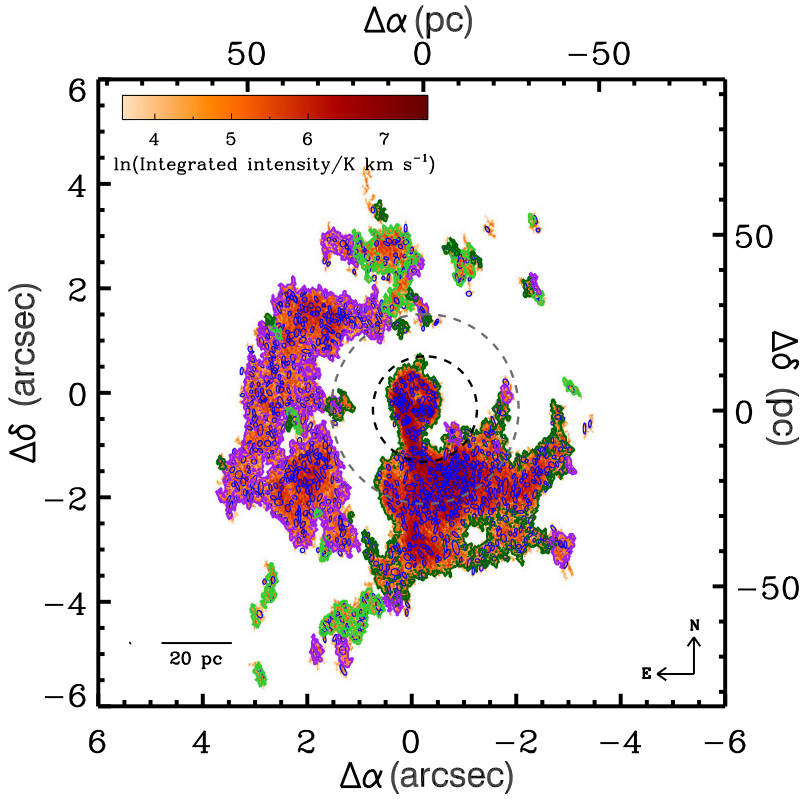

Figure 2. CO(2-1) integrated-intensity map of NGC 404 (colour scale), blanking out faint areas using the CPROPSTOO-generated mask. The mask covers pixels with connected emission above $1.5\sigma_{\rm rms}$ and at least one channel above $3\sigma_{\rm rms}$, where $\sigma_{\rm rms}$ is the RMS noise of the data cube. The coloured contours show resolved trunks, while the blue ellipses show resolved leaves (i.e. clumps; extrapolated to the limit of perfect sensitivity but not corrected for the finite angular resolution). The black dashed ellipse at a galactocentric distance of 15 pc separates the central region and molecular ring discussed in the text, while the grey dashed ellipse at a galactocentric distance of 27 pc indicates the galactocentric distance beyond which the molecular gas disc is no longer gravitationally stable (i.e. the Toomre parameter $Q \leq 1$ at $R_{\rm gal} \geq 27$ pc; see Section 4.5 for more details). The synthesized beam (≈0.058 arcsec × 0.034 arcsec or ≈0.86 × 0.51 pc^2) is shown as a very small black ellipse to the left of the scale bar in the bottom-left corner.

Table 1. Properties of the dendrogram-defined structures of NGC 404.

ID	RA (2000) (h:m:s)	Dec. (2000) (°: ′: ″)	$V_{\rm LSR}$ (km s^{-1})	$R_{\rm c}$ (pc)	$\sigma_{\rm obs,\,los}$ (km s^{-1})	$L_{\rm CO(2\text{-}1)}$ (10^4 K km s^{-1} pc^2)	$M_{\rm c}$ (10^5 M$_\odot$)	$R_{\rm gal}$ (pc)	Structure
1	01:09:27.00	35:43:04.85	−111.1	–	2.0 ± 0.9	0.03 ± 0.01	0.02 ± 0.01	1.5	L
2	01:09:26.98	35:43:03.64	−58.0	24.8 ± 3.3	10.0 ± 1.2	127.5 ± 1.9	70.1 ± 1.1	19.9	B
3	01:09:26.97	35:43:03.60	−57.8	26.7 ± 6.4	10.4 ± 1.8	139.4 ± 1.9	76.7 ± 1.0	20.8	B
–	–	–	–	–	–	–	–	–	–
3626	01:09:27.01	35:43:04.97	7.2	–	1.9 ± 1.0	0.03 ± 0.02	0.01 ± 0.01	0.9	L

Notes. Measurements of $R_{\rm c}$ assume $\eta = 1.91$. Measurements of $M_{\rm c}$ assume a CO(2-1)/CO(1-0) line ratio of 0.78 in temperature units and a standard Galactic conversion factor $X_{\rm CO} = 2 \times 10^{20}$ cm^{-2} (K km s^{-1})$^{-1}$ (including the mass contribution from helium). Structure codes: L – leaf, B – branch, T – trunk. Measurements of $R_{\rm gal}$ adopt a fixed position angle PA = 1° and inclination angle $i = 9.3°$. The uncertainty of the adopted distance D to NGC 404 was not propagated through the tabulated uncertainties of the measured quantities. This is because an error on the distance to NGC 404 translates to a systematic (rather than random) scaling of some of the measured quantities (no effect on the others), i.e. $R_{\rm c} \propto D$, $L_{\rm CO(2\text{-}1)} \propto D^2$, $M_{\rm c} \propto D^2$, and $R_{\rm gal} \propto D$. Table 1 is available in its entirety in machine-readable form in the electronic edition.

In this paper, we will refer to single centrally concentrated structures as 'clumps', and those objects with more complex structures as 'clouds'. We therefore treat dendrogram-defined leaves as clumps, and both branches and trunks as clouds, because by definition leaves cannot contain any substructure, while both branches and trunks must harbour multiple substructures. Here, 'substructure' is understood to be emission within a contour (in a 3D data cube) of $min\_delta = 1.5\sigma_{\rm rms}$ that has a minimum area of one synthesized beam. Hereafter, the subscript 'c' will denote both clumps and clouds, while the subscripts 'clump' and 'cloud' will refer to only clumps and only clouds, respectively.

3 RESULTS

3.1 Mass function of clumps

In this section, we analyse the mass distribution functions of independent structures, i.e. clumps, in NGC 404. The distribution of clumps by mass provides important information not only on the mechanisms

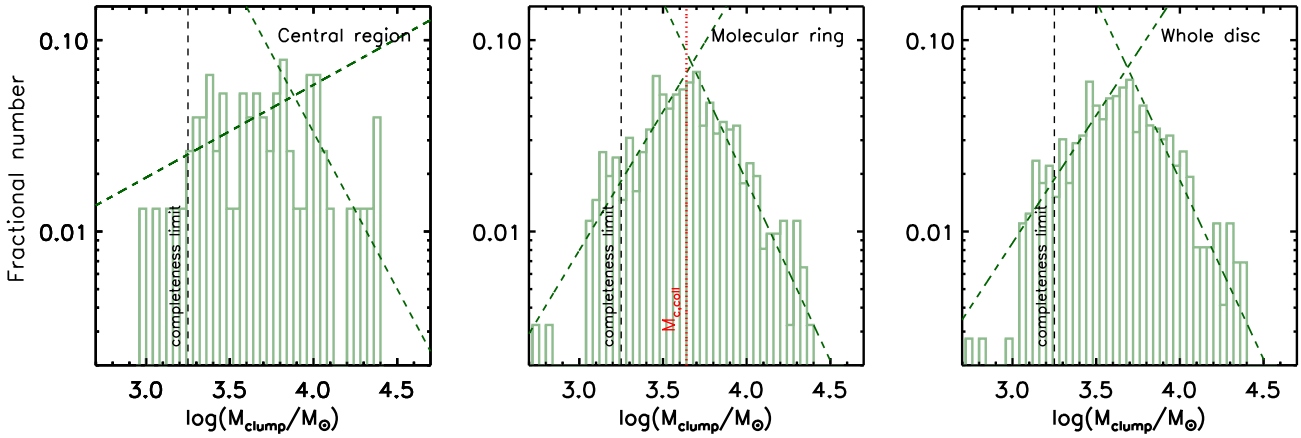

Figure 3. Normalized differential mass distribution function of the resolved clumps in the central region, molecular ring, and whole disc of NGC 404, respectively. The two power laws best fitting the differential mass distribution are overlaid as green dashed lines in each panel. Our mass completeness limit is indicated by a black vertical dashed line in each panel. The red dotted line in the middle panel indicates our model-predicted turn-over mass in the molecular ring ($M_{\rm c,\,coll}$; see Sections 4.2 and 6.1 for more details).

that influence clump formation, evolution, and destruction (e.g. Rosolowsky 2005; Colombo et al. 2014; Faesi, Lada & Forbrich 2016), but also on the factors regulating star formation. Indeed, the SFR diversity across galactic discs could simply originate from diverse clump populations (Kobayashi et al. 2017, 2018).

The differential clump mass distribution function can be characterized by a power law

$$\mathrm{d}N_{\rm clump}(M_{\rm clump})/\mathrm{d}M_{\rm clump} \propto M_{\rm clump}^{\gamma_{\rm clump}} \quad (1)$$

(or equivalently $dN_{\rm clump}(M_{\rm clump})/d\log M_{\rm clump} \propto M_{\rm clump}^{\gamma_{\rm clump}+1}$), where $N_{\rm clump}(M_{\rm clump})$ is the number of clumps with masses greater than $M_{\rm clump}$ and $\gamma_{\rm clump}$ is the power-law index, usually compared to an index of -2. If $\gamma_{\rm clump} < -2$, most of the molecular mass is found in low-mass clumps, while if $\gamma_{\rm clump} > -2$, most of the galaxy's molecular mass is located in high-mass clumps.

Fig. 3 shows the normalized differential mass distribution functions of the resolved clumps in the central region, molecular ring, and whole disc of NGC 404. The black vertical dashed line in each panel indicates the mass completeness limit $M_{\rm comp} = 1.8 \times 10^3$ M$_\odot$, estimated from the minimum resolved clump (gaseous) mass ($M_{\rm min} \approx$ 600 M$_\odot$) and the observational sensitivity $\delta_{\rm M} = 120$ M$_\odot$, i.e. $M_{\rm comp} \equiv M_{\rm min} + 10\delta_{\rm M}$. Here, the contribution to the mass due to noise $\delta_{\rm M}$ is estimated by multiplying our RMS column density sensitivity limit of $\approx$250 M$_\odot$ pc^{-2} (derived from our RMS noise $\sigma_{\rm rms}$) by the synthesized beam area of $\approx$0.49 pc^2.

We find 'turn-overs', that is, break points in the single power-law functions, in all the normalized differential mass distributions, always at the same clump mass $M_{\rm clump} \approx 4000$ M$_\odot$. As this turn-over mass is much larger than our estimated mass completeness limit, it is most likely real and thus informs on the underlying formation and destruction of clumps. We therefore fit the normalized differential mass distributions with two separate power laws, one for the high-mass regime $M_{\rm clump} \gtrsim 4000$ M$_\odot$, with a power-law index of $\gamma^{+}_{\rm clump}$, and the other for the low-mass regime $M_{\rm comp} \lesssim M_{\rm clump} \lesssim 4000$ M$_\odot$, with a power-law index of $\gamma^{-}_{\rm clump}$. All normalized differential mass distribution functions can be well described by such broken power laws, and the best-fitting power-law indices of each region are listed in Table 2. We note that the power-law index of the differential clump mass distribution function in the high-mass regime $\gamma^{+}_{\rm clump}$ is consistent with the best-fitting power-law indices of the cumulative clump mass distribution function (see Appendix A for the normalized cumulative mass distribution functions of the resolved clumps in the different regions of NGC 404).

The mass distribution functions of the NGC 404 clumps are unusually steep in the high-mass regime ($\gamma^{+}_{\rm clump} \approx -2.8$–$-2.6$), much steeper (i.e. more negative) than those of MW clumps and clouds ($\gamma_{\rm c} \approx -1.7$–$-1.5$; Simon et al. 2001; McKee & Ostriker 2007; Rice et al. 2016) and Local Group galaxy clouds ($\gamma_{\rm cloud} = -2.0$–$-1.7$; Fukui et al. 2001; Leroy et al. 2006; Wong et al. 2011; Faesi et al. 2016; except for M 33 clouds with $\gamma_{\rm cloud} \approx -2.5$; Blitz & Rosolowsky 2006). They are also slightly steeper than those of the clouds in the early-type galaxies (ETGs) NGC 4526 and NGC 4429 ($\gamma_{\rm cloud} \approx -2.3$–$-2.1$; Utomo et al. 2015; Liu et al. 2021). Interestingly, the steep power-law indices $\gamma^{+}_{\rm clump}$ of the NGC 404 clumps are similar to that of the massive end of the observed stellar initial mass function ($\gamma \approx -2.4$; Salpeter 1955; Chabrier 2003).

The best-fitting power-law indices in the low-mass regime are much larger ($\gamma^{-}_{\rm clump} \approx -0.5$–$0.4$). The number of clumps in NGC 404 thus seems to increase with increasing mass when $M_{\rm clump}$ is smaller than the turn-over mass ($\approx$4000 M$_\odot$), and to decrease sharply thereafter.

Overall, the clump mass distribution functions of NGC 404 seem to favour the formation of clumps with a mass around that of the turn-over mass ($\approx$4000 M$_\odot$), and we shall discuss the implications of this observed turn-over mass in Section 6.1.

3.2 Multiple-scale size–linewidth relations

The empirical relation between size and linewidth has become the yardstick against which to compare studies of clumps and clouds in the MW and other galaxies (e.g. Bolatto et al. 2008). It is of fundamental importance because it can be interpreted as a signature of turbulent motions within molecular structures (e.g. Rosolowsky 2005). As a dendrogram approach allows us to identify a full hierarchy of molecular structures, we are able to investigate whether the size–linewidth relation (and thus turbulence) is universal from the large-scale interstellar medium (ISM) to its smallest and densest structures (e.g. Shetty & Ostriker 2012).

Fig. 4 presents the size–linewidth relations of the molecular structures in the central region, molecular ring, and whole disc of NGC 404. Clumps, i.e. leaves, are shown as filled green circles.

Table 2. Summary of the observational results of NGC 404.

	Central region	Molecular ring	Whole disc
Mass functions of clumps	$\gamma^{-}_{\rm clump} = -0.52 \pm 0.49$ $\gamma^{+}_{\rm clump} = -2.63 \pm 0.49$	$\gamma^{-}_{\rm clump} = 0.37 \pm 0.08$ $\gamma^{+}_{\rm clump} = -2.87 \pm 0.13$	$\gamma^{-}_{\rm clump} = 0.25 \pm 0.19$ $\gamma^{+}_{\rm clump} = -2.67 \pm 0.16$
Size–linewidth relation	$\sigma_{\rm obs,los} = (3.24 \pm 0.08)\, R_{\rm c}^{0.82\pm0.11}$	$\sigma_{\rm obs,los} = (2.95 \pm 0.13)\, R_{\rm c}^{0.30\pm0.03}$	$\sigma_{\rm obs,los} = (3.02 \pm 0.15)\, R_{\rm c}^{0.30\pm0.04}$
Mass–size relation	$D_{\rm m,c} = 2.27 \pm 0.10$ $D_{\rm m,\,clump} = 2.07 \pm 0.16$ $D_{\rm m,cloud} = 2.22 \pm 0.10$	$D_{\rm m,c} = 2.12 \pm 0.01$ $D_{\rm m,\,clump} = 1.63 \pm 0.04$ $D_{\rm m,cloud} = 2.06 \pm 0.01$	$D_{\rm m,c} = 2.11 \pm 0.01$ $D_{\rm m,\,clump} = 1.65 \pm 0.04$ $D_{\rm m,cloud} = 2.04 \pm 0.01$
Virial parameter	$\langle\alpha_{\rm vir,c}\rangle = 1.35 \pm 0.13$ $\langle\alpha_{\rm vir,\,clump}\rangle = 1.52 \pm 0.11$ $\langle\alpha_{\rm vir,cloud}\rangle = 1.14 \pm 0.12$	$\langle\alpha_{\rm vir,c}\rangle = 0.67 \pm 0.10$ $\langle\alpha_{\rm vir,\,clump}\rangle = 1.82 \pm 0.07$ $\langle\alpha_{\rm vir,cloud}\rangle = 0.41 \pm 0.02$	$\langle\alpha_{\rm vir,c}\rangle = 0.73 \pm 0.10$ $\langle\alpha_{\rm vir,\,clump}\rangle = 1.78 \pm 0.05$ $\langle\alpha_{\rm vir,cloud}\rangle = 0.41 \pm 0.02$
$M_{\rm c}$–$\alpha_{\rm vir,\,c}$ relation	–	$\alpha_{\rm vir,c} \propto M_{\rm c}^{-0.27\pm0.01}$	$\alpha_{\rm vir,c} \propto M_{\rm c}^{-0.27\pm0.01}$
	–	$\alpha_{\rm vir,clump} \propto M_{\rm clump}^{-0.33\pm0.04}$	$\alpha_{\rm vir,clump} \propto M_{\rm clump}^{-0.33\pm0.03}$
	–	$\alpha_{\rm vir,cloud} \propto M_{\rm cloud}^{-0.24\pm0.03}$	$\alpha_{\rm vir,cloud} \propto M_{\rm cloud}^{-0.25\pm0.01}$

Notes. The subscript 'c' denotes both clumps and clouds, while the subscripts 'clump' and 'cloud' refer to only clumps and only clouds, respectively. The power-law indices $\gamma^{+}_{\rm clump}$ and $\gamma^{-}_{\rm clump}$ are for the differential mass distribution functions of the clumps in the high-mass ($M_{\rm clump} \gtrsim 4000\ {\rm M}_\odot$) and low-mass ($M_{\rm comp} \lesssim M_{\rm clump} \lesssim 4000\ {\rm M}_\odot$) regime, respectively.

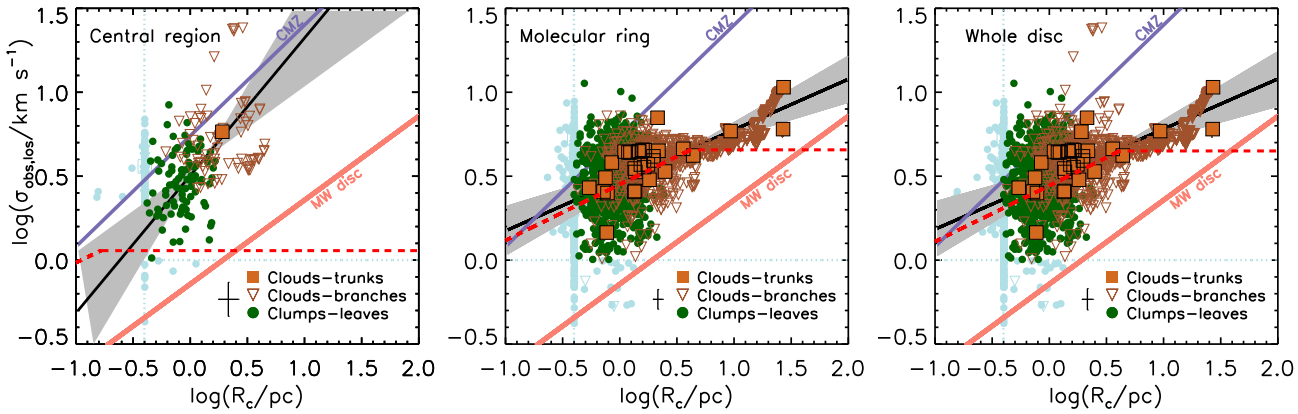

Figure 4. Size–linewidth relation of the molecular structures in the central region, molecular ring, and whole disc of NGC 404, respectively. Resolved clumps, i.e. leaves, are shown as filled green circled and resolved clouds, i.e. branches and trunks, are shown as open brown triangles and filled brown squares, respectively. The blue symbols denote unresolved structures. The horizontal and vertical blue dotted lines indicate our resolution limit of 1 km s^{-1} (i.e. half the channel width) and 0.40 pc (i.e. half the synthesized beam), respectively. In each panel, the black solid line with associated shading shows the best-fitting power-law relation of all resolved molecular structures with 1σ confidence intervals, while the red dashed line shows the $R_{\rm c}$–$\sigma_{\rm obs,\,los}$ relation predicted by our cloud–cloud collision model (see Section 4.4). The peach and purple solid lines show the size–linewidth relation of the MW disc (Solomon et al. 1987) and MW central molecular zone (Kauffmann et al. 2017), respectively. The typical uncertainty is shown as a black cross to the left of the legend in the bottom-right corner of each panel.

Clouds, i.e. branches and trunks, are shown as open brown triangles and filled brown squares, respectively. The molecular structures identified in NGC 404 span a relatively large dynamic range, with sizes spanning about two orders of magnitude and velocity dispersions spanning over one order of magnitude. We note that the observed velocity dispersions $\sigma_{\rm obs,\,los}$ shown in Fig. 4 should be almost exclusively comprised of turbulent motions. Following the method of Liu et al. (2021) (i.e. comparing $\sigma_{\rm obs,\,los}$ with the gradient-subtracted velocity dispersion measure $\sigma_{\rm gs,\,los}$), we found no evidence of a significant contribution of galactic rotation at the clump and cloud scales (i.e. $\sigma_{\rm obs,\,los} \approx \sigma_{\rm gs,\,los}$ for most clumps and clouds). Besides, as the galaxy is nearly face-on ($i \approx 9^\circ$ at $R_{\rm gal} \geq 15$ pc; Davis et al. 2020), contamination by (orbital) motions driven by the background galaxy potential in the disc plane ($\sigma_{\rm gal,\,r}$ radially and $\sigma_{\rm gal,\,t}$ azimuthally; see Liu et al. 2021) should be negligible for most molecular structures. The use of the gradient-subtracted velocity dispersion $\sigma_{\rm gs,\,los}$ is therefore unnecessary in this work.

The best-fitting size–linewidth relation of each region is listed in Table 2. The molecular structures in the central region exhibit an unusually steep size–linewidth relation with a slope of 0.82 ± 0.11, while those in the molecular ring have a much shallower relation with a slope of 0.30 ± 0.03. This trend is consistent with that in the MW, where the central molecular zone (CMZ) clouds have a size–linewidth relation steeper than that of clouds elsewhere in the disc (slope $\approx$0.7 compared to $\approx$0.5; e.g. Oka et al. 2001; Kauffmann et al. 2017). The molecular structures in the central region of NGC 404 also generally have velocity dispersions larger than those of similarly sized structures in the molecular ring. This is again similar to the behaviour observed in the MW, where at a given size the clumps/clouds in the CMZ have velocity dispersions larger than

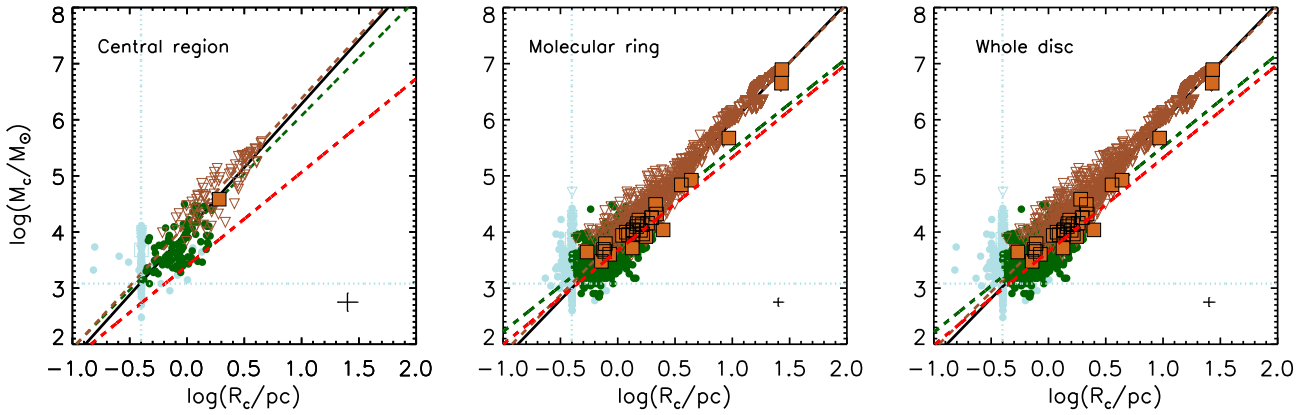

Figure 5. Mass–size relation of the molecular structures in the central region, molecular ring, and whole disc of NGC 404, respectively. Symbols are as for Fig. 4. The vertical blue dotted line indicates our spatial resolution limit of 0.40 pc (i.e. half the synthesized beam), while the horizontal blue dotted line indicates our mass detection limit ($\log(10\delta_{\rm M}/{\rm M}_\odot) = 3.08$; see Section 3.1). In each panel, the solid black, green, and brown lines show the best-fitting power-law relation of all resolved molecular structures, only resolved clumps (i.e. leaves), and only resolved clouds (i.e. branches and trunks), respectively, while the red dashed line shows the $M_{\rm c}$–$R_{\rm c}$ relation of clumps predicted by our cloud–cloud collision model (see equation 35 and Section 5.2).

those of clumps/clouds in the disc (e.g. Oka et al. 2001; Kauffmann et al. 2017).

It is worth noting that the power-law index found for the molecular ring (0.30 ± 0.03) is similar to that of the Kolmogorov (1941) law of incompressible turbulence, whereby $\sigma_{\rm obs,los} \propto R_{\rm c}^{1/3}$ based on a constant energy transmission rate in the turbulent cascade. However, the much steeper slope of 0.82 ± 0.11 is found in the central region, suggesting that the turbulence is highly compressible in this area, and the energy transmission through decreasing spatial scales is no longer conservative with kinetic energy also being expended to shock and/or compress the gas (e.g. Mac Low 1999; Federrath 2013; Cen 2021).

While a single power law seems to fit well the size–linewidth relation observed in the central region, the same relation appears to break down in the molecular ring at a scale of $R_{\rm c} \approx 3$ pc, where a flattening (i.e. a turn-over) is observed. The scatter around the $R_{\rm c}$–$\sigma_{\rm obs,\,los}$ is also much larger at scales below this turn-over scale (primarily clumps) than above (primarily clouds). The flattening and scatter of the $R_{\rm c}$–$\sigma_{\rm obs,\,los}$ relation suggest a turbulence driving scale of ≈3 pc in the molecular ring. Indeed, the velocity dispersion is expected to remain constant at scales larger than that driving the turbulence (e.g. Blitz & Rosolowsky 2006). The flattening at $R_{\rm c} \approx$ 3 pc is not observed in the central region, but there are very few structures (all clouds) larger than this, and as we will argue later (see Section 4.4) it is likely that the mechanism responsible for driving the turbulence in that region is different.

Overall, the molecular structures of NGC 404 exhibit complex size–linewidth relations, which vary strongly between the central region and molecular ring. It seems that molecular gas is more turbulent in the central region, and thus different sources of turbulence may be present in the two regions. These will be discussed in Section 4.4.

3.3 Multiple-scale mass–size relations

A plot of $\log(M_{\rm c})$ versus $\log(R_{\rm c})$ often provides a useful way to characterize the density structure (e.g. Kauffmann et al. 2010) and fractal nature (e.g. Mandelbrot & Whitrow 1983; Kritsuk, Lee & Norman 2013) of the ISM. Assuming all molecular structures have a power-law mass volume density radial profile $\rho(r) \propto r^{-k}$, the total mass within a given radius is then $M(r) \propto r^{3-k}$. Thus, the lower the slope of the mass–size relation, the more centrally condensed the structure. The power-law index of the $M_{\rm c}$–$R_{\rm c}$ relation may also reflect the fractal dimension $D_{\rm m}$ of the substructures[1] (Mandelbrot & Whitrow 1983). Indeed, as our identified molecular structures can be treated as substructures of a fractal ISM (to zeroth-order approximation; Roman-Duval et al. 2010), it is useful to adopt the fractal dimension $D_{\rm m}$ to describe how fully the molecular structures fill the space of the underlying ISM, i.e. the degree of porosity of the ISM.

Fig. 5 shows the mass–size relations of the molecular structures of the central region, molecular ring, and whole disc of NGC 404, all very tight. The best-fitting mass–size relations of each region are listed in Table 2. Overall, the power-law index for all molecular structures in the whole disc of NGC 404, $D_{\rm m} = 2.11 \pm 0.01$, is similar to (although statistically inconsistent with) that derived for MW clouds ($D_{\rm m} = 2.39 \pm 0.01$; Roman-Duval et al. 2010) and is within the range inferred from observations of nearby galaxies ($1.6 \leq D_{\rm m} \leq 3.0$; Kauffmann et al. 2010; Lombardi, Alves & Lada 2010; Urquhart et al. 2013; Zhang & Li 2017; Li & Zhang 2020). We note that $D_{\rm m} \approx 2.1$ implies a molecular gas mass volume density $\rho_{\rm gas} \propto R_{\rm c}^{-0.9}$ and mass surface density $\Sigma_{\rm gas} \propto R_{\rm c}^{0.1}$. The latter is the usual nearly constant mass surface density, but the former indicates inhomogeneous mass volume densities for the resolved molecular structures of NGC 404.

Interestingly, while clumps and clouds show similar power-law indices in the central region ($D_{\rm m,\,clump} = 2.07 \pm 0.16$ versus $D_{\rm m,\,cloud} = 2.22 \pm 0.10$), clumps exhibit power-law indices much shallower than those of clouds in the molecular ring ($D_{\rm m,\,clump} = 1.65 \pm 0.04$ versus $D_{\rm m,\,cloud} = 2.04 \pm 0.01$). The power-law index $D_{\rm m,\,clump}$ of clumps in the molecular ring (and thus the whole disc) is smaller than 2, suggesting that in that region the larger the clumps, the smaller their mass surface densities. The discrepancy between the power-law indices of clumps and clouds in the molecular ring is similar to that observed in the MW, where $M_{\rm c} \propto R_{\rm c}^{1.6}$ for clumps of sizes $0.01\ {\rm pc} \leq R_{\rm c} \leq 1\ {\rm pc}$ (Kauffmann et al. 2010; Lombardi et al. 2010; Zhang & Li 2017), while $M_{\rm c} \propto R_{\rm c}^{2.2-2.3}$ for clouds of sizes 3 pc

[1]The fractal dimension is an index characterizing fractal patterns or sets, and quantifying their complexity as the ratio of the change in detail to the change in scale. In fractal geometry, a self-similar shape may be split up into N parts, obtainable from the whole by a scaling factor r. The fractal dimension can then be defined mathematically as $D_{\rm m} \equiv -\log N/\log r$ (Mandelbrot & Whitrow 1983), and it need not be an integer.

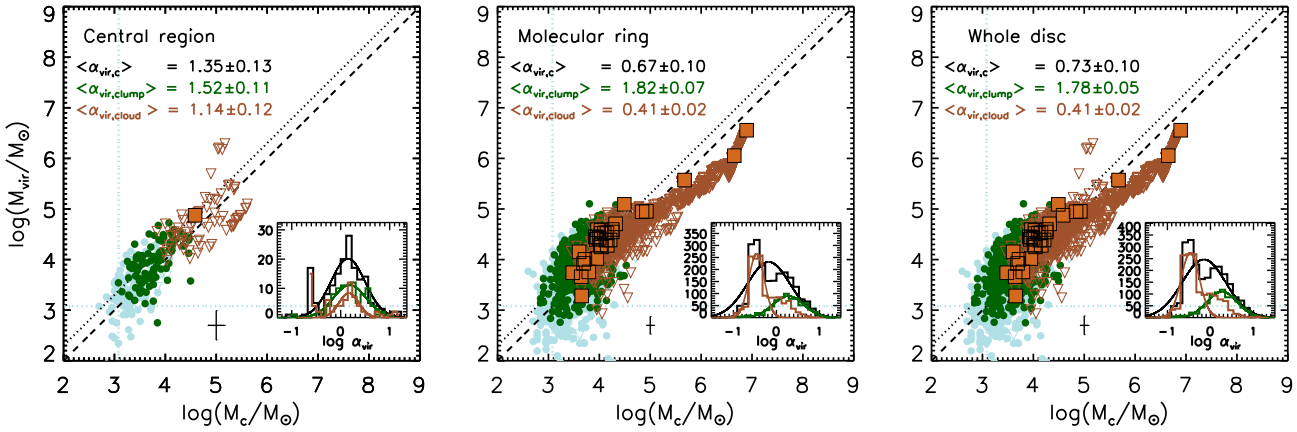

Figure 6. Virial mass–gaseous mass relation of molecular structures in the central region, molecular ring, and whole disc of NGC 404, respectively. Symbols are as for Fig. 4. The black dashed lines show the 1: 1 relations (i.e. $\alpha_{\rm vir,\,c} = 1$) and the black dotted lines the 2: 1 relations (i.e. $\alpha_{\rm vir,\,c} = 2$). The vertical and horizontal blue dotted lines indicate our mass detection limit ($\log(10\delta_{\rm M}/{\rm M}_\odot) = 3.08$; see Section 3.1). In the inset of each panel, the distributions of $\log\alpha_{\rm vir,\,c}$ of all resolved molecular structures (black), clumps (green), and clouds (brown) are shown, with their best lognormal fits overlaid in matching colours. The corresponding mean virial parameters are listed in the legend.

$\leq R_{\rm c} \leq 100$ pc (Roman-Duval et al. 2010; Miville-Deschênes et al. 2016). These trends thus suggest that smaller structures are generally more centrally concentrated (i.e. denser), and that the clumps and clouds in the molecular ring may constitute different populations of molecular structures within the same region. We will discuss the physical origins of the observed mass–size relations of NGC 404 in Section 5.2.

3.4 Multiple-scale virial analyses

A useful tool to quantify the dynamical state of a molecular structure is the virial theorem. The virial parameter

$$\alpha_{\rm vir,c} \equiv M_{\rm vir,c}/M_{\rm c}, \tag{2}$$

which compares the virial mass

$$M_{\rm vir,c} \equiv \frac{5\sigma^2_{\rm obs,los}R_{\rm c}}{G} \tag{3}$$

of the molecular structure to its gaseous mass $M_{\rm c}$, provides a useful measure of its degree of gravitational binding. If $\alpha_{\rm vir,\,c} \ll 1$, the gravitational binding energy is more important than the kinetic energy, and the structure is gravitationally bound. If $\alpha_{\rm vir,\,c} \approx 1$, the kinetic energy is roughly half the gravitational potential energy, and the structure is gravitationally bound and in (gravitational) virial equilibrium. If $\alpha_{\rm vir,\,c} \gg 1$, the kinetic energy is more important than the gravitational energy, and the structure is gravitationally unbound (and thus transient). A virial parameter $\alpha_{\rm vir,\,crit} \approx 2$ is often considered the threshold between gravitationally bound and unbound objects (e.g. Kauffmann, Pillai & Zhang 2013; Kauffmann et al. 2017).

Fig. 6 compares the virial and gaseous masses of molecular structures in the central region, molecular ring, and whole disc of NGC 404. The distributions of the resulting virial parameters of all resolved molecular structures (black line), only resolved clumps (green line), and only clouds (brown line) are also shown in an inset in each panel. The corresponding mean virial parameters are listed in the legend of each panel and Table 2.

Overall, the molecular structures identified in NGC 404 tend to be gravitationally bound, as their mean virial parameter is smaller than unity ($\langle\alpha_{\rm vir,\,c}\rangle = 0.73 \pm 0.10$ for all the molecular structures of the whole disc). However, the distributions of virial parameters vary significantly across the different regions. First, the molecular structures in the central region tend to have much larger virial parameters than those in the molecular ring ($\langle\alpha_{\rm vir,\,c}\rangle = 1.35 \pm 0.13$ versus $\langle\alpha_{\rm vir,\,c}\rangle = 0.67 \pm 0.10$). This is consistent with the fact that gas seems to be more turbulent in the central region (see Section 3.2).

Second, while clumps and clouds have similar virial parameters in the central region ($\langle\alpha_{\rm vir,\,clump}\rangle = 1.52 \pm 0.11$ versus $\langle\alpha_{\rm vir,\,cloud}\rangle = 1.14 \pm 0.12$), clumps have much larger virial parameters than clouds in the molecular ring ($\langle\alpha_{\rm vir,\,clump}\rangle = 1.82 \pm 0.07$ versus $\langle\alpha_{\rm vir,\,cloud}\rangle = 0.41 \pm 0.02$). Indeed, clumps have a $\log(\alpha_{\rm vir,\,c})$ distribution that is clearly distinct from that of clouds in the molecular ring (see middle panel of Fig. 6). It thus seems that the dynamical states of clumps and clouds are regulated by different physical mechanisms in that region. This appears to support the suggestion that clumps and clouds in the molecular ring may constitute different populations of molecular structures (see Section 3.3). Possible reasons for the different dynamical states of clumps and clouds in the molecular ring will be discussed in Section 5.1.

It is also worth noting that the clouds in the molecular ring clearly have a double-peaked, double-Gaussian $\log(\alpha_{\rm vir,\,c})$ distribution, implying two distinct cloud populations. Indeed, 'low-mass' clouds clearly have virial parameters larger than those of 'high-mass' clouds there ($\langle\alpha_{\rm vir,\,cloud}\rangle = 1.10 \pm 0.07$ for $M_{\rm cloud} \leq 10^5$ M$_\odot$ and $\langle\alpha_{\rm vir,\,cloud}\rangle = 0.21 \pm 0.0$ for $M_{\rm cloud} > 10^5$ M$_\odot$).

Fig. 7 shows the dependences of $\alpha_{\rm vir,\,c}$ on $M_{\rm c}$ for the central region, molecular ring, and whole disc of NGC 404. The corresponding power-law indices of the $\alpha_{\rm vir,\,c}$–$M_{\rm c}$ relations are listed in Table 2. There is no correlation between $\alpha_{\rm vir,\,c}$ and $M_{\rm c}$ in the central region (left-hand panel of Fig. 7; Spearman rank correlation coefficient -0.20 ± 0.07), but there is a clear trend in the molecular ring (middle panel of Fig. 7; Spearman rank correlation coefficient -0.75 ± 0.01), where the best-fitting power law is $\alpha_{\rm vir,c} \propto M_{\rm c}^{-0.27\pm0.01}$ (black solid line in the middle panel of Fig. 7). It thus seems that the higher mass molecular structures tend to be more bound than the lower mass ones in the molecular ring (albeit with much scatter). An anticorrelation of $\alpha_{\rm vir,\,c}$ and $M_{\rm c}$ has also been observed in the MW, where $\alpha_{\rm vir,c} \propto\sim M_{\rm c}^{-0.6}$ for Galactic clumps ($R_{\rm c} \leq 5$ pc; Zhang et al. 2016; Veltchev et al. 2018) and $\alpha_{\rm vir,c} \propto M_{\rm c}^{-0.53\pm0.30}$ for ≈8000 molecular clouds across the entire Galactic plane (Miville-Deschênes, Murray & Lee 2017).

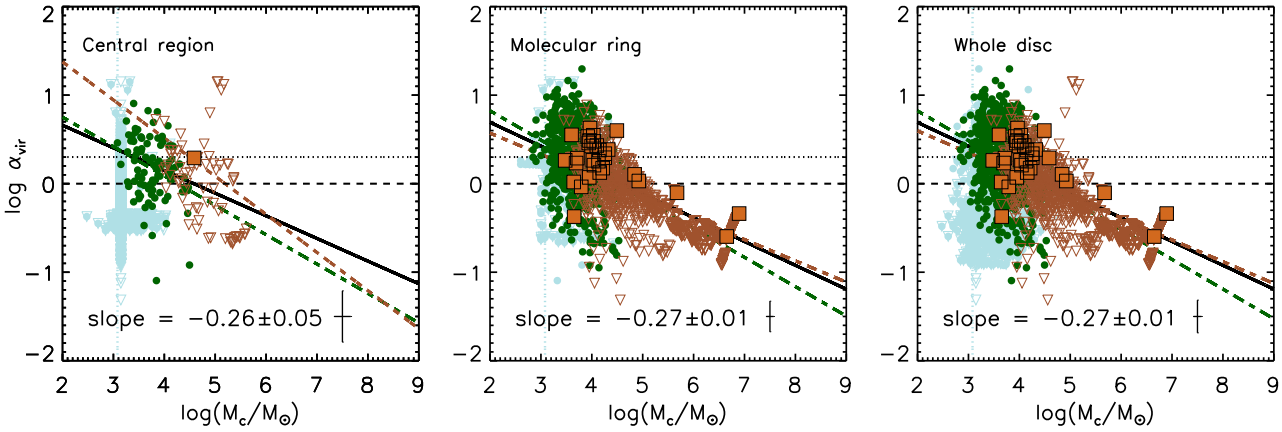

Figure 7. Virial parameter–gaseous mass relation of molecular structures in the central region, molecular ring, and whole disc of NGC 404, respectively. Symbols are as for Fig. 4. The black dashed lines indicate $\alpha_{vir,\,c} = 1$ and the black dotted lines $\alpha_{vir,\,c} = 2$, above which structures are unbound in the absence of other confining mechanisms. In each panel, the black, green, and brown lines show the best-fitting power-law relation of all resolved molecular structures, only resolved clumps (i.e. leaves), and only resolved clouds (i.e. branches and trunks), respectively. The slope of the best-fitting power-law relation of all resolved molecular structures is listed in the legend. The vertical blue dotted lines indicate our mass detection limit ($\log(10\delta_M/M_\odot) = 3.08$; see Section 3.1).

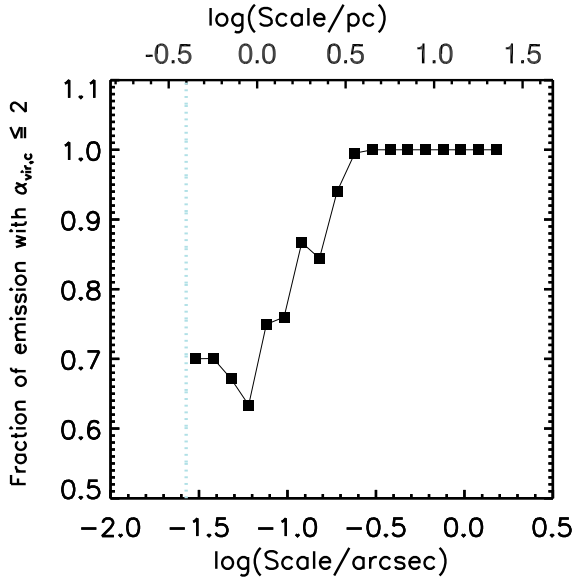

Figure 8. Fraction of emission originating from gravitationally bound (i.e. self-gravitating) structures ($\alpha_{vir,\,c} \leq \alpha_{vir,\,crit} = 2$) as a function of the structures' spatial scales in NGC 404. The fraction grows with scale and saturates at 1 at scales $\gtrsim$3 pc. The blue vertical dotted line indicates our spatial resolution limit of 0.027 arcsec or 0.40 pc (i.e. half the synthesized beam).

We also calculate the fraction of emission originating from gravitationally bound (i.e. $\alpha_{vir,\,c} \leq \alpha_{vir,\,crit} = 2$) structures, and plot this fraction as a function of the structures' spatial scales in Fig. 8. To calculate this, we first measure the virial parameter of the emission contained within each resolved isosurface in the data cube, and define the emission enclosed by an isosurface as self-gravitating if its $\alpha_{vir,\,c} \leq \alpha_{vir,\,crit} = 2$. The fraction of self-gravitating gas is then defined as the ratio of the total emission of the structures with $\alpha_{vir,\,c} \leq \alpha_{vir,\,crit} = 2$ to the total emission of all structures (of any $\alpha_{vir,\,c}$), this within a small range of spatial scales (i.e. a spatial scale 'bin'; see equation 6 of Rosolowsky et al. 2008). Similarly to the aforementioned trend, we find the fraction of self-gravitating gas to be about unity at spatial scales $\gtrsim$3 pc, implying that all these large-scale structures (that are exclusively clouds) are gravitationally bound. However, the fraction decreases for smaller spatial scales and it drops below $\approx$0.7 at spatial scales $\lesssim$1 pc. A similar trend has been observed in the multiple-scale structures of the L1448 molecular cloud in the MW, where only a small fraction of small-scale objects appear to be self-gravitating, but the fraction of gravitationally bound gas grows to unity at larger spatial scales (Rosolowsky et al. 2008; Goodman et al. 2009). We will discuss this scale (and mass) dependence of the gravitational boundedness in more detail in Section 5.1.

4 CLUMP–CLUMP COLLISION MODEL

Cloud–cloud collisions have been proposed in the past as a potentially important mechanism for giant molecular cloud (GMC) formation (e.g. Kwan 1979; Cowie 1980) and star formation (e.g. Dobbs 2008; Tasker & Tan 2009; Dobbs, Burkert & Pringle 2011; Fukui et al. 2021; Maeda et al. 2021; Sano et al. 2021), but they were rejected because of their supposedly long time-scale ($\sim$100 Myr; e.g. Blitz & Shu 1980; Das & Jog 1996; McKee & Ostriker 2007; Dobbs 2008; Hirota et al. 2011). However, recent theory (Gammie, Ostriker & Jog 1991; Tan 2000) and high-resolution hydrodynamic simulations (Tasker & Tan 2009; Li et al. 2018; Wu et al. 2018) suggested that cloud–cloud collisions can be efficient in a differentially rotating disc, where collisions between clouds are driven by galactic shear. In such a shear-driven collision scenario, the collision time-scale is much shorter than traditional estimates (a small fraction, $\approx$1/5, of the orbital time rather than hundreds of Myr; Tasker & Tan 2009). A short collision time-scale has several important implications: (1) cloud–cloud collisions can be crucial to regulate cloud properties such as mass and size (Tasker & Tan 2009; Li et al. 2018); (2) cloud–cloud collisions can be efficient to disturb the ISM and induce turbulence (Wu et al. 2017a, b, 2018; Li et al. 2018).

In this work, instead of cloud–cloud collisions, we will hereafter use the term 'clump–clump collisions', to better reflect the fact that most of the molecular structures we have identified in NGC 404 have sizes much smaller than those of molecular clouds (i.e. $<$10 pc rather than tens of parsecs; Solomon et al. 1987). More importantly, as we will see in Section 4.2, in NGC 404 the collisions between clouds are much less important than those between clumps. In this section, we will thus develop and explore a new simple analytical model

connecting clump–clump collisions to the clump properties and gas turbulence. We will also demonstrate that a key ingredient of our collision model is gravitational instabilities (i.e. a Toomre parameter $Q \lesssim 1$).

4.1 Collision time-scale

We consider an idealized model of a galactic disc that ignores the effects of supernovae, stellar winds, ram pressure, and magnetic fields, i.e. all the physical processes other than galactic rotational shear, gravitational instabilities, and clump–clump collisions. Molecular clumps are assumed to be uniformly distributed over a small (coarse-grained) region of an infinitely thin, two-dimensional disc, and to populate perfectly circular orbits determined by the gravitational potential of the galaxy. We take clump–clump collisions to be any mutual gravitational interaction and merging of clumps. In other words, collisions between clumps are assumed to be completely inelastic, and to lead to the coalescence of the clumps (Fleck 1987; Gammie et al. 1991). Finally, we assume that collisions can only occur between (two) clumps of equal mass; i.e. collisions can be described as 'major mergers', as hydrodynamic simulations have shown that the mass ratio distribution of colliding objects peaks at ≈1 (Li et al. 2018).

Following Tan (2000), we set the velocity of the collision between two clumps to be the shear velocity

$$v_{\rm shear} \equiv v_{\rm shear}(R) = 2Ab \tag{4}$$

and the radius of the collision cross-section to be the tidal radius

$$R_{\rm t} \equiv R_{\rm t}(R) \approx \left(\frac{G}{2A^2}\right)^{1/3} M_{\rm c}^{1/3}, \tag{5}$$

where $A \equiv A(R) = -\frac{R}{2}\frac{{\rm d}\Omega}{{\rm d}R}$ is Oort's constant A evaluated at the galactocentric distance R of the clump ($R_{\rm gal}$ in Table 1), $\Omega \equiv \Omega(R) = V_{\rm circ}/R$ is the angular velocity of orbital circular rotation, $V_{\rm circ} \equiv V_{\rm circ}(R)$ is the circular velocity of the galaxy, and b is the radial distance between the orbits of the two colliding clumps. See Appendix B for a full derivation of the shear velocity and tidal radius. The tidal radius $R_{\rm t}$ rather than the actual clump radius $R_{\rm clump}$ is adopted for the collision cross-section, because two clumps will gravitationally attract (i.e. collide with) each other despite the effects of the galaxy gravity (i.e. the effects of shear and tidal forces) as long as their relative distance is smaller than their tidal radius $R_{\rm t}$. We note that our adopted tidal radius $R_{\rm t}$ is derived by assuming a spherical galaxy mass distribution, and is similar to the Roche limit defined in the literature (e.g. Stark & Blitz 1978).

The clump–clump collision time-scale can then be shown to be

$$t_{\rm coll} \equiv t_{\rm coll}(R) \approx \frac{1}{2AN_{\rm A}R_{\rm t}^2} \approx \frac{A^{1/3}M_{\rm c}^{1/3}}{2^{1/3}G^{2/3}\Sigma_{\rm gas,disc}} \tag{6}$$

(see Appendix B), where $N_{\rm A} \equiv N_{\rm A}(R) = \Sigma_{\rm gas,\,disc}/M_{\rm c}$ is the number surface density of clumps and $\Sigma_{\rm gas,\,disc} \equiv \Sigma_{\rm gas,\,disc}(R)$ is the coarse-grained gaseous mass surface density of the disc.

4.2 Clump mass

We assume here that clumps (i.e. connected, locally peaked structures) are formed from the collisional agglomeration of smaller clumps (i.e. a 'bottom-up' scenario of clump formation; McKee & Ostriker 2007). We first define an accumulation length as the length-scale at which uniformly distributed gas can coalesces into a single centrally peaked clump via clump–clump collisions. The accumulation length can thus be approximated as the average distance between neighbouring clumps:

$$L_{\rm acc,clump} \equiv L_{\rm acc,clump}(R) = (M_{\rm clump}/\Sigma_{\rm gas,disc})^{1/2} = 1/N_{\rm A}^{1/2}. \tag{7}$$

This accumulation length naturally increases during the process of clump–clump collisions, as successive collisions constantly increase the clump mass and size (thereby decreasing the number surface density of clumps).

We then propose that the clumps regulated by collisions should have their accumulation length approximately equal to their tidal radius, i.e. $L_{\rm acc,\,clump} \approx R_{\rm t,\,clump}$. This is intuitively easy to understand. If $L_{\rm acc,\,clump} < R_{\rm t,\,clump}$, the distance between neighbouring clumps is smaller than the tidal radius, and thus the clumps will continue to coalesce with (i.e. gravitationally attract) each other, forming more massive clumps. If $L_{\rm acc,\,clump} > R_{\rm t,\,clump}$, the distance between neighbouring clumps is larger than the tidal radius, and thus the clumps will be pulled apart/sheared away from each other due to the effects of external gravity. Therefore, clump growth via clump–clump collisions naturally ceases when $L_{\rm acc,\,clump} \approx R_{\rm t,\,clump}$.

By posing $L_{\rm acc,clump} = R_{\rm t,clump} \approx \left(\frac{G}{2A^2}\right)^{1/3} M_{\rm c}^{1/3}$ (assuming a spherical galaxy mass distribution, see equation 5), we can rewrite the clump tidal radius and accumulation length as

$$R_{\rm t,clump} \approx L_{\rm acc,clump} \approx G\Sigma_{\rm gas,disc}/2A^2 \equiv \lambda_{\rm coll}(R). \tag{8}$$

This naturally defines a critical collision length $\lambda_{\rm coll} \equiv \lambda_{\rm coll}(R) = G\Sigma_{\rm gas,\,disc}/2A^2$, which is a key length-scale of our collision model. When $R_{\rm t,\,clump} = \lambda_{\rm coll}$ or equivalently $L_{\rm acc,\,clump} = \lambda_{\rm coll}$, then necessarily $R_{\rm t,\,clump} = L_{\rm acc,\,clump}$.

Another way to understand this limitation is to compare the collision time-scale of clumps $t_{\rm coll,\,clump}$ (equation 6) with the shear time-scale

$$t_{\rm shear} \equiv t_{\rm shear}(R) = 1/2A, \tag{9}$$

i.e. the time-scale for gas instabilities to develop and grow before the clumps are sheared apart (see Kruijssen & Longmore 2014; Liu et al. 2021). If $t_{\rm coll,\,clump} < t_{\rm shear}$, collisions dominate over shear, and clumps can collide and merge into more massive clumps. If $t_{\rm coll,\,clump} > t_{\rm shear}$, shear dominates over collisions, and collisions between clumps are disrupted by shear. Hence, clumps regulated by clump–clump collisions should have $t_{\rm coll} \approx t_{\rm shear} = 1/2A$, which is equivalent to $L_{\rm acc,\,clump} \approx R_{\rm t,\,clump}$.

A simple scenario of clump formation therefore emerges, whereby small-scale clumps initially form and then collide and coalesce into more massive clumps, until the clumps' tidal radii reach $\lambda_{\rm coll}$. The resulting clump mass ($M_{\rm c,\,coll}$) is thus directly obtained:

$$\begin{aligned} M_{\rm clump} &\equiv M_{\rm clump}(R) = \Sigma_{\rm gas,\,disc}\,\lambda_{\rm coll}^2 \approx (2A^2/G)\,\lambda_{\rm coll}^3 \\ &\approx G^2\Sigma_{\rm gas,disc}^3/4A^4 \equiv M_{\rm c,coll}(R) \end{aligned} \tag{10}$$

(see Section 6.1 for a more detailed discussion). The typical mass of clumps formed via clump–clump collisions is thus determined only by galaxy properties ($\Sigma_{\rm gas,\,disc}$ and A).

4.3 First comparison to NGC 404

We now apply our clump–clump collision model to NGC 404. We first compare the clump–clump collision time-scale $t_{\rm coll,\,clump}$ (equation 6) with the shear time-scale $t_{\rm shear}$ (equation 9) at each galactocentric radius (see panel a of Fig. 9). To achieve this, we adopt radially varying Ω and A (see Fig. B1), $\Sigma_{\rm gas,\,disc}$ (see Fig. B2), and median clump mass $M_{\rm clump}$ (which also happens to be the most common clump mass; see panel b of Fig. 9). In the central region, the collision time-scale is much longer than the shear time-scale (i.e. $t_{\rm coll,\,clump}$

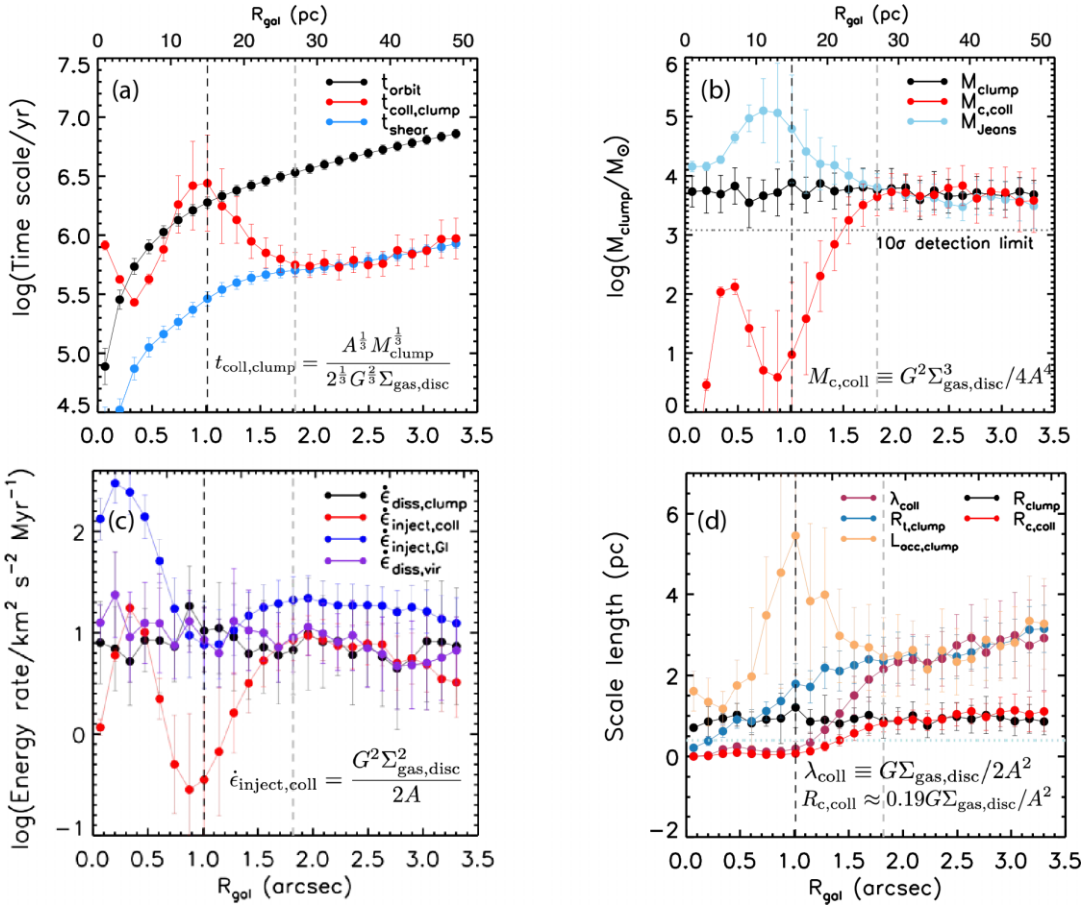

Figure 9. Radial variation of the predicted collision time-scale ($t_{\rm coll,\,clump}$), clump mass ($M_{\rm c,\,coll}$), turbulence energy injection rate ($\dot{\epsilon}_{\rm inject,coll}$), and clump size ($R_{\rm c,\,coll}$), respectively, of our clump–clump collision model, averaged over galactocentric radius bins of 2 pc in NGC 404. In each panel, the black vertical dashed line indicates the boundary ($R_{\rm gal} = 15$ pc) between the central region and molecular ring, while the grey vertical dashed line indicates the galactocentric distance ($R_{\rm gal} = 27$ pc) beyond which the molecular gas disc is no longer gravitationally stable (i.e. Toomre parameter's $Q \leq 1$ at $R_{\rm gal} \geq 27$ pc; see Section 4.5). The error bars of each quantity indicate the 1σ scatter of the values within each radial bin (not the uncertainty on the mean within each bin, which is much smaller). Panel (a): comparisons of the orbital time-scale $t_{\rm orbit}$ (equation 11), our model-predicted clump–clump collision time-scale $t_{\rm coll,\,clump}$ (equation 6), and the shear time-scale $t_{\rm shear}$ (equation 9) at each galactocentric radius. The clump–clump collision time-scale $t_{\rm coll,\,clump}$ is much smaller than the orbital time-scale $t_{\rm orbit}$ but is in good agreement with the shear time-scale $t_{\rm shear}$ in the molecular ring (especially at $R_{\rm gal} \geq 27$ pc where $Q \leq 1$; see Section 4.2). Panel (b): comparisons of the observed median clump mass $M_{\rm clump}$, which also happens to be the most common clump mass, our model-predicted clump mass $M_{\rm c,\,coll}$ (equation 10), and the Jeans mass $M_{\rm Jeans}$ (equation 25) at each galactocentric radius. The black horizontal dotted line indicates our mass detection limit ($\log(10\delta_{\rm M}/{\rm M}_{\odot}) = 3.08$; see Section 3.1). The median/most common clump mass $M_{\rm clump}$ is in good agreement with the predicted clump mass $M_{\rm c,\,coll}$ (and the Jeans mass $M_{\rm Jeans}$) in the molecular ring (especially at $R_{\rm gal} \geq 27$ pc where $Q \leq 1$; see Section 4.2). Panel (c): comparisons of the observed median energy dissipation rate (per unit mass) of clumps $\dot{\epsilon}_{\rm diss,clump}$ (equation 14), our model-predicted energy injection rate (per unit mass) due to clump–clump collisions $\dot{\epsilon}_{\rm inject,coll}$ (equation 13), the predicted energy injection rate (per unit mass) from gravitational instabilities $\dot{\epsilon}_{\rm inject,GI}$ (equation 28), and the median virial energy dissipation rate (per unit mass) of clumps $\dot{\epsilon}_{\rm diss,vir}$ (equation 33) at each galactocentric radius. The observed median energy dissipation rate $\dot{\epsilon}_{\rm diss,clump}$ is consistent with the median virial energy dissipation rate $\dot{\epsilon}_{\rm diss,vir}$ at all radii, but it agrees well with our predicted energy injection rate $\dot{\epsilon}_{\rm inject,coll}$ and is within one order of magnitude of $\dot{\epsilon}_{\rm inject,GI}$ in the molecular ring only (especially at $R_{\rm gal} \geq 27$ pc where $Q \leq 1$; see Section 4.4). Panel (d): comparison of the observed median clump size $R_{\rm clump}$, which also happens to be the most common clump size, and our model-predicted clump size $R_{\rm c,\,coll}$ (equation 36), and comparisons of the observed clump tidal radius $R_{\rm t,\,clump}$ (equation B3), accumulation length $L_{\rm acc,\,clump}$ (equation 7), and collision critical length $\lambda_{\rm coll}$ (equation 8) at each galactocentric radius. The blue horizontal dotted line indicates our spatial resolution limit of 0.027 arcsec or 0.40 pc (i.e. half the synthesized beam). The clump tidal radius $R_{\rm t,\,clump}$, accumulation length $L_{\rm acc,\,clump}$, and collision critical length $\lambda_{\rm coll}$ are consistent with each other (see Section 4.2) in the molecular ring (especially at $R_{\rm gal} \geq 27$ pc where $Q \leq 1$; see Section 5.2), similarly for the observed clump size $R_{\rm clump}$ and predicted clump size $R_{\rm c,\,coll}$. The clump collision time-scale $t_{\rm coll,\,clump}$, tidal radius $R_{\rm t,\,clump}$, and accumulation length $L_{\rm acc,\,clump}$ are calculated using the median clump mass $M_{\rm clump}$ at each galactocentric radius (see panel b). The quantities $t_{\rm coll,\,clump}$, $M_{\rm clump}$, $\dot{\epsilon}_{\rm diss,clump}$, $\dot{\epsilon}_{\rm diss,vir}$, $R_{\rm clump}$, $R_{\rm t,\,clump}$, and $L_{\rm acc,\,clump}$ are calculated for resolved clumps only.

$> t_{\rm shear}$), implying that clump–clump collisions are not important in this region. In the molecular ring, however, the collision time-scale decreases significantly with increasing galactocentric distance, and it becomes comparable to the shear time-scale at $R_{\rm gal} \geq 27$ pc, where most (≈ 87 per cent) of the molecular gas in the molecular ring is located (see the grey vertical dashed line in each panel of Fig. 9). This implies clump–clump collisions must be important in the molecular ring.

Panel (a) of Fig. 9 also shows the orbital time-scale of clumps

$$t_{\rm orbit} \equiv t_{\rm orbit}(R) = 2\pi/\Omega \tag{11}$$

as a function of the galactocentric distance R (i.e. $R_{\rm gal}$) in NGC 404. The orbital time-scales of clumps are generally longer than their collision time-scales. This is particularly the case in the molecular ring, where at $R_{\rm gal} \geq 27$ pc the clump–clump collision time-scales are only 0.1–0.2 of the orbital time-scales. Our observations are thus consistent with simulation results ($t_{\rm coll} \approx 0.2\, t_{\rm orbit}$; Tasker & Tan 2009; Dobbs, Pringle & Duarte-Cabral 2015; Li et al. 2018), suggesting clump–clump collisions can indeed be frequent in galactic discs with strong shear. We also note that, for a flat circular velocity curve ($\Omega = 2A$), the shear time-scale $t_{\rm shear} = 1/2A = t_{\rm orbit}/2\pi$, and thus in the molecular ring (where the rotation curve is almost flat)

$$t_{\rm coll,clump} \approx t_{\rm shear} \approx t_{\rm orbit}/2\pi, \tag{12}$$

which naturally accounts for our finding that $t_{\rm coll,\,clump}/t_{\rm orbit} \approx 0.1$–$0.2$ in the molecular ring.

The observed clump accumulation length $L_{\rm acc,\,clump}$ (equation 7) and tidal radius $R_{\rm t,\,clump}$ (equation 5) are also compared in panel (d) of Fig. 9 (calculated again using the median clump mass $M_{\rm clump}$ at each galactocentric radius; see panel b of Fig. 9). Again, the clump accumulation length is much larger than the clump tidal radius in the central region, but the two are comparable in the molecular ring (especially at $R_{\rm gal} \geq 27$ pc). This again suggests that clump–clump collisions are important in the molecular ring but not in the central region.

We also compare our predicted clump mass $M_{\rm c,\,coll}$ (equation 10) with the observed (median) clump masses $M_{\rm clump}$, and our predicted clump tidal radius $\lambda_{\rm coll}$ (equation 8) with the observed (median) clump tidal radii $R_{\rm t,\,clump}$ at each galactocentric distance. As shown in panels (b) and (d) of Fig. 9, our model successfully accounts for the measurements in the molecular ring, especially at $R_{\rm gal} \geq 27$ pc, where $M_{\rm clump} \approx M_{\rm c,\,coll}$ and $R_{\rm t,\,clump} \approx L_{\rm acc,\,clump} \approx \lambda_{\rm coll}$. The good match between the predicted and observed clump masses in the molecular ring can also be seen in the middle panel of Fig. 3, where our predicted clump mass $M_{\rm c,\,coll}$ for the molecular ring (the red vertical dashed line) agrees well with the observed most common clump mass (i.e. the turn-over mass at $M_{\rm clump} \approx 4000\ {\rm M}_\odot$).

Having said that, our collision model leads to significant underestimates of the clump masses in the central region. This significant mismatch between the model $M_{\rm c,\,coll}$ (or $\lambda_{\rm coll}$) and the observed (median) $M_{\rm clump}$ (or $R_{\rm t,\,clump}$) in the central region is unlikely to be due to the limited spatial resolution and/or sensitivity of our data, as the clumps in the central region have deconvolved sizes larger than our spatial resolution limit (see the blue horizontal dotted line in panel d of Fig. 9) and masses well above our detection limit [$\log(10\delta_{\rm M}/{\rm M}_\odot) = 3.08$; see the grey horizontal dotted line in panel (b) of Fig. 9].

Overall, the good match between our predictions and the observations in the molecular ring suggests that clump–clump collisions are an important mechanism regulating clumps in regions where $t_{\rm coll,\,clump} \leq t_{\rm shear}$. Other physical mechanisms are required to explain the formation of massive clumps in the central region, where $t_{\rm coll,\,clump} > t_{\rm shear}$. It is interesting to note that the clumps in the central region nevertheless have masses and sizes similar to those in the molecular ring (see panels b and d of Fig. 9). We will discuss this fact in Section 6.3.

So far, we have only considered the importance of collisions between clumps, but are collisions between clouds also likely to be important? The answer is probably no. This is because $t_{\rm coll} \propto M_{\rm c}^{1/3}$ (see equation 6), so clouds tend to have much longer collision time-scales than clumps. We have also seen that most clumps have already reached a critical state whereby $t_{\rm coll,\,clump} \approx t_{\rm shear}$ in the molecular ring (and $t_{\rm coll,\,clump} > t_{\rm shear}$ in the central region). Clouds, which by definition contains several clumps, should therefore have $t_{\rm coll,\,cloud} > t_{\rm shear}$ everywhere. In other words, it is likely that clouds in NGC 404 will be pulled away from each other (by tidal and shear forces) before they have a chance to collide and coalesce with each other. Cloud–cloud collisions are therefore likely to be much less important than clump–clump collisions in NGC 404. Hereafter, we will thus ignore cloud–cloud collisions, and only discuss clump–clump collisions.

4.4 Turbulence driven by clump–clump collisions

High-resolution hydrodynamic simulations suggest that frequent clump–clump collisions can be an important source of turbulence in galaxies (e.g. Agertz et al. 2009; Namekata & Habe 2011; Tan, Shaske & Van Loo 2013; Li 2017b; Li et al. 2018; Wu et al. 2018). According to these simulations, clump–clump collisions alone can provide sufficient energy to maintain the observed level of turbulence in the ISM (e.g. Aumer et al. 2010; Li 2017b; Wu et al. 2017a, b, 2018). In this section, we thus explore the impact of clump–clump collisions on turbulence, by relating the turbulent energy injected via clump–clump collisions to the kinetic energy of ordered differential-rotation motions in the disc. In the process, we will show that our model of collision-induced turbulence matches well the observed turbulence in the molecular ring of NGC 404.

4.4.1 Energy injection rate by clump–clump collisions

We have implicitly assumed that the collisions between clumps are inelastic. This assumption is reasonable, as theoretical and simulation works suggest that clumps in a differentially rotating galactic disc can have inelastic collisions, which give rise to viscosity and lead to energy dissipation and the transport of angular momentum (e.g. Jog & Ostriker 1988; Ozernoy, Fridman & Biermann 1998; Vollmer & Duschl 2001; Williamson & Thacker 2012; Li 2017b). Given inelastic collisions, all the available kinetic energy is dissipated into turbulence, i.e. the kinetic energy extracted from galactic differential rotation by clump–clump collisions is completely converted to turbulence. The average rate of 'turbulent energy' injection due to clump–clump collision (per unit mass), $\dot{\epsilon}_{\rm inject,coll}$, can then be expressed as

$$\begin{aligned}\dot{\epsilon}_{\rm inject,coll}(R) &= \frac{1}{t_{\rm coll}} \frac{2\int_0^{R_{\rm t,clump}} \left(\frac{1}{2} M_{\rm clump} v_{\rm shear}^2(b)\right) z_{\rm coll}(b)\,{\rm d}b}{2\int_0^{R_{\rm t,clump}} M_{\rm clump}\, z_{\rm coll}(b)\,{\rm d}b} \\ &\approx \frac{1}{t_{\rm coll}} \frac{(2A)^3 N_{\rm A} \int_0^{R_{\rm t,clump}} b^3\,{\rm d}b}{Z_{\rm coll}} \approx 2A^3\, N_{\rm A}\, R_{\rm t,clump}^4 \\ &\approx 2A^3 N_{\rm A} \lambda_{\rm coll}^4 \approx (G\Sigma_{\rm gas,disc})^2/2A, \end{aligned} \tag{13}$$

where $z_{\rm coll}(b) = N_{\rm A} v_{\rm shear}(b) = N_{\rm A}(2Ab)$ is the collision rate per unit length and $N_{\rm A}$ is approximately constant over a region of radius $R_{\rm t,\,clump}$ (see equations B4–B6), and we have used $R_{\rm t,\,clump} \approx \lambda_{\rm coll}$ as demonstrated in Section 4.2 (see equation 8). The factor of 2 in both numerator and denominator of equation (13) accounts for clumps either catching up with other clumps at larger $R_{\rm gal}$ or being caught up by other clumps at smaller $R_{\rm gal}$. As $N_{\rm A} \propto M_{\rm clump}^{-1}$ and $R_{\rm t} \propto M_{\rm clump}^{1/3}$, $\dot{\epsilon}_{\rm inject,coll} \propto M_{\rm clump}^{1/3}$, suggesting that collisions between more massive clumps are more effective at injecting turbulent energy. We note that our derived $\dot{\epsilon}_{\rm inject,coll}$ again comprises galaxy properties only ($\Sigma_{\rm gas,\,disc}$ and A) and therefore does not depend on the clump properties.

The question is then whether the energy injected by clump–clump collisions in NGC 404 is sufficient to maintain the observed level of turbulence. An important parameter to quantify the properties of turbulence is the rate at which energy is dissipated in the turbulent

cascade (per unit mass), or equivalently the rate at which energy is transferred from large to small scales (per unit mass), $\dot{\epsilon}_{\rm diss}$ (Mivile-Deschênes et al. 2017). This can be estimated for each clump as the total kinetic energy (per unit mass) divided by the dynamical time ($t_{\rm dyn} = 2R_{\rm c}/\sigma_{\rm obs,\,los}$; Mac Low et al. 1998; Mac Low 1999):

$$\dot{\epsilon}_{\rm diss,clump} = \frac{1}{M_{\rm clump}} \frac{\frac{1}{2}M_{\rm clump}\sigma^2_{\rm obs,los}}{2R_{\rm clump}/\sigma_{\rm obs,los}} = \frac{1}{4}\frac{\sigma^3_{\rm obs,los}}{R_{\rm clump}}. \quad (14)$$

If turbulence is maintained by clump–clump collisions, we should expect

$$\dot{\epsilon}_{\rm diss,clump} \approx \dot{\epsilon}_{\rm inject,coll}. \quad (15)$$

Comparison to NGC 404. Panel (c) of Fig. 9 compares the energy injection rate from clump–clump collisions $\dot{\epsilon}_{\rm inject,coll}$ to the clumps' turbulent energy dissipation rate $\dot{\epsilon}_{\rm diss,clump}$ in NGC 404. The latter is derived by utilizing the observed median clump size $R_{\rm clump}$ and median clump velocity dispersion $\sigma_{\rm obs,\,los}$ at each radius. We find the energy injection rates of collisions are sufficient to balance the turbulent energy dissipation rates of the clumps in the molecular ring and the inner parts ($R_{\rm gal} \lesssim 8$ pc) of the central region, but not in the outer parts (8 pc $\lesssim R_{\rm gal} \lesssim$ 15 pc) of the central region.

4.4.2 *Size–linewidth relation regulated by clump–clump collisions*

To check whether the gas turbulence is indeed triggered by clump–clump collisions, one must also compare the observed size–linewidth relation with that predicted from the collision model. This is because the size–linewidth relation is often interpreted as a signature of turbulent motions, representing the length-scales of velocity correlations within a turbulent flow (e.g. Falgarone & Phillips 1991; Elmegreen & Falgarone 1996; Roman-Duval et al. 2010). Energy is generally considered to be fed into the turbulent medium on its largest spatial scale (the turbulence driving scale $L_{\rm D}$), and to be transmitted through the so-called 'turbulent cascade' to smaller and smaller spatial scales l, until the energy reaches a (very small) scale at which it is dissipated into heat (e.g. Bodenheimer 2011). If turbulence is maintained by clump–clump collisions, the turbulence driving scale should be equal to the critical collision length, i.e.

$$L_{\rm D,coll} \approx \lambda_{\rm coll} = G\Sigma_{\rm gas,disc}/2A^2. \quad (16)$$

This is because $\lambda_{\rm coll}$ is the maximum distance within which clumps can collide with each other and thus trigger turbulence.

As turbulence has self-similar properties only on spatial scales below the driving scale, the size–linewidth relation should exhibit a power law on spatial scales $l < L_{\rm D}$, and then turn over and flatten at $l \geq L_{\rm D}$ (e.g. Blitz & Rosolowsky 2006). If we assume the turbulent energy due to clump–clump collisions $\dot{\epsilon}_{\rm inject,coll}$ cascades down to small spatial scales with a constant energy dissipation rate (per unit mass), i.e. if we assume a Kolmogorov spectrum of turbulence (e.g. Kolmogorov 1941; Lighthill 1955; Kritsuk et al. 2007; Mivile-Deschênes et al. 2017), we can pose

$$\dot{\epsilon}_{\rm diss} \equiv \frac{1}{4}\frac{\sigma^3_{\rm obs,los}(l)}{l} = {\rm constant} = \dot{\epsilon}_{\rm inject,coll} \quad {\rm for}\ l \leq L_{\rm D} \approx \lambda_{\rm coll} \quad (17)$$

(see equation 14). Combining this with equations (13) and (16), we can infer the velocity dispersion of clumps (and clouds) due to clump–clump (or cloud–cloud) collisions $\sigma_{\rm c,\,coll}$ at all spatial scales:

$$\sigma_{\rm c,coll} = \begin{cases} \left(2G^2\Sigma^2_{\rm gas,disc}/A\right)^{1/3} R_{\rm c}^{1/3} & {\rm if}\ R_{\rm c} \lesssim L_{\rm D} \approx \lambda_{\rm coll}; \\ G\Sigma_{\rm gas,disc}/A \equiv \sigma_{\rm max,coll} & {\rm if}\ R_{\rm c} \gtrsim L_{\rm D} \approx \lambda_{\rm coll}. \end{cases} \quad (18)$$

Hence, if clump–clump collisions constitute a major driver of turbulence, the size–linewidth relation is linked to the galaxy properties $\Sigma_{\rm gas,\,disc}$ and A only.

Comparison to NGC 404. The red dashed line shown in each panel of Fig. 4 shows our predicted size–linewidth relation using equation (18), with a slope of 1/3, a flattening at a clump/cloud radius $L_{\rm D} \approx \lambda_{\rm coll} = G\Sigma_{\rm gas,\,disc}/2A^2$ (equation 16), and a maximum clump/cloud velocity dispersion $\sigma_{\rm max,\,coll} = G\Sigma_{\rm gas,\,disc}/A$, where the molecular gas mass surface density $\Sigma_{\rm gas,\,disc}$ and Oort's constant A were spatially averaged within each region (i.e. the central region, molecular ring, and whole disc, respectively). Our predicted size–linewidth relation (with no free parameter!) strongly resembles the observed $R_{\rm c}$–$\sigma_{\rm obs,\,los}$ trend in the molecular ring (see the middle panel of Fig. 4), including its slope, normalization, turn-over scale, and plateau. This lends strong support to our conjecture that the observed turbulence in the molecular ring of NGC 404 is maintained by clump–clump collisions.

In the central region, although the energy injection rate due to collisions appears to be sufficient to balance the turbulent energy dissipation rate of the clumps in the very inner parts ($R_{\rm gal} \leq$ 8 pc; see panel c of Fig. 9), the observed velocity dispersions are much larger than those predicted by our collision model (and a turn-over at the scale predicted is not observed). Mechanisms other than collisions are therefore required to explain the higher level of turbulence (and larger turbulence driving scale) in that region. We will compare clump–clump collisions with stellar feedback in Section 6.2, and discuss the possibility of clump migration as a source of turbulence in the central region in Section 6.3.

4.4.3 *Vertical support from collision-induced turbulence*

If the disc velocity dispersion $\sigma_{\rm gas,\,disc}$ is driven by clump–clump collisions and maintains the gas disc in vertical equilibrium, it should be approximately equal to (or smaller than) the maximum velocity dispersion possibly maintained by clump–clump collisions ($\sigma_{\rm max,\,coll}$; see equation 18), i.e.

$$\sigma_{\rm gas,disc} \approx \sigma_{\rm max,coll} \approx G\Sigma_{\rm gas,disc}/A. \quad (19)$$

In addition, as the gas disc scale height $h_{\rm gas,\,disc}$ should be comparable to the spatial scale on which the turbulence is driven (e.g. Blitz & Rosolowsky 2006; Swinbank et al. 2011; Hughes et al. 2013; Kim & Ostriker 2015), we also expect

$$h_{\rm gas,disc} \approx L_{\rm D} \approx \lambda_{\rm coll} = G\Sigma_{\rm gas,disc}/2A^2 \quad (20)$$

(see equation 16). Therefore, if the turbulent kinetic energy that supports the gas disc in vertical equilibrium is maintained by clump–clump collisions, the disc velocity dispersion $\sigma_{\rm gas,\,disc}$ and vertical scale height $h_{\rm gas,\,disc}$ are again linked only to the galaxy properties $\Sigma_{\rm gas,\,disc}$ and A.

Comparison to NGC 404. In NGC 404, we do find that the observed one-dimensional (coarse-grained) gas disc velocity dispersions $\sigma_{\rm gas,\,disc}$ agree well with our predicted maximum velocity dispersions $\sigma_{\rm max,\,coll}$ in the molecular ring (especially at $R_{\rm gal} \geq 27$ pc; see the middle panel of Fig. 10), where $\sigma_{\rm gas,\,disc}(R)$ was obtained again by averaging measurements within galactocentric annuli of increasing $R_{\rm gal}$ (with a radial bin size of 2 pc and a fixed position angle $PA = 1^\circ$ and inclination angle $i = 9.3^\circ$). A very good agreement between our estimated scale height $h_{\rm gas,\,disc}$ and the turbulence driving scale $L_{\rm D} \approx \lambda_{\rm coll}$ is also found in the molecular ring (see the right-hand panel of Fig. 10). We note that for this purpose we estimated the disc

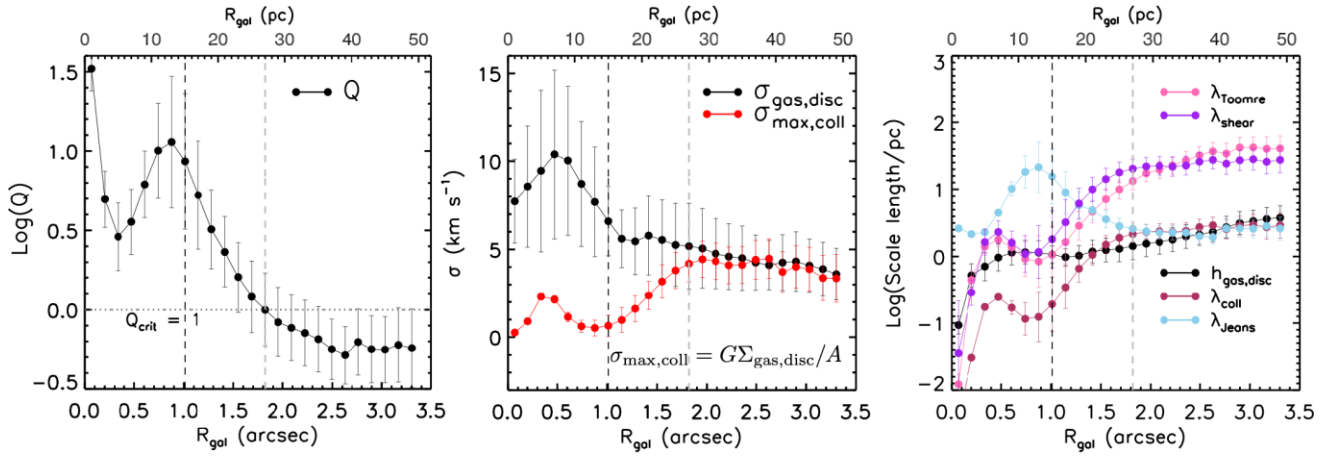

Figure 10. Radial variations of molecular gas disc properties of NGC 404, averaged over galactocentric radius bins of 2 pc. In each panel, the black vertical dashed line indicates the boundary ($R_{\rm gal}$ = 15 pc) between the central region and molecular ring, while the grey vertical dashed line indicates the galactocentric distance ($R_{\rm gal}$ = 27 pc) beyond which the molecular gas disc is no longer gravitationally stable (i.e. $Q \leq 1$ at $R_{\rm gal} \geq 27$ pc). The error bars of each quantity indicate the 1σ scatter of the values within each radial bin (not the uncertainty on the mean within each bin, that is much smaller). Left-hand panel: Toomre parameter Q (equation 22) as a function of galactocentric radius. The horizontal black dotted line indicates $Q_{\rm crit} = 1$. The Toomre parameter $Q \gg 1$ in the central region but decreases significantly in the molecular ring, and drops below unity at $R_{\rm gal} \geq 27$ pc. Centre: Comparison of the observed coarse-grained velocity dispersion of the molecular gas disc $\sigma_{\rm gas,\,disc}$ and our predicted maximum velocity dispersion sustained by clump–clump collisions $\sigma_{\rm max,\,coll}$ (equation 18) at each galactocentric radius. We note that $\sigma_{\rm gas,\,disc} \gg \sigma_{\rm max,\,coll}$ in the central region, while $\sigma_{\rm gas,\,disc} \approx \sigma_{\rm max,\,coll}$ in the molecular ring (especially at $R_{\rm gal} \geq 27$ pc where $Q \leq 1$). Right-hand panel: Comparisons of the molecular gas disc scale height $h_{\rm gas,\,disc}$ (equation 21), collision critical length $\lambda_{\rm coll}$ (equation 8), and Jeans length $\lambda_{\rm Jeans}$ (equation 24), and comparison of the Toomre length $\lambda_{\rm Toomre}$ (equation 29) and shear length $\lambda_{\rm shear}$ (equation 32) at each galactocentric radius. The scale height $h_{\rm gas,\,disc} \approx \lambda_{\rm coll} \approx \lambda_{\rm Jeans}$ and $\lambda_{\rm Toomre} \approx \lambda_{\rm Shear}$ in the molecular ring of NGC 404 (especially at $R_{\rm gal} \geq 27$ pc where $Q \leq 1$; see Sections 4.5 and 5.1, respectively).

scale height as

$$h_{\rm gas,disc} \approx \sigma_{\rm gas,disc}/\sqrt{4\pi G \rho_*}, \tag{21}$$

which assumes a disc in vertical equilibrium (e.g. Koyama & Ostriker 2009), where $\rho_* \equiv \rho_*(R)$ is the stellar mass volume density at each galactocentric radius, here taken from the stellar mass model presented in Nguyen (2017) and Davis et al. (2020).

In the central region, however, the observed disc velocity dispersions $\sigma_{\rm gas,\,disc}$ and disc scale heights $h_{\rm gas,\,disc}$ are significantly larger than the model predictions, suggesting other sources of turbulence are required in that region.

4.5 Gravitational instabilities as the onset of clump–clump collisions

The above sections have shown that clump–clump collisions play an important role to regulate clump properties and gas turbulence in the molecular ring of NGC 404. In the central region, however, the clump masses (see panel b of Fig. 9) and velocity dispersions (see left-hand panel of Fig. 4) are significantly underestimated by our collision model. A question then arises: under what circumstance does our clump–clump collision model hold? Numerical simulations have shown that gravitational instabilities coupled with galactic shear is probably the only mechanism able to generate a population of clumps that undergo mutual gravitational interactions and merging (Kim & Ostriker 2007; Agertz et al. 2009; Dekel, Sari & Ceverino 2009b; Aumer et al. 2010; Elmegreen & Burkert 2010; Agertz, Romeo & Grisdale 2015; Goldbaum et al. 2015). It has been further shown that gravitational instabilities are of great importance to generate turbulent motions from ordered circular motions (e.g. Agertz et al. 2009; Dekel et al. 2009a; Goldbaum et al. 2016; Krumholz & Burkhart 2016). Indeed, gas would remain on approximately circular orbits without the onset of gravitational instabilities (Agertz et al. 2009).

According to the standard analysis, a thin rotating gaseous disc becomes unstable if the Toomre parameter Q is smaller than a critical value $Q_{\rm crit}$ that is approximately unity (Toomre 1964; Lin & Pringle 1987; Binney & Tremaine 2008):

$$Q \equiv Q(R) = \frac{\sigma_{\rm gas,disc}\kappa}{\pi G \Sigma_{\rm gas,disc}} < Q_{\rm crit} \approx 1, \tag{22}$$

where $\kappa \equiv \kappa(R) = \left(R\frac{d\Omega^2(R)}{dR} + 4\Omega^2(R)\right)^{\frac{1}{2}}$ is the epicyclic frequency. Fig. B1 shows the dependence of κ on the galactocentric distance R (i.e. $R_{\rm gal}$) in NGC 404.

As shown in the left-hand panel of Fig. 10, the central region of NGC 404 ($R_{\rm gal} < 15$ pc) has Q significantly larger than unity at all radii (Q = 3–30), while the molecular ring ($R_{\rm gal} \geq 15$ pc) has Q smaller than unity at $R_{\rm gal} \geq 27$ pc, where most ($\approx$ 87 per cent) of the molecular gas in the molecular ring is located. This suggests the central region is strongly gravitationally stable, while the molecular ring is gravitationally unstable or only marginally stable. The observed trends of the Toomre parameter Q in NGC 404 seem to suggest that gravitational instabilities can indeed trigger clump–clump collisions, as already pointed out by many numerical simulations (e.g. Agertz et al. 2009, 2015; Dekel et al. 2009b; Elmegreen & Burkert 2010; Goldbaum et al. 2015). Indeed, we find a much better match between our model predictions and the observations at $R_{\rm gal} \geq 27$ pc where $Q \leq 1$ (see e.g. all the panels of Fig. 9 and the middle and right-hand panels of Fig. 10).

More importantly, using $\sigma_{\rm gas,\,disc} \approx \sigma_{\rm max,\,coll}$ (see equation 19) and assuming a flat circular velocity curve ($\kappa = \sqrt{2}\Omega = 2\sqrt{2}A$), as is approximately the case in the molecular ring of NGC 404 (see

Fig. B1), we can rewrite the Toomre parameter (equation 22) as

$$Q_{\rm coll} \equiv Q_{\rm coll}(R) \approx \frac{\sigma_{\rm max,coll}\,\kappa}{\pi G \Sigma_{\rm gas,disc}} \approx \frac{(G\Sigma_{\rm gas,disc}/A)(2\sqrt{2}A)}{\pi G \Sigma_{\rm gas,disc}} = \frac{2\sqrt{2}}{\pi} \approx 1. \quad (23)$$

It thus seems that, if the velocity dispersions supporting a gas disc are generated by clump–clump collisions, this disc will necessarily self-regulate and remain marginally gravitationally stable (i.e. $Q \approx 1$). Conversely, for a gas disc with $Q \gg 1$, the disc velocity dispersions $\sigma_{\rm gas,\,disc}$ are expected to be significantly larger than the maximum velocity dispersions generated by clump–clump collisions $\sigma_{\rm max,\,coll}$, as is indeed the case in the central region of NGC 404 (see middle panel of Fig. 10). Thus, other mechanisms are required to stir the turbulence in such a disc (e.g. clump migration, stellar feedback, and gas inflows/outflows; Krumholz & Kruijssen 2015).

A simple criterion to ascertain whether clump–clump collisions are efficient was given in Section 4.2, a comparison of the collision time-scale $t_{\rm coll,\,clump}$ (equation 6) and shear time-scale $t_{\rm shear}$ (equation 9), i.e. $t_{\rm coll,\,clump} \leq t_{\rm shear}$. But how does this criterion imply a gas disc that is gravitationally unstable or marginally stable (i.e. a gas disc with $Q \lesssim 1$)? For a thin gas disc, the length-scale at which gravitational fragmentation occurs is approximately the two-dimensional Jeans length (Bournaud et al. 2010; Swinbank et al. 2011, 2015; Dobbs & Pringle 2013)

$$\lambda_{\rm Jeans} \equiv \lambda_{\rm Jeans}(R) \approx \pi\sigma^2_{\rm gas,disc}/8G\Sigma_{\rm gas,disc}. \quad (24)$$

Thus, the mass of the clumps formed via large-scale gravitational fragmentation should be approximately equal to

$$M_{\rm clump} \approx M_{\rm Jeans} \equiv M_{\rm Jeans}(R) = \Sigma_{\rm gas,disc}\lambda^2_{\rm Jeans} = \left(\frac{\pi}{8G}\right)^2 \frac{\sigma^4_{\rm gas,disc}}{\Sigma_{\rm gas,disc}} \quad (25)$$

(Kim & Ostriker 2001). We can then obtain the collision time-scale that depends on the Jeans mass:

$$t_{\rm coll,clump} \approx \frac{A^{1/3}M^{1/3}_{\rm Jeans}}{2^{1/3}G^{2/3}\Sigma_{\rm gas,disc}} = \frac{\pi^2 A^{1/3} Q^{4/3}}{2^{7/3}\kappa^{4/3}} \approx \frac{\pi^2}{2^{10/3}}\left(\frac{1}{2A}\right) Q^{4/3} \approx t_{\rm shear}\, Q^{4/3}, \quad (26)$$

where for the last line we have assumed a flat circular velocity curve (i.e. $\kappa = 2\sqrt{2}A$). Equation (26) implies that the time-scale ratio $t_{\rm coll,\,clump}/t_{\rm shear}$ is directly related to the Toomre parameter Q. If $Q \gg 1$, $t_{\rm coll,\,clump} \gg t_{\rm shear}$ and clump–clump collisions will not be relevant in the disc. Only when $Q \leq 1$ does $t_{\rm coll,\,clump} \leq t_{\rm shear}$ and clump–clump collisions become important.

It thus seems that gravitational instabilities are the ultimate sources of the turbulent energy. As a sanity check, we now compare the energy injection rate from gravitational instabilities $\dot{\epsilon}_{\rm inject,GI}$ to that from clump–clump collisions $\dot{\epsilon}_{\rm inject,coll}$ (equation 13). The energy injection rate (per volume) from gravitational instabilities is of the order of

$$\dot{e}_{\rm inject,GI} \approx G(\Sigma_{\rm gas,disc}/h_{\rm gas,disc})^2 L_{\rm D}^2\,\Omega \approx G\Sigma^2_{\rm gas,disc}\Omega \quad (27)$$

(see equation 46 of Mac Low & Klessen 2004), where we have used $h_{\rm gas,\,disc} \approx L_{\rm D}$ as the scale height of the gas disc should be approximately equal to the turbulence driving scale for gravitationally unstable gas discs (Blitz & Rosolowsky 2006; Swinbank et al. 2011; Hughes et al. 2013; Kim & Ostriker 2015), and as is indeed the case for the molecular ring of NGC 404 (see the right-hand panel of Fig. 10). Thus, the energy injection rate (per unit mass) from gravitational instabilities $\dot{\epsilon}_{\rm inject,GI}$ is

$$\dot{\epsilon}_{\rm inject,GI} = \dot{e}_{\rm inject,GI}/\rho_{\rm gas,disc} \approx G\Sigma^2_{\rm gas,disc}\Omega/(\Sigma_{\rm gas,disc}/2h_{\rm gas,disc}) \approx 2G\Sigma_{\rm gas,disc}\,\Omega\,h_{\rm gas,disc}, \quad (28)$$

where we have used $\rho_{\rm gas,\,disc} = \Sigma_{\rm gas,\,disc}/2h_{\rm gas,\,disc}$. Panel (c) in Fig. 9 shows the derived energy injection rate (per unit mass) from gravitational instabilities $\dot{\epsilon}_{\rm inject,GI}$ as a function of the galactocentric radius $R_{\rm gal}$ in NGC 404. In the molecular ring, these energy injection rates (per unit mass) from gravitational instabilities $\dot{\epsilon}_{\rm inject,GI}$ are indeed within an order of magnitude of those from clump–clump collisions $\dot{\epsilon}_{\rm inject,coll}$ ($\dot{\epsilon}_{\rm inject,GI} \approx 4\,\dot{\epsilon}_{\rm inject,coll}$). This provides further evidence for gravitational instabilities as the onset of clump–clump collisions and turbulence. We also note that $\dot{\epsilon}_{\rm inject,GI}$ should in fact always be $\approx$4 times larger than $\dot{\epsilon}_{\rm inject,coll}$ for a flat rotation curve (i.e. $\Omega = 2A$), as $h_{\rm gas,\,disc} \approx \lambda_{\rm coll} = G\Sigma_{\rm gas,\,disc}/2A^2$ (see equations 20 and 13).

5 IMPLICATIONS OF COLLISION-INDUCED TURBULENCE

In Section 4.4, we characterized the driving scale and energy injection rate of turbulence from clump–clump collisions. The results have profound implications for the dynamics and density structures of molecular gas, as interstellar turbulence is one of the main agents opposing gravity (e.g. Federrath & Klessen 2012; Hennebelle & Falgarone 2012; Padoan et al. 2014) and shaping the molecular ISM (e.g. Kritsuk et al. 2011; Orkisz et al. 2017).

In this section, we will discuss how clump–clump collision-driven turbulence affects the dynamical states (virial parameters $\alpha_{\rm vir,\,c}$) and density structures (mass–size relations) of clumps and clouds. We will tackle the following questions with regard to NGC 404: (1) why are clumps in rough virial equilibria (i.e. $\alpha_{\rm vir,\,clump} \approx 2$) while clouds are strongly self-gravitating (i.e. $\alpha_{\rm vir,\,cloud} < 1$) in the molecular ring (see Section 3.4); (2) why do clumps have a mass–size relation ($D_{\rm m,\,clump} \approx 1.7$) different from that of clouds ($D_{\rm m,\,cloud} \approx 2.1$) in the molecular ring (see Section 3.3); and (3) based on our estimates of the dynamical states and mass–size relation of clumps, can we predict the clump sizes in the molecular ring?

5.1 Stability of multiple-scale molecular structures

Neglecting magnetic fields, the stability and dynamics of molecular gas structures are generally governed by self-gravity and interstellar turbulence. In a differentially rotating gas disc, shear (and tides, i.e. external/galactic gravity) is an additional factor. This leads to a complex interplay between shear and turbulence, both opposing self-gravity. The key question is then in which ranges of size and mass do shear, turbulence, and self-gravity individually dominate the gas dynamics.

In a differentially rotating gas disc, there are two critical lengths. One is the Toomre length

$$\lambda_{\rm Toomre} \equiv \lambda_{\rm Toomre}(R) = 2\pi^2 G\Sigma_{\rm gas,disc}/\kappa^2, \quad (29)$$

where the numerical coefficient $2\pi^2$ applies to infinitely thin gas discs (Tasker & Tan 2009). The other is the Jeans length $\lambda_{\rm Jeans} \approx \pi\sigma^2_{\rm gas,disc}/8G\Sigma_{\rm gas,disc}$ (equation 24). Molecular structures with $L_{\rm acc} \geq \lambda_{\rm Toomre}$ (where $L_{\rm acc}$ is the accumulation length; equation 7) are supported against gravity by shear motions and thus cannot collapse, while molecular structures with $L_{\rm acc} \leq \lambda_{\rm Toomre}$ are supported against gravity by turbulent motions. Only molecular structures with $\lambda_{\rm Jeans} < L_{\rm acc} < \lambda_{\rm Toomre}$ are dominated by gravity, and thus can collapse

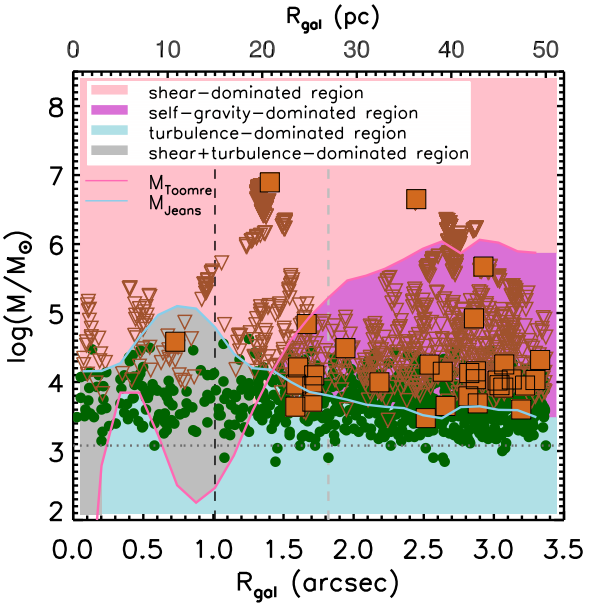

Figure 11. Various masses as a function of galactocentric distance in NGC 404. The Toomre mass ($M_{\rm Toomre}$) is shown as a pink line, the Jeans mass ($M_{\rm Jeans}$) as a blue line, and individual clumps and clouds as data points. Symbols are as for Fig. 4. In the pink-shaded region ($M_{\rm c} > M_{\rm Jeans}$ and $M_{\rm c} > M_{\rm Toomre}$), molecular gas structures are supported against gravity by shear. In the blue-shaded region ($M_{\rm c} \leq M_{\rm Toomre}$ and $M_{\rm c} \leq M_{\rm Jeans}$), molecular gas structures are supported against gravity by turbulence. In the grey-shaded region ($M_{\rm Toomre} < M_{\rm c} \leq M_{\rm Jeans}$), molecular gas structures are supported against gravity by both shear and turbulence. In the magenta-shaded region ($M_{\rm Jeans} < M_{\rm c} \leq M_{\rm Toomre}$), molecular gas structures are gravitational unstable due to dominant self-gravity. The black vertical dashed line indicates the boundary ($R_{\rm gal} = 15$ pc) between the central region and molecular ring, while the grey vertical dashed line indicates the galactocentric distance ($R_{\rm gal} = 27$ pc) beyond which the molecular gas disc is no longer gravitationally stable (i.e. Toomre parameter's $Q \leq 1$ at $R_{\rm gal} \geq 27$ pc; see Section 4.5). The black horizontal dotted line indicates our mass detection limit ($\log(10\delta_{\rm M}/{\rm M}_\odot) = 3.08$; see Section 3.1).

gravitationally. The two critical length-scales also correspond to two critical masses: the Toomre mass

$$M_{\rm Toomre} \equiv M_{\rm Toomre}(R) = \Sigma_{\rm gas,disc}\lambda^2_{\rm Toomre} = \left(\frac{2\pi^2 G}{\kappa^2}\right)^2 \Sigma^3_{\rm gas,disc} \quad (30)$$

and the Jeans mass $M_{\rm Jeans} \equiv \Sigma_{\rm gas,disc}\lambda^2_{\rm Jeans} = \left(\frac{\pi}{8G}\right)^2 \frac{\sigma^4_{\rm gas,disc}}{\Sigma_{\rm gas,disc}}$ (equation 25).

Fig. 11 shows the Toomre and Jeans masses as a function of the galactocentric radius R (i.e. $R_{\rm gal}$), as well as the masses of all clumps and clouds at their respective galactocentric radii. There are four regions in Fig. 11: (1) $M_{\rm c} > M_{\rm Jeans}$ and $M_{\rm c} > M_{\rm Toomre}$ (pink-shaded region), where molecular structures are supported against gravity or even disrupted by shear (i.e. $\alpha_{\rm vir,\,c} > \alpha_{\rm vir,\,crit}$); (2) $M_{\rm c} \leq M_{\rm Toomre}$ and $M_{\rm c} \leq M_{\rm Jeans}$ (blue-shaded region), where molecular structures are supported against gravity by turbulence (i.e. $\alpha_{\rm vir,\,c} \geq \alpha_{\rm vir,\,crit}$); (3) $M_{\rm Toomre} < M_{\rm c} \leq M_{\rm Jeans}$ (grey-shaded region), where molecular structures are supported against gravity or even disrupted by both shear and turbulence (i.e. $\alpha_{\rm vir,\,c} \geq \alpha_{\rm vir,\,crit}$); and (4) $M_{\rm Jeans} < M_{\rm c} \leq M_{\rm Toomre}$ (magenta-shaded region), where molecular structures are gravitationally unstable due to dominant self-gravity (i.e. $\alpha_{\rm vir,\,c} < \alpha_{\rm vir,\,crit}$). We note that $M_{\rm Jeans} > M_{\rm Toomre}$ (or equivalently $\lambda_{\rm Jeans} > \lambda_{\rm Toomre}$) in the central region, while $M_{\rm Jeans} < M_{\rm Toomre}$ (or equivalently $\lambda_{\rm Jeans} < \lambda_{\rm Toomre}$) at $R_{\rm gal} \gtrsim 20$ pc in the molecular ring (see also the right-hand panel of Fig. 10). This is consistent with our earlier conclusion that the central region is gravitationally stable, while the molecular ring is gravitationally unstable or only marginally stable (Section 4.5).

5.1.1 *Gas dynamics in the molecular ring*

We first assess the dynamical states of the molecular structures in the molecular ring of NGC 404, where our collision model holds. We find that the clumps in the molecular ring have their Jeans masses $M_{\rm Jeans}$ (or Jeans lengths $\lambda_{\rm Jeans}$) approximately equal to the collision critical masses $M_{\rm c,\,coll}$ (or the collision critical lengths $\lambda_{\rm coll}$), i.e. $M_{\rm Jeans} \approx M_{\rm c,\,coll}$ (or $\lambda_{\rm Jeans} \approx \lambda_{\rm coll}$), as shown in Fig. 11 (or the right-hand panel of Fig. 10). In fact, for a gravitationally unstable disc where the disc velocity dispersion $\sigma_{\rm gas,\,disc}$ is set by the maximum velocity dispersion sustained by clump–clump collisions $\sigma_{\rm max,\,coll} = G\Sigma_{\rm gas,\,disc}/A$ (see equation 19 and Section 4.4.3), one naturally expects

$$\begin{aligned}\lambda_{\rm Jeans} &= \pi\sigma^2_{\rm gas,disc}/8G\Sigma_{\rm gas,disc} \approx (\pi/8G\Sigma_{\rm gas,disc})(G\Sigma_{\rm gas,disc}/A)^2 \\ &= (\pi/4)\lambda_{\rm coll} \approx \lambda_{\rm coll}, \end{aligned} \quad (31)$$

and thus $M_{\rm Jeans} \approx M_{\rm c,\,coll}$. Our findings that $\lambda_{\rm Jeans} \approx \lambda_{\rm coll}$ and $h_{\rm gas,\,disc} \approx \lambda_{\rm coll}$ (see equation 20) are consistent with calculations and simulations showing that the average separation of clumps and the disc thickness are primarily regulated by gravitational instabilities and are about the Jeans length (e.g. Elmegreen, Kim & Staveley-Smith 2001; Dutta et al. 2009; Bournaud et al. 2010).

Clumps are supported by turbulence. The fact that $\lambda_{\rm Jeans} \approx \lambda_{\rm coll}$ (or $M_{\rm Jeans} \approx M_{\rm c,\,coll}$) has important implications for the dynamical states of clumps and clouds in our collision model. First, clumps should have their masses $M_{\rm clump} \approx M_{\rm c,\,coll} \approx M_{\rm Jeans}$ (see Fig. 11), and thus should be supported against gravity by collision-induced turbulence (i.e. $\alpha_{\rm vir,\,clump} \approx \alpha_{\rm vir,\,crit}$). Indeed, clumps are in rough virial equilibrium (mean virial parameter $\langle\alpha_{\rm\,vir,\,clump}\rangle = 1.82 \pm 0.07$; see Section 3.4) in the molecular ring. This is consistent with numerical simulations that show the kinetic energy injected by clump–clump collisions is enough to counterbalance the self-gravity of clumps in rough virial equilibrium (e.g. Tasker & Tan 2009; Li et al. 2018; Wu et al. 2018).

We note that turbulent energy injected by clump–clump collisions is only sufficient to support clumps against self-gravity, but is not enough to drive them out of virial equilibrium (i.e. disrupt them), i.e. clumps should always remain in rough virial equilibrium with $\alpha_{\rm vir,\,clump} \approx \alpha_{\rm vir,\,crit}$. This is because clump–clump collisions can only happen effectively between gravitationally bound objects (e.g. Tan 2000; Gammie 2001; Tasker & Tan 2009; Goldbaum et al. 2016; Takahira et al. 2018). If the turbulent velocity dispersion is abnormally high temporarily, such that clumps become unbound ($\alpha_{\rm vir,\,clump} > \alpha_{\rm vir,\,crit}$), the collisions between clumps become less frequent (as the number of bound clumps decreases), driving $\alpha_{\rm vir,\,clump}$ downward again. Thus, clumps will be self-regulated by their collisions to have $\alpha_{\rm vir,\,c} \approx \alpha_{\rm vir,\,crit}$.

Clouds are dominated by self-gravity. On the other hand, clouds (which by definition contain more than one clump) should have their masses $M_{\rm cloud} > M_{\rm c,\,coll} \approx M_{\rm Jeans}$ (see Fig. 11), and thus should be dominated by self-gravity (i.e. $\alpha_{\rm vir,\,cloud} < \alpha_{\rm vir,\,crit}$), i.e. collision-induced turbulence cannot support clouds against gravity in virial equilibrium. Indeed, clouds have a mean virial parameter much smaller than unity ($\langle\alpha_{\rm\,vir,\,cloud}\rangle = 0.41 \pm 0.02$; see Section 3.4) in the molecular ring.

Most massive clouds are dominated by shear. The most massive clouds, however, may not be gravitationally bound as their dynamics are likely dominated by shear rather than turbulence and self-gravity. As one can see from Fig. 11, in the molecular ring of NGC 404, the two most massive trunks (labelled by the two largest contours in Fig. 2) and some of their largest branches (with $M_{\rm cloud} \gtrsim 10^6$ M$_\odot$) have masses larger than the Toomre masses (pink line in Fig. 11), suggesting that these structures may not be gravitationally bound.

In fact, Liu et al. (2021) introduced a maximum size (diameter) for a cloud to stay gravitationally bound in the presence of shear motions,

$$\lambda_{\rm shear} \equiv 2R_{\rm shear} \approx \frac{3\pi G \Sigma_{\rm gas,disc}}{2A^2} \tag{32}$$

(see equation 54 in Liu et al. 2021), assuming that the cloud has a spherical homogeneous density distribution. An effective virial parameter $\alpha_{\rm eff,\,vir}$, which provides a straightforward measurable diagnostic of cloud boundedness in the presence of a non-negligeable external potential, was also defined in Liu et al. (2021) (see their equation 34). A molecular structure with a size (diameter) larger than $\lambda_{\rm shear}$ should have $\alpha_{\rm eff,\,vir} > \alpha_{\rm vir,\,crit}$ (Liu et al. 2021).

Our estimated maximum cloud size $\lambda_{\rm shear}$ is in good agreement with the Toomre length $\lambda_{\rm Toomre}$ (equation 29) in the molecular ring, with the ratio of $\lambda_{\rm Toomre}$ and $\lambda_{\rm shear}$ between 0.5 and 1.5 (see the right-hand panel of Fig. 10). This is expected, since the Toomre length also sets a natural spatial scale over which molecular gas structures cannot be bound by gravity due to shear. The fact that $\lambda_{\rm Toomre} \approx \lambda_{\rm shear}$ implies $\alpha_{\rm eff,\,vir} > \alpha_{\rm vir,\,crit}$ for structures with $M_{\rm cloud} > M_{\rm Toomre}$. Indeed, we find structures with $M_{\rm cloud} > M_{\rm Toomre}$ to have estimated effective virial parameters $\alpha_{\rm eff,\,vir}$ ranging from 2 to 5 in the molecular ring. As such, these massive clouds are not gravitationally bound. They are likely to be disrupted or even torn apart by galactic shear.

5.1.2 *Gas dynamics in the central region*

The central region ($R_{\rm gal} \leq 15$ pc) of NGC 404 is found to be gravitationally stable, with $Q = 3$–30 (see Fig. 10). Our collision model is therefore not expected to hold there (see Section 4.5), and indeed $M_{\rm Jeans}$ is significantly larger than $M_{\rm Toomre}$ throughout that region (see Fig. 11). This implies that molecular structures in the central region should not collapse gravitationally. As sources of turbulence other than clump–clump collisions are likely present in the central region (see Sections 4.4 and 4.5), not only clumps but even clouds there appear to be supported against gravity by turbulent motions ($\langle\alpha_{\rm vir,\,clump}\rangle = 1.52 \pm 0.11$ and $\langle\alpha_{\rm vir,\,cloud}\rangle = 1.14 \pm 0.12$ in the central region).

A few of the most massive molecular structures in the very centre ($R_{\rm gal} \lesssim 10$ pc) region have masses $M_{\rm cloud}$ much larger than $M_{\rm Toomre}$, suggesting shear motions may dominate their dynamics and tear them apart (i.e. $\alpha_{\rm eff,\,vir} > \alpha_{\rm vir,\,crit}$).

5.2 Implications for the mass–size relation

As shown in Section 5.1, clumps are primarily dominated by turbulence and clouds by self-gravity (except for the most massive clouds that are dominated by shear) in the molecular ring. As the two main drivers of density structures in molecular gas (thus the mass–size relation) are turbulence and self-gravity (Field, Blackman & Keto 2008, 2011; Kritsuk & Norman 2011; Gouliermis 2018), could it be that the different mass–size relations for the clumps and clouds in the molecular ring ($D_{\rm m,\,clump} = 1.63 \pm 0.04$ versus $D_{\rm m,\,cloud} = 2.06 \pm 0.01$; see Section 3.3) also originate from these two different physical mechanisms (respectively, turbulence and self-gravity)? To answer this question, we predict the mass–size trend for both the turbulence-dominated and the self-gravity-dominated regime below, and compare our predictions with observations.

5.2.1 *Mass–size relation regulated by turbulence*

We first assess the mass–size relation regulated by collision-induced turbulence, i.e. the mass–size relation of clumps in the molecular ring. In our clump–clump collision scenario, the turbulent energy injected by the collisions cascades down to small scales and counterbalances self-gravity to produce a rough virial equilibrium (i.e. the clumps are able to maintain virialization; see Section 5.1). These virialized clumps should always have their energy dissipation rates (per unit mass) $\dot{\epsilon}_{\rm diss,clump} = \frac{1}{4}\frac{\sigma^3_{\rm obs,los}}{R_{\rm clump}}$ (equation 14) match their virial energy dissipation rates (per unit mass)

$$\dot{\epsilon}_{\rm diss,vir} = \frac{1}{4}\left(\alpha_{\rm vir,crit}\, G M_{\rm clump}/5\right)^{3/2} R_{\rm clump}^{-5/2} \tag{33}$$

(Li 2017b), i.e. $\dot{\epsilon}_{\rm diss,clump} \approx \dot{\epsilon}_{\rm diss,vir}$, where as before $\alpha_{\rm vir,\,crit} \approx 2$ is the boundary between gravitationally bound and unbound objects (Kauffmann et al. 2013, 2017). The virial energy dissipation rate (per unit mass) $\dot{\epsilon}_{\rm diss,vir}$ is the energy dissipation rate (per unit mass) a molecular gas structure would have if it were virialized. We therefore expect

$$\dot{\epsilon}_{\rm diss,vir} \approx \dot{\epsilon}_{\rm diss,clump} \approx \dot{\epsilon}_{\rm inject,coll} \tag{34}$$

for the clumps in the molecular ring of NGC 404, where we have used $\dot{\epsilon}_{\rm diss,clump} \approx \dot{\epsilon}_{\rm inject,coll}$, i.e. the energy dissipation rates (per unit mass) of clumps are approximately equal to the energy dissipation rates (per unit mass) from clump–clump collisions in the molecular ring (see Section 4.4). We indeed find very good agreements between the estimated $\dot{\epsilon}_{\rm diss,vir}$, the measured $\dot{\epsilon}_{\rm diss,clump}$, and our predicted $\dot{\epsilon}_{\rm inject,coll}$ in the molecular ring (see panel c of Fig. 9), providing more evidence that the turbulence induced by clump–clump collisions can support and maintain molecular ring clumps in virial equilibrium.

The facts that $\dot{\epsilon}_{\rm diss,vir} = \frac{1}{4}\left(\alpha_{\rm vir,crit}\, G M_{\rm clump}/5\right)^{3/2} R_{\rm clump}^{-5/2} \approx \dot{\epsilon}_{\rm inject,coll}$, and that $\dot{\epsilon}_{\rm inject,coll}$ is independent of clump properties (it depends only on $\Sigma_{\rm gas,\,disc}$ and A; see equation 13), imply $M_{\rm clump}^{3/2} R_{\rm clump}^{-5/2}$ is constant at any given location in the disc (i.e. for any given $\Sigma_{\rm gas,\,disc}$ and A). Thus, the mass–size relation should have the form $M_{\rm clump} \propto R_{\rm clump}^{5/3}$, as suggested by Li (2017a). Specifically, by equating the virial energy dissipation rate $\dot{\epsilon}_{\rm diss,vir}$ (equation 33) to the energy injection rate due to clump–clump collisions $\dot{\epsilon}_{\rm inject,coll}$ (equation 13), we obtain

$$\begin{aligned} M_{\rm clump} &= \left(5/\alpha_{\rm vir,crit} G\right)\left(4\dot{\epsilon}_{\rm inject,coll}\right)^{2/3} R_{\rm clump}^{5/3} \\ &= \left(5/\alpha_{\rm vir,crit} G\right)\left(2G^2\Sigma^2_{\rm gas,disc}/A\right)^{2/3} R_{\rm clump}^{5/3} \end{aligned} \tag{35}$$

for virialized clumps supported by collision-induced turbulence. The mass–size relation of clumps should thus depend only on the galactic properties (i.e. $\Sigma_{\rm gas,\,disc}$ and A). The red dashed line in the middle panel of Fig. 5 shows our predicted mass–size relation using equation (35), which is in very good agreement (both slope *and* normalization) with the observed trend of the clumps in the molecular ring (green dashed line), $M_{\rm clump} \propto R_{\rm clump}^{1.63\pm0.04}$. In equation (35), we have therefore predicted an accurate mass–size relation regulated by collision-induced turbulence only, with no free parameter. We also note that the molecular structures lying above the predicted mass–size relation in Fig. 5 should have $\alpha_{\rm vir,\,c} < \alpha_{\rm vir,\,crit}$, while those lying below the relation should have $\alpha_{\rm vir,\,c} > \alpha_{\rm vir,\,crit}$.

Equation (35) also predicts the sizes of clumps, i.e. the clump size $R_{\rm c,\,coll}$ corresponding to the clump mass $M_{\rm c,\,coll}$:

$$\begin{aligned} R_{\rm clump} &= \left(4\,\dot{\epsilon}_{\rm inject,coll}\right)^{-2/5}\left(\alpha_{\rm vir,crit}\,GM_{\rm clump}/5\right)^{3/5} \\ &= \left(4\,\dot{\epsilon}_{\rm inject,coll}\right)^{-2/5}\left(\alpha_{\rm vir,crit}\,GM_{\rm c,coll}/5\right)^{3/5} \\ &= \frac{1}{5^{3/5}}\,\frac{G\Sigma_{\rm gas,disc}}{2A^2} \approx 0.19\,G\Sigma_{\rm gas,disc}/A^2 \\ &= 0.38\,\lambda_{\rm coll} \equiv R_{\rm c,coll}, \end{aligned} \tag{36}$$

where we have used $\dot{\epsilon}_{\rm inject,coll} = G^2\Sigma^2_{\rm gas,disc}/2A$ (equation 13), $M_{\rm c,coll} = G^2\Sigma^3_{\rm gas,disc}/4A^4$ (equation 10), and $\alpha_{\rm vir,\,crit} = 2$. It therefore seems that the typical clump size regulated by clump–clump collisions $R_{\rm c,\,coll}$ is determined solely by galactic properties ($\Sigma_{\rm gas,\,disc}$ and A). A comparison between the observed most common clump size, which also happens to be the median clump size $R_{\rm clump}$, and our predicted $R_{\rm c,\,coll}$ at each galactocentric radius is shown in panel (d) of Fig. 9. Again, a very good agreement is found in the molecular ring of NGC 404. Our results thus support numerical simulations suggesting that clump–clump collisions can be an important mechanism to determine both the masses and the sizes of clumps (e.g. Tasker & Tan 2009; Li et al. 2018). In the central region, clumps have sizes much larger than our predictions, implying that in that region other physical mechanisms are required to explain their formation. Clumps in the central region nevertheless have sizes similar to those of clumps in the molecular ring, a feature we will discuss in Section 6.3.

It is also worth mentioning here that, for a flat rotation curve ($\Omega = 2A$), we have $\lambda_{\rm coll} = G\Sigma_{\rm gas,\,disc}/2A^2 = \sigma_{\rm max,\,coll}/\Omega \approx \sigma_{\rm gas,\,disc}/\Omega$ (see equations 8 and 18, Section 4.5, and the middle panel of Fig. 10) and therefore

$$\begin{aligned} R_{\rm clump}/R_{\rm gal} &= R_{\rm c,coll}/R_{\rm gal} \approx 0.38\,\lambda_{\rm coll}/R_{\rm gal} \\ &= 0.38\,\lambda_{\rm coll}\,\Omega/V_{\rm circ} \approx 0.38\,\sigma_{\rm gas,disc}/V_{\rm circ} \end{aligned} \tag{37}$$

(see equation 36), where as usual $R_{\rm gal}$ is the galactocentric distance of the clump. This relation is a perfect match to the best-fitting relation of the clumps in a sample of local analogues to high-redshift galaxies in DYnamics of Newly-Assembled Massive Objects (DYNAMO)-*HST* survey (Fisher et al. 2017): $R_{\rm clump}/R = (0.38 \pm 0.02)\,\sigma_{\rm gas,disc}/V_{\rm circ}$. Fisher et al. (2017) explained their observed relation by instabilities in a self-gravitating disc, but only predicted a range of $(R_{\rm clump}/R)/(\sigma_{\rm obs,\,los}/V_{\rm circ})$ ratios of 1/3 to $\sqrt{2}/3 \approx 0.47$ (see their equation 3). A precise match between our model (0.38) and DYNAMO-*HST* observations (0.38 ± 0.02) does not only suggest that the molecular ring of NGC 404 is akin to high-z star-forming disc galaxies, but also that clump–clump collisions are an important mechanism to regulate clump sizes across redshifts.

5.2.2 *Mass–size relation regulated by self-gravity*

We now analyse the mass–size relation regulated by self-gravity, i.e. the mass–size relation of clouds (rather than clumps) in the molecular ring of NGC 404. As clouds are gravitationally unstable and have $\alpha_{\rm vir,\,cloud} \ll \alpha_{\rm vir,\,crit}$, they should lie above the mass–size relation regulated by turbulence in the middle panel of Fig. 5 (equation 35; i.e. the red dashed line). Indeed, the clouds in the molecular ring are located above both the predicted (red dashed line) and measured (green dashed line) mass–size relations of clumps there.

In the molecular ring, the mass–size relation of clouds also exhibits a steeper power law ($M_{\rm cloud} \propto R^{2.06\pm0.01}_{\rm cloud}$, brown dashed line) than that of clumps ($M_{\rm clump} \propto R^{1.63\pm0.04}_{\rm clump}$, green dashed line; see Section 3.3). This again appears to be consistent with theoretical results suggesting that structures subject to gravitational collapse should have fractal dimensions $D_{\rm m}$ larger than the critical value $D_{\rm m,\,crit} = 2$ for gravitational instabilities (Perdang 1990; Kritsuk & Norman 2011).

5.2.3 *Clumps versus clouds*

In summary, turbulence triggered by clump–clump collisions has important implications for the structure and dynamics of molecular gas. In a gravitationally unstable or only marginally stable gas disc where clump–clump collisions are efficient, such as the molecular ring of NGC 404, the transition from the turbulence- to the self-gravity-dominated regime seems to occur at a mass $M_{\rm c,coll} = \Sigma_{\rm gas,disc}\lambda^2_{\rm coll} \approx M_{\rm Jeans}$. Molecular structures with masses $\approx M_{\rm c,\,coll}$ (or $\approx M_{\rm Jeans}$), which are typically clumps, have their internal structures and dynamics dominated by collision-induced turbulence (see Section 5.2.1), which is not only able to support them against gravity in a rough virial equilibrium, but also shapes them to yield a mass–size relation with a power-law index $D_{\rm m}$ smaller than 2: $M_{\rm clump} \propto R^{5/3}_{\rm clump}$. Molecular structures with masses much larger than $M_{\rm c,\,coll}$ (or $M_{\rm Jeans}$), which are primarily clouds, have their internal structures and dynamics increasingly governed by self-gravity and thus appear gravitationally unstable, as the turbulent kinetic energy injected by clump–clump collisions is unable to support them against gravitational collapse. The dominant self-gravity breaks the self-similarity of gas structures established by collision-induced turbulence, leading to a mass–size relation with a steeper slope ($D_{\rm m} \gtrsim 2$).

6 DISCUSSION

6.1 Clump mass function due to clump–clump collisions

If clumps are formed via collisions and mergers of (smaller) clumps (i.e. clump–clump collisions), the clumps' lifetimes $t_{\rm life,\,clump}$ should be approximately equal to their collision time-scales $t_{\rm coll,\,clump}$, as the clumps are destroyed by becoming part of larger clumps (Tasker & Tan 2009). If we make the zeroth-order approximation that the number density of clumps is proportional to their lifetimes (i.e. their collision times), we obtain

$$\mathrm{d}N_{\rm clump}(M_{\rm clump})/\mathrm{d}M_{\rm clump} \propto t_{\rm life,clump} \approx t_{\rm coll,clump} \propto M^{1/3}_{\rm clump} \tag{38}$$

(see equation 6), where as before $N_{\rm clump}(M_{\rm clump})$ is the number of clumps with masses $\geq M_{\rm clump}$ (see equation 1). Thus, for those clumps regulated by collisions (i.e. those clumps with $M_{\rm clump} \leq M_{\rm c,\,coll}$), the power-law index of the differential mass distribution function should be $\gamma_{\rm coll,\,clump} \approx 1/3$.

Having said that, clumps with $M_{\rm clump} > M_{\rm c,\,coll}$, cannot form efficiently via clump–clump collisions, as they are disrupted by shear before they can collide and merge with other clumps (see Section 4.2). The number density of clumps with $M_{\rm clump} > M_{\rm c,\,coll}$ should thus decrease sharply with mass, and the differential mass distribution function in the high-mass regime ($M_{\rm clump} > M_{\rm c,\,coll}$) should have $\gamma_{\rm coll,\,clump} < -2$. This is also true of the overall mass distribution function, which is primarily sensitive to the mass distribution at high masses. The result is consistent with the hydrodynamic simulation by Li et al. (2018), who found the cloud population regulated by cloud–cloud collisions to have a cumulative mass distribution function with a power-law index $\gamma \approx -2.4$. Hence, our collision model predicts the differential mass distribution function of clumps to exhibit *two* separate power laws: $\gamma_{\rm coll,\,clump} \approx 1/3$ in the low-mass regime ($M_{\rm clump} \leq M_{\rm c,\,coll}$) and $\gamma_{\rm coll,\,clump} < -2$ in the high-mass regime ($M_{\rm clump}$

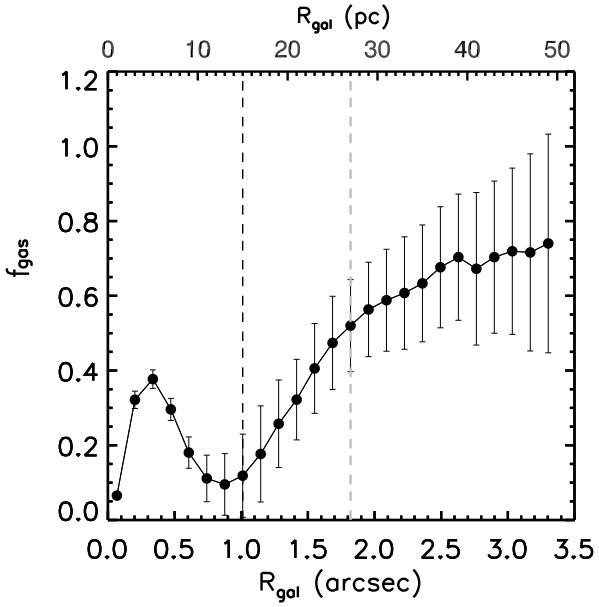

Figure 12. Galactocentric distance dependence of the gas fraction $f_{\rm gas}$ of NGC 404. The black vertical dashed line indicates the boundary ($R_{\rm gal} = 15$ pc) between the central region and molecular ring, while the grey vertical dashed line indicates the galactocentric distance ($R_{\rm gal} = 27$ pc) beyond which the molecular gas disc is no longer gravitationally stable (i.e. Toomre parameter's $Q \leq 1$ at $R_{\rm gal} \geq 27$ pc; see Section 4.5). The error bars indicate the 1σ scatter of the different fractions within each radial bin (not the uncertainty on the mean within each bin, that is much smaller).

$> M_{\rm c,\,coll}$). The observed clump mass distribution function in the molecular ring of NGC 404 indeed closely follows this prediction (see Table 2 and Section 3.1), further suggesting that the clump population in the molecular ring is indeed primarily regulated by clump–clump collisions.

6.2 Effect of stellar feedback on turbulence

As argued in Sections 4.4 and 4.5, clump–clump collisions are likely to be an important mechanism driving the turbulence in (the molecular ring of) NGC 404. Another important source of turbulence in galaxies is stellar feedback, including supernova explosions, stellar winds, ionizing radiation, and protostellar outflows (e.g. Mac Low & Klessen 2004; Dib, Bell & Burkert 2006; Agertz et al. 2009; Krumholz & Burkhart 2016). The question then arises: can stellar feedback also play an important role to drive the turbulence in NGC 404, which is a dwarf galaxy?

One way to assess whether stellar feedback is important to drive turbulence is to analyse whether clump–clump collisions alone are sufficient to maintain the observed velocity dispersions. High-resolution 3D numerical simulations of ISM turbulence suggest that clump–clump collisions serve as a baseline level for turbulence in galaxies, and any excess random motions observed must be caused by additional sources such as stellar feedback, active galactic nucleus (AGN) feedback and/or the magneto-rotational instability (e.g. Agertz et al. 2009; Goldbaum et al. 2016). If this is right, then stellar feedback should not be necessary in the molecular ring of NGC 404, as clump–clump collisions are sufficient to maintain the observed velocity dispersions (see panel c of Fig. 9 and Section 4.4). In the central region, however, the observed velocity dispersions are much larger than our collision model predictions (see equation 18 and Fig. 4), and additional energy sources are required to disturb the gas there. Stellar feedback is one such potential energy source.

To explore the origin of disc turbulence using observational tests, Krumholz & Burkhart (2016) constructed two simple analytical models describing collision-driven turbulence and feedback-driven turbulence, respectively. The models predict SFR $\propto \sigma^2_{\rm obs,los}$ for feedback-driven turbulence and SFR $\propto \sigma_{\rm obs,los}\, f^2_{\rm gas}$ for collision-driven turbulence (i.e. turbulence triggered by gravitational instabilities), where $f_{\rm gas} \equiv \frac{\Sigma_{\rm gas,disc}}{\Sigma_{\rm gas,disc}+\Sigma_{*,\rm disc}}$ is the galaxy gas fraction and $\Sigma_{*,\,\rm disc}$ is the (coarse-grained) stellar mass surface density of the galactic disc. Fig. 12 presents the galactocentric distance dependence of the gas fraction $f_{\rm gas}$ of NGC 404, assuming only the molecular gas observed here for the gas. The stellar mass surface density is taken from the stellar mass model presented in Nguyen (2017) and Davis et al. (2020). One can see that the gas fraction $f_{\rm gas}$ is very high across the molecular ring, with a median of $\approx$0.5, similar to those found in high-redshift star-forming gas discs (e.g. Swinbank et al. 2015; Kanekar et al. 2020; Tacconi et al. 2020).

To properly test the predictions of these two models in NGC 404, spatially resolved SFR measurements are required. High-resolution ($\approx$0.28 arcsec) and high-sensitivity ($\mu_{\rm 33GHz} \approx 3.1$ μJy beam^{-1}) observations of the 33 GHz radio continuum emission (tracing free–free emission from H II regions) have been carried out in NGC 404 with Very Large Array (VLA; Liu et al. in preparation). However, except for a very bright central point source possibly associated with the AGN, no extended emission is detected, suggesting an upper limit to the SFR surface density of

$$\left(\frac{\Sigma_{\rm SFR}}{\rm M_\odot\ yr^{-1}\ pc^{-2}}\right) < 4.6\times10^{-28}\left(\frac{T_{\rm e}}{10^4\ \rm K}\right)\left(\frac{\nu}{\rm GHz}\right)^{0.1} \times\left(\frac{L_{\nu,\rm beam}}{\rm erg\ s^{-1}\ Hz^{-1}}\right)\left(\frac{\rm beam}{\rm pc^2}\right)^{-1}$$
$$\left(\frac{L_{\nu,\rm beam}}{\rm erg\ s^{-1}\ Hz^{-1}}\right) = 4\pi\left(\frac{D}{\rm pc}\right)^2\times10^{-23}\times(3.0857\times10^{18})^2 \times\left(\frac{\mu_{\rm 33GHz}}{\rm Jy\ beam^{-1}}\right) \quad (39)$$

(see equation 11 in Murphy et al. 2011), where $T_{\rm e} \approx 11\,000$ K is the electron temperature, $\nu = 33$ GHz the frequency, $L_{\nu,\,\rm beam}$ the free–free spectral luminosity per beam, $D = 3.06 \times 10^6$ pc the distance of NGC 404, $\mu_{\rm 33GHz} \approx 3.1$ μJy beam^{-1} the sensitivity of our VLA observations, and beam ≈ 20 pc^2 the VLA synthesized beam size. Thus, we derive a maximum SFR surface density of $\Sigma_{\rm SFR} \approx 1\times10^{-6}$ M$_\odot$ yr^{-1} pc^{-2} for NGC 404, or an upper limit to the SFR volume density of $\rho_{\rm SFR} \equiv \Sigma_{\rm SFR}/2h_{\rm gas,\,disc} \approx 1.6\times10^{-7}$ M$_\odot$ yr^{-1} pc^{-3} (using $h_{\rm gas,\,disc} \approx 3$ pc; see panel d in Fig. 9).

The energy injection rate (per volume) from supernova (SN) explosions is given by

$$\dot{e}_{\rm SN} = \xi_{\rm SN} E_{\rm SN}(f_{\rm SN}\rho_{\rm SFR}) \quad (40)$$

(see equation 4 of Kawakatu, Wada & Ichikawa 2020 and equation 55 of Mac Low & Klessen 2004), where $\xi_{\rm SN} = 0.1$ is the efficiency with which SN energy is transferred to the gas (e.g. Thornton et al. 1998), $E_{\rm SN} = 10^{51}$ erg (or 5×10^7 M$_\odot$ km^2 s^{-2}) is the total energy injected by one SN, and $f_{\rm SN} = 10^{-2}$ M$_\odot^{-1}$ is the fraction of supernovae per solar mass of star formation (e.g. Thompson, Quataert & Murray 2005). The energy injection rate (per unit mass) from supernova explosions is therefore

$$\dot{\epsilon}_{\rm SN} = \dot{e}_{\rm SN}/\rho_{\rm gas} = \xi_{\rm SN}E_{\rm SN}(f_{\rm SN}\rho_{\rm SFR})/\rho_{\rm gas} \leq 2.5\ \rm km^2\ s^{-2}\ Myr^{-1}, \quad (41)$$

where we have used the $\rho_{\rm SFR}$ upper limit above and the global gas volume density of $\rho_{\rm gas} = \Sigma_{\rm gas,\,disc}/2h_{\rm gas,\,disc} \approx 10^{3.5}\,{\rm M_\odot\,pc^{-3}}$ as measured in NGC 404 (see Fig. B2 and panel d in Fig. 9 for the distributions of $\Sigma_{\rm gas,\,dis}$ and $h_{\rm gas,\,disc}$, respectively). This upper limit to the energy injection rate (per unit mass) from stellar feedback is clearly smaller than the observed energy dissipation rate (per unit mass) of clumps and the energy injection rate (per unit mass) from clump–clump collisions, i.e. $\dot{\epsilon}_{\rm SN} < \dot{\epsilon}_{\rm diss,clump} \approx \dot{\epsilon}_{\rm inject,coll} \approx 10\,{\rm km^2\,s^{-2}\,Myr^{-1}}$ (see panel c in Fig. 9). It therefore seems that feedback-driven turbulence is much less important than collision-driven turbulence in NGC 404.

6.3 Clump migration towards the galaxy centre

Panels (b) and (d) of Fig. 9 show the clumps of NGC 404 have relatively uniform properties (i.e. masses and sizes) as a function of galactocentric distance, with the median clump masses and sizes varying by at most a factor of ≈4 and ≈2, respectively. In fact, the clumps of NGC 404 also seem to have similar velocity dispersions (or similar energy dissipation rates; see panel c in Fig. 9) at different galactocentric distances. These surprisingly small variations are unlikely to be due to the dendrogram decomposition algorithm, as the dendrogram approach should allow to identify clumps with sizes varying by an order of magnitude (e.g. Colombo et al. 2014; Henshaw et al. 2016, 2019; Wong et al. 2019; Krieger et al. 2020).

It is easy to understand why the clump masses and sizes do not vary much across the molecular ring. Indeed, we have demonstrated that these clump properties depend only on the galactic properties in the molecular ring, specifically $\Sigma_{\rm gas,\,disc}$ and A (see equations 10 and 36, respectively). As neither varies significantly across the molecular ring (see Figs B2 and B1, respectively), the clump masses and sizes are not expected to exhibit much variation across this region either (see the red data points in panels b and panel d of Fig. 9).

The question then is why do the clumps in the central region, where galactic properties are significantly different, also share the same properties as those in the molecular ring? One obvious possibility is that the clumps currently in the central region migrated inward from larger galactocentric distances (i.e. from the molecular ring). We have shown in Section 4.4 that clump–clump collisions can extract kinetic energy from ordered differential rotation and inject this energy into turbulence. Clumps must therefore loose angular momentum and migrate towards the galaxy centre (Gammie 2001; Vollmer & Beckert 2002; Dekel et al. 2009b; Namekata & Habe 2011). This scenario of clump migration towards galactic centres is discussed at length in many theoretical works (Gammie 2001; Elmegreen et al. 2007; Elmegreen, Bournaud & Elmegreen 2008; Dekel et al. 2009b; Krumholz et al. 2018), numerical simulations of high-z gaseous discs (Aumer et al. 2010; Bournaud et al. 2014; Forbes et al. 2014; Goldbaum et al. 2015; Mandelker et al. 2016), and observations of high-z star-forming galaxies (Genzel et al. 2008, 2012, 2020; Swinbank et al. 2011; Guo et al. 2012; Tacconi et al. 2020). The migrating clumps may eventually form bulges, which stabilize the systems against further fragmentation (e.g. Genzel et al. 2008; Aumer et al. 2010).

Unfortunately, we have not found direct evidence of clump migration (i.e. inflow) in NGC 404, as its gas disc is viewed nearly face-on ($i \approx 9.3$ arcsec at $R_{\rm gal} \geq 15$ pc; Davis et al. 2020) and detecting clear non-circular motions is very difficult. Nevertheless, there seems to be some indirect evidence supporting inward clump migration. First, the molecular ring of NGC 404 is connected to the central region via a single arm-like structure (see Fig. 1). The kinematics of this arm is complex and fairly chaotic, with signs of strong streaming motions that may be due to the funnelling gas from the outer regions inward (Davis et al. 2020). Secondly, the molecular ring is incomplete (see, again, Fig. 1), implying it has recently been disrupted, possibly by inward clump migration. A key requirement for making inward clump migration a long-term phenomenon is a continuous, rapid supply of cold gas, which would replenish the ring (or disc) as it is being drained (Dekel et al. 2009a). If the gas supplied to the molecular ring is reduced, the molecular ring will gradually be destroyed, as seen in NGC 404.

If this migration scenario is true and clumps survive with physical properties largely unchanged for a migration time-scale (i.e. as they migrate towards the galactic centre), one would naturally expect the clumps in the central region and molecular ring to have similar clump properties. We now calculate the time-scale of clumps migrating from the molecular ring to the central region. According to standard accretion disc theory (e.g. Lynden-Bell & Pringle 1974), the time-scale for clumps to migrate to the galaxy centre due to collisions (i.e. viscosity) is

$$t_{\rm migrate} = \frac{1}{4}\,L_0^2\,V_0^{-2}\,\upsilon^{-1} \tag{42}$$

(see section 3.1 of Lynden-Bell & Pringle 1974), where $L_0 = R_0^2\,\Omega_0$ is the angular momentum (per unit mass) of a clump at galactocentric distance R_0, $V_0 = R_0\,\Omega_0$ is the orbital circular velocity of the clump, Ω_0 is the angular velocity of orbital circular rotation of the clump, and $\upsilon = \frac{1}{3}\upsilon_{\rm shear}\lambda_{\rm coll}$ is the kinetic viscosity. By adopting a galactocentric distance at the boundary between the central region and molecular ring, i.e. $R_0 = 15$ pc, we derive a migration time-scale $t_{\rm migrate} \approx 10$ Myr. This rapid inward migration of clumps from the molecular ring to the central region ($t_{\rm migrate} \approx 5.6\,t_{\rm orbit}$ at $R_0 = 15$ pc) suggests that the current molecular ring of NGC 404 is highly unstable and transient. Migrating clumps from the molecular ring may eventually merge once in the central region, forming a larger gravitationally stable system against fragmentation (and clump–clump collisions) and further gas inflow (i.e. further clump migration).

Clump migration may also trigger turbulence by converting the kinetic and gravitational energies of the clumps into turbulent energy (e.g. Krumholz & Burkert 2010; Forbes, Krumholz & Burkert 2012; Dekel & Burkert 2014; Forbes et al. 2014). Could it be that the large disc velocity dispersion observed in the central region of NGC 404 triggered by clump migration? The energy injection rate (per unit mass) due to clump migration is (Dekel & Burkert 2014)

$$\dot{\epsilon}_{\rm inject,migrate} = V_0^2/t_{\rm migrate}. \tag{43}$$

At a galactocentric distance of $R_0 = 15$ pc, $\dot{\epsilon}_{\rm inject,migrate} \approx 230\,{\rm km^2\,s^{-2}\,Myr^{-1}}$. If the disc velocity dispersion is maintained by clump migration, one expects

$$\dot{\epsilon}_{\rm inject,migrate} \approx \dot{\epsilon}_{\rm diss,disc} = \frac{1}{2}\sigma^2_{\rm gas,disc}/(2h_{\rm gas,disc}/\sigma_{\rm gas,disc}) \tag{44}$$

(see equation 6 in Dekel & Burkert 2014), where $\dot{\epsilon}_{\rm diss,disc}$ is the energy dissipation rate (per unit mass) of the gas disc and $2h_{\rm gas,\,disc}/\sigma_{\rm gas,\,disc}$ is the turbulence decay time-scale. Indeed, the central region (where $\sigma_{\rm gas,\,disc} \approx 10\,{\rm km\,s^{-1}}$ and $h_{\rm gas,\,disc} \approx 1$ pc) has an average disc energy dissipation rate (per unit mass) $\dot{\epsilon}_{\rm diss,disc} \approx 250\,{\rm km^2\,s^{-2}\,Myr^{-1}}$, which is approximately equal to the calculated energy injection rate (per unit mass) from clump migration $\dot{\epsilon}_{\rm inject,migrate} \approx 230\,{\rm km^2\,s^{-2}\,Myr^{-1}}$. It thus seems that clump migration may be the major mechanism driving turbulence in the central region of NGC 404, where the observed large velocity dispersions cannot be explained by clump–clump collisions or stellar feedback. However, other mechanisms may also play a role given the potential jet–ISM interaction in the core of this galaxy.

7 CONCLUSIONS

We studied the molecular structures (clumps and clouds) of the dwarf lenticular galaxy NGC 404. We performed a dendrogram analysis of our high-resolution ($\approx$0.86 $\times$ 0.51 pc^2) ALMA ^{12}CO(2-1) data and identified a number of nested structures, including 953 resolved clumps (i.e. leaves) and 1639 resolved clouds (i.e. branches and trunks), whose radii range from 0.4 to 25 pc. Our main findings are as follows.

(i) Two distinct regions are identified: a gravitationally stable central region (Toomre parameter Q = 3–30 and gas fraction $f_{\rm gas}$ $\approx$ 10–40 per cent) and a gravitationally unstable molecular ring (Q $\lesssim$ 1 and $f_{\rm gas}$ $\approx$ 50–70 per cent).

(ii) The differential mass distribution functions of the clumps are best fitted by two power laws with a turn-over or peak at $M_{\rm clump}$ $\approx$ 4000 M$_\odot$.

(iii) The molecular structures of the central region have an unusually steep size–linewidth relation $R_{\rm c} \propto \sigma_{\rm obs,los}^{0.82\pm0.11}$, while those of the molecular ring have a much shallower relation $R_{\rm c} \propto \sigma_{\rm obs,los}^{0.30\pm0.03}$ (with a flattening or turn-over at $R_{\rm c}$ $\approx$ 3 pc). The latter is similar to the Kolmogorov law for turbulence ($\sigma_{\rm obs,los} \propto R_{\rm c}^{1/3}$; Kolmogorov 1941).

(iv) The molecular structures of the central region and the molecular ring have similar mass–size relations (with power-law indices $D_{\rm m}$ = 2.27 $\pm$ 0.10 and $D_{\rm m}$ = 2.12 $\pm$ 0.01, respectively). However, while in the central region, clumps and clouds have similar power-law indices ($D_{\rm m,\,clump}$ = 2.07 $\pm$ 0.16 versus $D_{\rm m,\,cloud}$ = 2.22 $\pm$ 0.10), in the molecular ring, clumps have a much shallower power-law index than clouds ($D_{\rm m,\,clump}$ = 1.63 $\pm$ 0.04 versus $D_{\rm m,\,cloud}$ = 2.06 $\pm$ 0.01).

(v) In the central region, both clumps (mean virial parameter $\langle\alpha_{\rm vir,\,clump}\rangle$ = 1.52 $\pm$ 0.11) and clouds ($\langle\alpha_{\rm vir,\,cloud}\rangle$ = 1.14 $\pm$ 0.12) appear to be in virial equilibria. In the molecular ring, however, while clumps are in rough virial equilibria ($\langle\alpha_{\rm vir,\,clump}\rangle$ = 1.82 $\pm$ 0.07), clouds appear to be strongly gravitationally bound ($\langle\alpha_{\rm vir,\,cloud}\rangle$ = 0.41 $\pm$ 0.02).

The virial parameter of molecular structures in the molecular ring is in turn dependent on mass: $\alpha_{\rm vir,c} \propto M_{\rm c}^{-0.27\pm0.01}$.

We developed an analytical model of clump–clump collisions to explain the clump properties and gas turbulence in the molecular ring. Our model suggests that the collisions between clumps are driven by gravitational instabilities coupled with galactic shear, which leads to several results.

(i) The formation of clumps with $R_{\rm t,\,clump}$ $\approx$ $L_{\rm acc,\,clump}$ $\approx$ $\lambda_{\rm coll}$ (where $\lambda_{\rm coll} \equiv G\Sigma_{\rm gas,\,disc}/2A^2$ is the critical collision length arising from our model), i.e. the tidal radii of clumps approximately equal to the average distance between neighbouring clumps.

(ii) A typical clump mass $M_{\rm clump} \approx \Sigma_{\rm gas,disc}\lambda_{\rm coll}^2 \approx G^2\Sigma_{\rm gas,disc}^3/4A^4 \equiv M_{\rm c,coll}$ and a typical clump size $R_{\rm clump} \approx 0.38\lambda_{\rm coll} \equiv R_{\rm c,\,coll}$.

(iii) An energy injection rate (per unit mass) for the collision-induced turbulence $\dot{\epsilon}_{\rm inject,coll} \equiv G^2\Sigma_{\rm gas,disc}^2/2A \approx \dot{\epsilon}_{\rm diss,clump}$.

(iv) A size–linewidth relation $\sigma_{\rm obs,los} \approx (2G^2\Sigma_{\rm gas,disc}^2/A)^{1/3}R_{\rm c}^{1/3}$ (assuming a Kolmogorov spectrum of turbulence), with a flattening at the turbulence driving scale $L_{\rm D} \approx \lambda_{\rm coll}$.

(v) If the turbulence that supports the gas disc in vertical equilibrium is sustained by clump–clump collisions, a gas disc velocity dispersion $\sigma_{\rm max,\,coll} \equiv G\Sigma_{\rm gas,\,disc}/A \approx \sigma_{\rm gas,\,disc}$ and a gas disc scale height $h_{\rm gas,\,disc}$ $\approx$ $L_{\rm D}$ $\approx$ $\lambda_{\rm coll}$. Turbulence from clump–clump collisions can maintain the disc in a marginally gravitationally stable state, i.e. $Q \approx 1$.

(vi) A virial parameter $\alpha_{\rm vir,\,clump} \approx \alpha_{\rm vir,\,crit} = 2$ for clumps and $\alpha_{\rm vir,\,cloud} < 1$ for clouds, as $M_{\rm clump} \approx M_{\rm Jeans} \approx M_{\rm c,\,coll}$ while $M_{\rm cloud} > M_{\rm Jeans} \approx M_{\rm c,\,coll}$. Collision-induced turbulence can thus maintain the clumps (but not the clouds) in rough virial equilibria.

(vii) A mass–size relation for clumps $M_{\rm clump} = (5/\alpha_{\rm vir,crit}G)(2G^2\Sigma_{\rm gas,disc}^2/A)^{2/3}R_{\rm clump}^{5/3}$.

Our predictions above all match the observations very well in the molecular ring of NGC 404, suggesting clump–clump collisions are the dominant mechanism regulating clump properties and gas turbulence in that region. As expected, the collision model fails to explain the observations in the central region of NGC 404, where the gas disc is strongly gravitationally stable (Q = 3–30). It also seems that clumps migrate inward from the molecular ring to the central region, so that the clump properties do not change much between the two regions. In turn, clump migration may be the major source of turbulence in the central region, although other sources are possible (e.g. AGN feedback and/or the magneto-rotational instability).

Our model may be relevant to the understanding of molecular gas discs and star formation in high-z disc galaxies, as the molecular ring of NGC 404 resembles in many ways the star-forming gas discs observed at high redshifts (e.g. clumpy morphology, low Toomre parameter, and high gas fraction). We note, however, that our findings are based on only one galaxy. High-resolution observations of molecular gas in more gravitationally unstable gas discs are thus needed to further confirm our model.

ACKNOWLEDGEMENTS

We thank the referee for providing valuable comments that improved the paper. LL was supported by a Hintze Fellowship, funded by the Hintze Family Charitable Foundation, and by a DAWN Fellowship, funded by the Danish National Research Foundation under grant No. 140. MB was supported by STFC consolidated grant 'Astrophysics at Oxford' ST/H002456/1 and ST/K00106X/1. GXL acknowleges supports from NSFC grants W820301904 and 12033005. TAD acknowledges support from an STFC Ernest Rutherford Fellowship. MDS acknowledges support from an STFC DPhil studentship ST/N504233/1. This publication arises from research funded by the John Fell Oxford University Press Research Fund.

This paper uses the ALMA data. ALMA is a partnership of ESO (representing its member states), NSF (USA), and NINS (Japan), together with NRC (Canada) and NSC and ASIAA (Taiwan) and KASI (Republic of Korea), in cooperation with the Republic of Chile. The Joint ALMA Observatory is operated by ESO, AUI/NRAO, and NAOJ. This paper also uses observations made with the NASA/ESA Hubble Space Telescope, and obtained from the Hubble Legacy Archive, which is a collaboration between the Space Telescope Science Institute (STScI/NASA), the Space Telescope European Coordinating Facility (ST-ECF/ESA), and the Canadian Astronomy Data Centre (CADC/NRC/CSA). This research has used the NASA/IPAC Extragalactic Database (NED) which is operated by the Jet Propulsion Laboratory, California Institute of Technology, under contract with the National Aeronautics and Space Administration.

DATA AVAILABILITY

The data underlying this article are available in the ALMA archive (https://almascience.eso.org/asax/) under project code: (i) 2015.1.00597.S, (ii) 2017.1.00572.S and (iii) 2017.1.00907.S.

REFERENCES

Agertz O., Teyssier R., Moore B., 2009, MNRAS, 397, L64
Agertz O., Romeo A. B., Grisdale K., 2015, MNRAS, 449, 2156

Aumer M., Burkert A., Johansson P. H., Genzel R., 2010, ApJ, 719, 1230
Binney J., Tremaine S., 2008, Galactic Dynamics, 2nd edn. Princeton Univ. Press, Princeton
Blitz L., Rosolowsky E., 2006, ApJ, 650, 933
Blitz L., Shu F. H., 1980, ApJ, 238, 148
Bodenheimer P. H., 2011, Principles of Star Formation. Springer-Verlag, Berlin, Heidelberg
Boehle A., Larkin J. E., Armus L., Wright S. A., 2018, ApJ, 866, 79
Bolatto A. D., Leroy A. K., Rosolowsky E., Walter F., Blitz L., 2008, ApJ, 686, 948
Bournaud F., Elmegreen B. G., Teyssier R., Block D. L., Puerari I., 2010, MNRAS, 409, 1088
Bournaud F. et al., 2014, ApJ, 780, 57
Bresolin F., 2013, ApJ, 772, L23
Cappellari M., 2002, MNRAS, 333, 400
Carilli C. L., Walter F., 2013, ARA&A, 51, 105
Cen R., 2021, ApJ, 906, L4
Chabrier G., 2003, PASP, 115, 763
Colombo D. et al., 2014, ApJ, 784, 3
Cormier D. et al., 2017, MNRAS, 468, L87
Cowie L. L., 1980, ApJ, 236, 868
Dame T. M., 2011, preprint (arXiv:1101.1499)
Das M., Jog C. J., 1996, ApJ, 462, 309
Davis T. A. et al., 2013, MNRAS, 429, 534
Davis T. A. et al., 2020, MNRAS, 496, 4061
del Río M. S., Brinks E., Cepa J., 2004, AJ, 128, 89
Dekel A., Burkert A., 2014, MNRAS, 438, 1870
Dekel A. et al., 2009a, Nature, 457, 451
Dekel A., Sari R., Ceverino D., 2009b, ApJ, 703, 785
Dib S., Bell E., Burkert A., 2006, ApJ, 638, 797
Dobbs C. L., 2008, MNRAS, 391, 844
Dobbs C. L., Pringle J. E., 2013, MNRAS, 432, 653
Dobbs C. L., Burkert A., Pringle J. E., 2011, MNRAS, 413, 2935
Dobbs C. L. et al., 2014, in Beuther H., Klessen R. S., Dullemond C. P., Henning T., eds, Protostars and Planets VI. Univ. Arizona Press, Tucson, p. 3
Dobbs C. L., Pringle J. E., Duarte-Cabral A., 2015, MNRAS, 446, 3608
Donovan Meyer J. et al., 2013, ApJ, 772, 107
Dutta P., Begum A., Bharadwaj S., Chengalur J. N., 2009, MNRAS, 397, L60
Elmegreen B. G., 2011, ApJ, 737, 10
Elmegreen B. G., Burkert A., 2010, ApJ, 712, 294
Elmegreen B. G., Falgarone E., 1996, ApJ, 471, 816
Elmegreen B. G., Scalo J., 2004, ARA&A, 42, 211
Elmegreen B. G., Kim S., Staveley-Smith L., 2001, ApJ, 548, 749
Elmegreen D. M., Elmegreen B. G., Ravindranath S., Coe D. A., 2007, ApJ, 658, 763
Elmegreen B. G., Bournaud F., Elmegreen D. M., 2008, ApJ, 688, 67
Elmegreen B. G., Rubio M., Hunter D. A., Verdugo C., Brinks E., Schruba A., 2013, Nature, 495, 487
Emsellem E., Monnet G., Bacon R., 1994, A&A, 285, 723
Faesi C. M., Lada C. J., Forbrich J., 2016, ApJ, 821, 125
Falgarone E., Phillips T. G., 1991, in Falgarone E., Boulanger F., Duvert G., eds, Proc. IAU Symp. 147, Fragmentation of Molecular Clouds and Star Formation. Kluwer, Dordrecht, p. 119
Federrath C., 2013, MNRAS, 436, 1245
Federrath C., Klessen R. S., 2012, ApJ, 761, 156
Field G. B., Blackman E. G., Keto E. R., 2008, MNRAS, 385, 181
Field G. B., Blackman E. G., Keto E. R., 2011, MNRAS, 416, 710
Fisher D. B. et al., 2017, ApJ, 839, L5
Fleck Robert C. J., 1987, ApJ, 315, 259
Forbes J., Krumholz M., Burkert A., 2012, ApJ, 754, 48
Forbes J. C., Krumholz M. R., Burkert A., Dekel A., 2014, MNRAS, 438, 1552
Fukui Y., Kawamura A., 2010, ARA&A, 48, 547
Fukui Y., Mizuno N., Yamaguchi R., Mizuno A., Onishi T., 2001, PASJ, 53, L41
Fukui Y., Habe A., Inoue T., Enokiya R., Tachihara K., 2021, PASJ, 73, S1
Gammie C. F., 2001, ApJ, 553, 174
Gammie C. F., Ostriker J. P., Jog C. J., 1991, ApJ, 378, 565
Genzel R. et al., 2008, ApJ, 687, 59
Genzel R. et al., 2012, ApJ, 746, 69
Genzel R. et al., 2014, ApJ, 785, 75
Genzel R. et al., 2020, ApJ, 902, 98
Goldbaum N. J., Krumholz M. R., Forbes J. C., 2015, ApJ, 814, 131
Goldbaum N. J., Krumholz M. R., Forbes J. C., 2016, ApJ, 827, 28
Goodman A. A., Rosolowsky E. W., Borkin M. A., Foster J. B., Halle M., Kauffmann J., Pineda J. E., 2009, Nature, 457, 63
Gouliermis D. A., 2018, PASP, 130, 072001
Guo Y., Giavalisco M., Ferguson H. C., Cassata P., Koekemoer A. M., 2012, ApJ, 757, 120
Hasegawa T., Sato F., Whiteoak J. B., Miyawaki R., 1994, ApJ, 429, L77
Hennebelle P., Falgarone E., 2012, A&A Rev., 20, 55
Henshaw J. D. et al., 2016, MNRAS, 457, 2675
Henshaw J. D. et al., 2019, MNRAS, 485, 2457
Henshaw J. D., Barnes A. T., Battersby C., Ginsburg A., Sormani M. C., Walker D. L., 2022, preprint (arXiv:2203.11223)
Hirota A., Kuno N., Sato N., Nakanishi H., Tosaki T., Sorai K., 2011, ApJ, 737, 40
Hughes A. et al., 2013, ApJ, 779, 46
Hughes A., Meidt S., Colombo D., Schruba A., Schinnerer E., Leroy A., Wong T., 2016, in Jablonka P., Andrè Ph., van der Tak F., eds, Proc. IAU Symp. 315, From Interstellar Clouds to Star-Forming Galaxies: Universal Processes?. Cambridge Univ. Press, p. 30
Hunter D. A., Elmegreen B. G., Berger C. L., 2019, AJ, 157, 241
Imara N., Faesi C. M., 2019, ApJ, 876, 141
Jog C. J., Ostriker J. P., 1988, ApJ, 328, 404
Kanekar N., Prochaska J. X., Neeleman M., Christensen L., Møller P., Zwaan M. A., Fynbo J. P. U., Dessauges-Zavadsky M., 2020, ApJ, 901, L5
Karachentsev I. D. et al., 2002, A&A, 389, 812
Kauffmann J., Pillai T., Shetty R., Myers P. C., Goodman A. A., 2010, ApJ, 716, 433
Kauffmann J., Pillai T., Zhang Q., 2013, ApJ, 765, L35
Kauffmann J., Pillai T., Zhang Q., Menten K. M., Goldsmith P. F., Lu X., Guzmán A. E., 2017, A&A, 603, A89
Kawakatu N., Wada K., Ichikawa K., 2020, ApJ, 889, 84
Kim W.-T., Ostriker E. C., 2001, ApJ, 559, 70
Kim W.-T., Ostriker E. C., 2007, ApJ, 660, 1232
Kim C.-G., Ostriker E. C., 2015, ApJ, 802, 99
Kim W.-T., Ostriker E. C., Stone J. M., 2003, ApJ, 599, 1157
Kobayashi M. I. N., Inutsuka S.-i., Kobayashi H., Hasegawa K., 2017, ApJ, 836, 175
Kobayashi M. I. N., Kobayashi H., Inutsuka S.-i., Fukui Y., 2018, PASJ, 70, S59
Kolmogorov A., 1941, Akademiia Nauk SSSR Doklady, 30, 301
Koyama H., Ostriker E. C., 2009, ApJ, 693, 1346
Krieger N. et al., 2020, ApJ, 899, 158
Kritsuk A. G., Norman M. L., 2011, preprint (arXiv:1111.2827)
Kritsuk A. G., Norman M. L., Padoan P., Wagner R., 2007, ApJ, 665, 416
Kritsuk A. G. et al., 2011, ApJ, 737, 13
Kritsuk A. G., Lee C. T., Norman M. L., 2013, MNRAS, 436, 3247
Kruijssen J. M. D., Longmore S. N., 2014, MNRAS, 439, 3239
Krumholz M., Burkert A., 2010, ApJ, 724, 895
Krumholz M. R., Burkhart B., 2016, MNRAS, 458, 1671
Krumholz M. R., Kruijssen J. M. D., 2015, MNRAS, 453, 739
Krumholz M. R., Burkhart B., Forbes J. C., Crocker R. M., 2018, MNRAS, 477, 2716
Kwan J., 1979, ApJ, 229, 567
Leroy A., Bolatto A., Walter F., Blitz L., 2006, ApJ, 643, 825
Leroy A. K. et al., 2011, ApJ, 737, 12
Leroy A. K. et al., 2015, ApJ, 801, 25
Li G.-X., 2017a, MNRAS, 465, 667
Li G.-X., 2017b, MNRAS, 471, 2002
Li G.-X., Zhang C.-P., 2020, ApJ, 897, 89
Li Q., Tan J. C., Christie D., Bisbas T. G., Wu B., 2018, PASJ, 70, S56
Lighthill M. J., 1955, Proc. IAU Symp. 2, Gas Dynamics of Cosmic Clouds. North-Holland Publ. Company, Amsterdam, p. 121

Lin D. N. C., Pringle J. E., 1987, MNRAS, 225, 607
Liu L., Bureau M., Blitz L., Davis T. A., Onishi K., Smith M., North E., Iguchi S., 2021, MNRAS, 505, 4048
Lombardi M., Alves J., Lada C. J., 2010, A&A, 519, L7
Lynden-Bell D., Pringle J. E., 1974, MNRAS, 168, 603
Mac Low M.-M., 1999, ApJ, 524, 169
Mac Low M.-M., Klessen R. S., 2004, Rev. Mod. Phys., 76, 125
Mac Low M.-M., Smith M. D., Klessen R. S., Burkert A., 1998, Ap&SS, 261, 195
Madden S. C., Cormier D., 2019, in McQuinn K. B. W., Stierwalt S., eds, Proc. IAU Symp. 344, Dwarf Galaxies: From the Deep Universe to the Present. Kluwer, Dordrecht, p. 240
Maeda F., Ohta K., Fujimoto Y., Habe A., 2021, MNRAS, 502, 2238
Mandelbrot B. B., Whitrow G. J., 1983, J. Br. Astron. Assoc., 93, 238
Mandelker N., Padnos D., Dekel A., Birnboim Y., Burkert A., Krumholz M. R., Steinberg E., 2016, MNRAS, 463, 3921
Maoz D., Koratkar A., Shields J. C., Ho L. C., Filippenko A. V., Sternberg A., 1998, AJ, 116, 55
McKee C. F., Ostriker E. C., 2007, ARA&A, 45, 565
Miville-Deschênes M. A., Duc P. A., Marleau F., Cuillandre J. C., Didelon P., Gwyn S., Karabal E., 2016, A&A, 593, A4
Miville-Deschênes M.-A., Murray N., Lee E. J., 2017, ApJ, 834, 57
Motiño Flores S. M., Wiklind T., Eufrasio R. T., 2021a, ApJ, 921, 130
Motiño Flores S. M., Wiklind T., Eufrasio R., 2021b, in American Astronomical Society Meeting Abstracts. p. 219.04D
Muller E. et al., 2010, ApJ, 712, 1248
Murphy E. J. et al., 2011, ApJ, 737, 67
Myers P. C., 2009, ApJ, 700, 1609
Namekata D., Habe A., 2011, ApJ, 731, 57
Nguyen D. D., 2017, preprint (arXiv:1712.02470)
Nyland K. et al., 2017, ApJ, 845, 50
Oka T., Hasegawa T., Sato F., Tsuboi M., Miyazaki A., Sugimoto M., 2001, ApJ, 562, 348
Orkisz J. H. et al., 2017, A&A, 599, A99
Ozernoy L. M., Fridman A. M., Biermann P. L., 1998, A&A, 337, 105
Padoan P. et al., 2014, in Beuther H., Klessen R. S., Dullemond C. P., Henning T., eds, Protostars and Planets VI. Univ. Arizona Press, Tucson, p. 77
Perdang J., 1990, Vistas Astron., 33, 371
Piontek R. A., Ostriker E. C., 2004, ApJ, 601, 905
Piontek R. A., Ostriker E. C., 2005, ApJ, 629, 849
Piontek R. A., Ostriker E. C., 2007, ApJ, 663, 183
Querejeta M. et al., 2021, A&A, 645, A97
Rice T. S., Goodman A. A., Bergin E. A., Beaumont C., Dame T. M., 2016, ApJ, 822, 52
Rizzo F., 2020, in American Astronomical Society Meeting Abstracts #236. p. 122.04
Roman-Duval J., Jackson J. M., Heyer M., Rathborne J., Simon R., 2010, ApJ, 723, 492
Rosolowsky E., 2005, PASP, 117, 1403
Rosolowsky E., Leroy A., 2006, PASP, 118, 590
Rosolowsky E. W., Pineda J. E., Kauffmann J., Goodman A. A., 2008, ApJ, 679, 1338
Salpeter E. E., 1955, ApJ, 121, 161
Sano H. et al., 2021, PASJ, 73, S62
Schmidt A. A., Bica E., Alloin D., 1990, MNRAS, 243, 620
Schneider N. et al., 2012, A&A, 540, L11
Schruba A. et al., 2017, ApJ, 835, 278
Seth A. C. et al., 2010, ApJ, 714, 713
Shetty R., Ostriker E. C., 2012, ApJ, 754, 2
Simon R., Jackson J. M., Clemens D. P., Bania T. M., Heyer M. H., 2001, ApJ, 551, 747
Solomon P. M., Rivolo A. R., Barrett J., Yahil A., 1987, ApJ, 319, 730
Sormani M. C. et al., 2019, MNRAS, 488, 4663
Stark A. A., Blitz L., 1978, ApJ, 225, L15
Stilp A. M., Dalcanton J. J., Skillman E., Warren S. R., Ott J., Koribalski B., 2013, ApJ, 773, 88
Stott J. P. et al., 2016, MNRAS, 457, 1888
Sun J. et al., 2018, ApJ, 860, 172
Sun J. et al., 2020, ApJ, 901, L8
Swinbank A. M. et al., 2011, ApJ, 742, 11
Swinbank A. M. et al., 2015, ApJ, 806, L17
Tacconi L., 2012, in American Astronomical Society Meeting Abstracts #219. p. 421.01
Tacconi L. J., Genzel R., Sternberg A., 2020, ARA&A, 58, 157
Tadaki K. et al., 2018, Nature, 560, 613
Takahira K., Shima K., Habe A., Tasker E. J., 2018, PASJ, 70, S58
Tan J. C., 2000, ApJ, 536, 173
Tan J. C., Shaske S. N., Van Loo S., 2013, in Wong T., Ott J., eds, Proc. IAU Symp. 292, Molecular Gas, Dust, and Star Formation in Galaxies. Kluwer, Dordrecht, p. 19
Tasker E. J., Tan J. C., 2009, ApJ, 700, 358
Taylor C. L., Petitpas G. R., del Rio M. S., 2015, AJ, 149, 187
Thompson T. A., Quataert E., Murray N., 2005, ApJ, 630, 167
Thornton K., Gaudlitz M., Janka H. T., Steinmetz M., 1998, ApJ, 500, 95
Tikhonov N. A., Galazutdinova O. A., Aparicio A., 2003, A&A, 401, 863
Toomre A., 1964, ApJ, 139, 1217
Urquhart J. S. et al., 2013, MNRAS, 431, 1752
Utomo D., Blitz L., Davis T., Rosolowsky E., Bureau M., Cappellari M., Sarzi M., 2015, ApJ, 803, 16
Veltchev T. V., Ossenkopf-Okada V., Stanchev O., Schneider N., Donkov S., Klessen R. S., 2018, MNRAS, 475, 2215
Vollmer B., Beckert T., 2002, A&A, 382, 872
Vollmer B., Duschl W. J., 2001, A&A, 367, 72
Williams B. F., Dalcanton J. J., Gilbert K. M., Stilp A., Dolphin A., Seth A. C., Weisz D., Skillman E., 2010, ApJ, 716, 71
Williamson D. J., Thacker R. J., 2012, MNRAS, 421, 2170
Wong T. et al., 2011, ApJS, 197, 16
Wong T. et al., 2019, ApJ, 885, 50
Wu B., Tan J. C., Nakamura F., Van Loo S., Christie D., Collins D., 2017a, ApJ, 835, 137
Wu B., Tan J. C., Christie D., Nakamura F., Van Loo S., Collins D., 2017b, ApJ, 841, 88
Wu B., Tan J. C., Nakamura F., Christie D., Li Q., 2018, PASJ, 70, S57
Zhang C.-P., Li G.-X., 2017, MNRAS, 469, 2286
Zhang C.-P. et al., 2016, A&A, 585, A117

SUPPORTING INFORMATION

Supplementary data are available at *MNRAS* online.

Table S1: Properties of the dendrogram-defined structures of NGC 404

Please note: Oxford University Press is not responsible for the content or functionality of any supporting materials supplied by the authors. Any queries (other than missing material) should be directed to the corresponding author for the article.

APPENDIX A: CUMULATIVE MASS FUNCTION OF CLUMPS

The cumulative clump mass distribution function can be characterized quantitatively by a power law

$$N_{\rm clump}(M'_{\rm clump} > M_{\rm clump}) = \left(\frac{M_{\rm clump}}{M_{0,\rm clump}}\right)^{\gamma_{\rm clump}+1}, \quad \text{(A1)}$$

where $N_{\rm clump}(M'_{\rm clump} > M_{\rm clump})$ is the number of clumps with a mass greater than $M_{\rm clump}$, $M_{0,\rm clump}$ sets the normalization, and $\gamma_{\rm clump}$ is the power-law index.

Fig. A1 presents the normalized cumulative mass distribution function (and its power-law fit as a dashed green line) of the resolved clumps in the the central region, molecular ring, and whole disc of NGC 404, respectively. The power-law fits are only performed above the mass completeness limit $M_{\rm comp} = 1.8 \times 10^3$ M$_\odot$ (see Section 3.1).

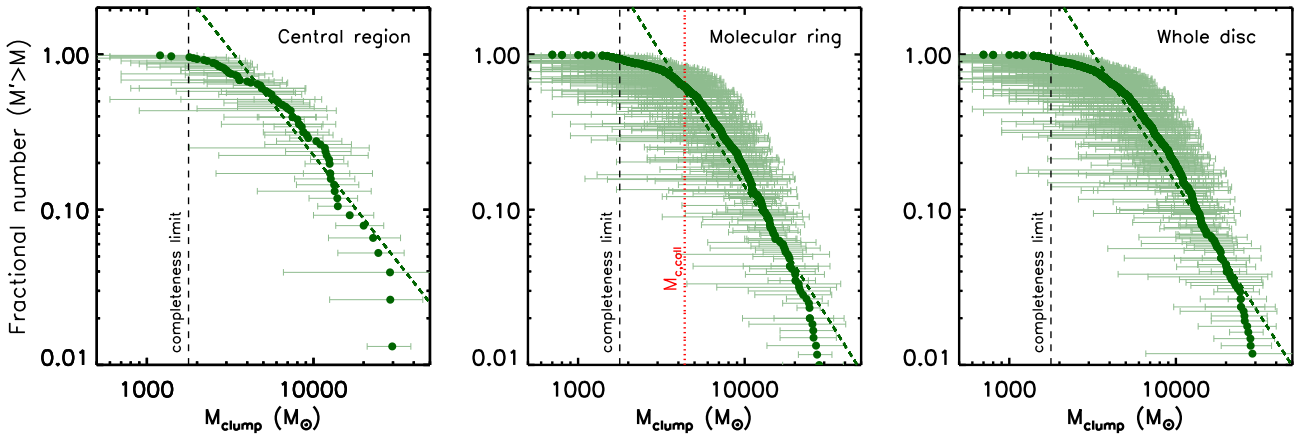

Figure A1. Normalized cumulative mass distribution function of the resolved clumps in the central region, molecular ring, and whole disc of NGC 404, respectively. The power law best fitting the cumulative mass distribution is overlaid as green dashed lines in each panel. Our mass completeness limit is indicated by a black vertical dashed line in each panel. The red dotted line in the middle panel indicates our model-predicted turn-over mass in the molecular ring ($M_{c,\,coll}$; see Sections 4.2 and 6.1 for more details).

We find power laws fit the cumulative mass functions relatively well in the mass regime $M_{clump} \gtrsim 4000\ M_\odot$. The best-fitting power-law index γ_{clump} of the cumulative mass distribution function is -2.36 ± 0.10, -2.70 ± 0.06, and -2.67 ± 0.07 for the central region, molecular ring, and whole disc, respectively. These best-fitting power-law indexes are similar to those of the differential mass distribution function in the high-mass regime γ^{+}_{clump} (-2.63 ± 0.49, -2.87 ± 0.13, and -2.67 ± 0.16 for the central region, molecular ring, and whole disc, respectively; see Section 3.1). It thus seems that most of the molecular gas mass of NGC 404 is located in low-mass clumps.

We note, however, that power-law functions only seem to fit well at the high-mass ends of the cumulative clump mass distribution functions, and 'turn-overs', which are break points in the power-law functions, seem to be present in all the cumulative mass distributions at the same clump mass $M_{clump} \approx 4000\ M_\odot$. Indeed, the cumulative mass distribution functions show strong deviations from the best-fitting power laws (green dash lines in the Fig. A1) below this turn-over mass. As this turn-over mass is much larger than the mass completeness limit, these deviations are most likely real and probe (and thus inform on) the underlying formation and destruction of clumps. The presence of these turn-overs may in fact suggest less negative or even positive power-law indices (i.e. 'slopes') at the low-mass ends of the cumulative clump mass distribution functions.

APPENDIX B: COLLISION TIME-SCALE

In this section, we derive the collision time-scale of clumps from first principles. Following Tan (2000), we set the collision velocity of clumps to be the shear velocity

$$v_{shear} \equiv v_{shear}(R) = b\,(\Omega - \frac{\mathrm{d}V_{circ}}{\mathrm{d}R}) = 2Ab \qquad \text{(B1)}$$

(see equation 46 in Liu et al. 2021), where $A \equiv A(R) = -\frac{R}{2}\frac{\mathrm{d}\Omega}{\mathrm{d}R}$ is Oort's constant A evaluated at the galactocentric distance R of the clump (R_{gal} in Table 1), $\Omega \equiv \Omega(R) = V_{circ}/R$ is the angular velocity of orbital circular rotation, $V_{circ} \equiv V_{circ}(R)$ is the circular velocity of the galaxy, and b is the radial distance between the orbits of the two colliding clumps. We note that the shear velocity v_{shear} is derived using the shearing-sheet approximation (e.g. Binney & Tremaine 2008). Fig. B1 shows the dependence of Ω and Oort's constant A on the galactocentric distance R in NGC 404.

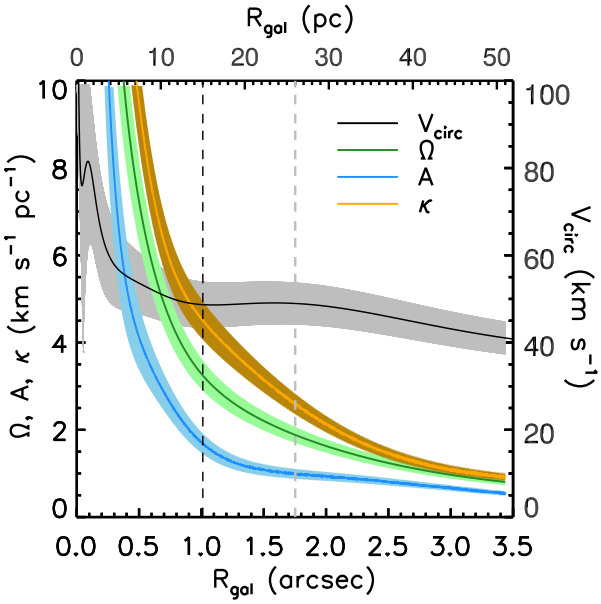

Figure B1. Galactocentric distance dependence of the orbital circular velocity V_{cir} (black curve), orbital circular angular velocity Ω (green curve), Oort's constants A (blue curve), and epicyclic frequency κ (orange curve) in NGC 404. The coloured envelope around each curve indicates the $\pm 1\sigma$ uncertainties. The black vertical dashed line indicates the boundary ($R_{gal} = 15$ pc) between the central region and molecular ring, while the grey vertical dashed line indicates the galactocentric distance ($R_{gal} = 27$ pc) beyond which the molecular gas disc is no longer gravitationally stable (i.e. Toomre parameter's $Q \leq 1$ at $R_{gal} \geq 27$ pc; see Section 4.5). The circular velocity curve is nearly flat in the molecular ring.

We adopt the circular velocity curve of Davis et al. (2020), derived by creating a gas dynamical model using the `Kinematic Molecular Simulation` (`KinMS`) package of Davis et al. (2013). Inputs to the model include the stellar mass distribution, stellar mass-to-light ratio, molecular gas mass, SMBH mass, as well as the disc orientation (position angle and inclination) and position (spatially and spectrally). The stellar mass distribution is parametrized by a

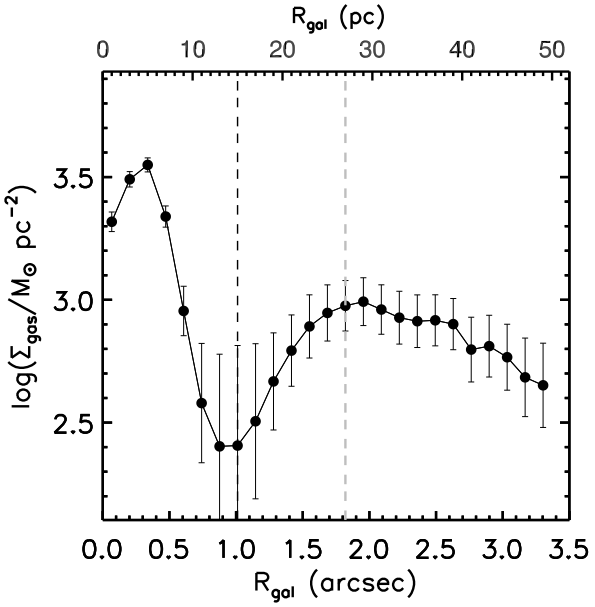

Figure B2. Galactocentric distance dependence of the coarse-grained deprojected molecular gas mass surface density of the NGC 404 disc, with a radial bin size of 2 pc. The error bars indicate the 1σ scatter of the different mass surface densities within each radial bin (not the uncertainty on the mean within each bin, which is much smaller). The black vertical dashed line indicates the boundary ($R_{\rm gal} = 15$ pc) between the central region and molecular ring, while the grey vertical dashed line indicates the galactocentric distance ($R_{\rm gal} = 27$ pc) beyond which the molecular gas disc is no longer gravitationally stable (i.e. Toomre parameter's $Q \leq 1$ at $R_{\rm gal} \geq 27$ pc; see Section 4.5).

multi-Gaussian expansion (MGE; Emsellem, Monnet & Bacon 1994; Cappellari 2002) fit to *HST* images of the nucleus from Nguyen (2017), while the molecular gas mass distribution is parametrized by an MGE fit to the ALMA CO(2-1) image of Davis et al. (2020). We use stellar mass-to-light ratios calculated on a pixel-by-pixel basis from multiband imaging by Davis et al. (2020). The MGE model of the molecular gas does not account for the flocculent substructure of the molecular gas disc, but it does allow to quantify the contribution to the potential of an ideal axisymmetric approximation of the observed molecular gas disc (Davis et al. 2020). The SMBH mass ($M_{\rm BH} \approx 5.7 \times 10^5$ M$_\odot$), position angle (PA $= 37.2^\circ$ at $R_{\rm gal} < 15$ pc and PA $= 1^\circ$ at $R_{\rm gal} \geq 15$ pc) and inclination ($i = 37.1^\circ$ at $R_{\rm gal} < 15$ pc and $i = 9.3^\circ$ at $R_{\rm gal} \geq 15$ pc) were then obtained from the best fit to the kinematics of the CO gas. Full details of the fitting procedure can be found in Davis et al. (2020).

We set the radius of the effective collision cross-section of a clump to be its tidal radius $R_{\rm t}$ rather than its actual radius $R_{\rm clump}$, as we consider clump–clump collisions to be any mutual gravitational interaction and ultimate merging of clumps (rather than exclusively physical collisions). We adopt the definition of tidal radius from Gammie et al. (1991) and Tan (2000), whereby the tidal radius marks the radial distance from a clump's centre at which the shear velocity of the clump due to differential galactic rotation is equal to its escape velocity. This leads to

$$R_{\rm t} = (1 - \beta_{\rm circ})^{-2/3} \left(\frac{2M_{\rm c}}{M_{\rm gal}}\right)^{1/3} R \tag{B2}$$

(see equation 8 in Tan 2000), where as before $M_{\rm c}$ is the clump's mass, $\beta_{\rm circ} \equiv \beta_{\rm circ}(R) = \frac{{\rm d}\ln V_{\rm circ}}{{\rm d}\ln R}$, and $M_{\rm gal} \equiv M_{\rm gal}(R)$ is the total galaxy mass interior to R. Equation (B2) assumes a spherical mass distribution, i.e. $M_{\rm gal}(R) = V_{\rm circ}^2(R)R/G$, and can therefore be simplified to

$$R_{\rm t} = \left(\frac{G}{2A^2}\right)^{1/3} M_{\rm c}^{1/3}. \tag{B3}$$

The tidal radius defined in this manner is the maximum size of a gravitationally bound cloud (of a given mass $M_{\rm c}$) allowed by galactic rotational shear (quantified by A). Normally, the tidal radius of a self-gravitating object is at least a few times larger than its actual radius. We note that in our formalism, a collision occurs between two clumps only when the radial distance between their orbits b is smaller than their tidal radius $R_{\rm t}$.

Using the above-defined collision velocity (i.e. the shear velocity $v_{\rm shear}$) and collision cross-section (i.e. the tidal radius $R_{\rm t}$), we can derive a clump–clump (or cloud–cloud) collision rate

$$\begin{aligned} Z_{\rm coll} \equiv Z_{\rm coll}(R) &= 2\int_0^{R_{\rm t}} z_{\rm coll}\,{\rm d}b \\ &= 2\int_0^{R_{\rm t}} N_{\rm A}\, v_{\rm shear}\,{\rm d}b \\ &= 4A\int_0^{R_{\rm t}} N_{\rm A}\, b\,{\rm d}b, \end{aligned} \tag{B4}$$

where $z_{\rm coll} \equiv z_{\rm coll}(b) = N_{\rm A}\, v_{\rm shear}$ is the collision rate per unit length, $N_{\rm A} \equiv N_{\rm A}(b) = \Sigma_{\rm gas,\,disc}/M_{\rm c}$ is the number surface density of molecular structures, $\Sigma_{\rm gas,\,disc} \equiv \Sigma_{\rm gas,\,disc}(b)$ is the coarse-grained gaseous mass surface density of the disc, and $v_{\rm shear}$ is taken from equation (B1). It is reasonable to define the number surface density of clumps $N_{\rm A}$ in this manner as we have assumed collisions occur only between clumps of equal mass. The first factor of 2 in equation (B4) accounts for clumps/clouds either catching up with others clumps/clouds at larger $R_{\rm gal}$ or being caught up by other clumps/clouds at smaller $R_{\rm gal}$ (Tan 2000). If we assume clumps are approximately uniformly distributed over a region of radius $\approx R_{\rm t}$ centred on the clump, then $N_{\rm A}$ in equation (B4) (or equivalently $\Sigma_{\rm gas,\,disc}$) is approximately constant, i.e. $N_{\rm A}(b) \approx N_{\rm A}(R) = \frac{1}{M_{\rm c}}\Sigma_{\rm gas,disc}(R)$, where $\Sigma_{\rm gas,\,disc}(R)$ is the coarse-grained gaseous mass surface density of the disc evaluated at the centre (galactocentric distance) of the reference clump ($R_{\rm gal}$ in Table 1). This leads to

$$Z_{\rm coll} \approx 4AN_{\rm A}\int_0^{R_{\rm t}} b\,{\rm d}b \approx 2AN_{\rm A}R_{\rm t}^2. \tag{B5}$$

The clump–clump (or cloud–cloud) collision time-scale is then

$$t_{\rm coll} \equiv t_{\rm coll}(R) = 1/Z_{\rm coll} \approx \frac{1}{2AN_{\rm A}R_{\rm t}^2} \approx \frac{A^{1/3}M_{\rm c}^{1/3}}{2^{1/3}G^{2/3}\Sigma_{\rm gas,disc}}, \tag{B6}$$

where the last expression assumes a spherical galaxy mass distribution (via equation B3). Fig. B2 shows the deprojected molecular gas mass surface density $\Sigma_{\rm gas,\,disc}$ as a function of the galactocentric distance R (i.e. $R_{\rm gal}$) in NGC 404. The mass surface density $\Sigma_{\rm gas,\,disc}$ is computed by summing the molecular gas mass within galactocentric annuli of increasing $R_{\rm gal}$ (with a radial bin size of 2 pc), corrected for inclination (where a fixed position angle $PA = 1^\circ$ and inclination angle $i = 9.3^\circ$ were adopted). We note that our derived collision time-scale above is essentially the same as that derived by Tan (2000; see their equation 13), except that we adopted $R_{\rm t}$ rather than $1.6\,R_{\rm t}$ as the radius of the effective collision cross-section. We use the subscript 'c' when referring to the masses of the molecular structures in equations B2–6, as the equations apply equally to clump–clump collisions and cloud–cloud collisions.

This paper has been typeset from a TEX/LATEX file prepared by the author.